Robust, Portable Optical Cavities utilising; Invar, Additive Manufacturing and an Ultra-stable Diamond Cavity

by

Freya Owen

A thesis presented to the
University of Birmingham
for the degree of
DOCTOR OF PHILOSOPHY

Quantum Matter Research Group
School of Physics and Astronomy
College of Engineering and Physical Sciences
University of Birmingham
February 2023

UNIVERSITY^{OF}
BIRMINGHAM

University of Birmingham Research Archive

e-theses repository

Abstract

Optical cavities provide the stability required for lasers to be utilised in a range of scientific applications, including for quantum technologies. The work described here discusses a range of novel, Fabry-Perot optical cavities which are designed to be utilised within different aspects of quantum technologies. Where firstly, there is an introduction to Fabry-Perot optical cavities with a discussion on their key properties, as well as detailed descriptions of perturbations that affect the stability of Fabry-Perot optical cavities.

The first optical cavity mentioned, is a tunable ULE-FS (ultra-low expansion glass - fused silica) optical cavity to stabilise a currently free running 2.6μm re-pump laser, for a strontium (Sr) magneto-optical trap. This leads onto descriptions of two invar cavities which are designed to stabilise the first stage of cooling of Sr atoms for portable Sr optical clocks. Where the use of additive manufacturing and selective laser melting is used to built both compact, portable, invar optical cavities. Lastly, two diamond cavities are introduced, where the first is a diamond-diamond optical cavity and the second is a diamond-FS optical cavity. These diamond cavities are found to have simulated acceleration sensitivities as low as $7/9\times10^{-15}$/g, which is lower than any other published optical cavity, resulting in these diamond cavities being applicable in deployable optical clocks and other deployable quantum technologies.

Acknowledgements

I would like to thank the following people, without whom I would not have been able to complete this research.

Dr. Jonathan Jones for his support and guidance through out my PhD and for providing me with constant knowledge and expertise to allow for my research to expand.

Prof. Kai Bongs for the opportunity to be part of this project and for his invaluable knowledge and feedback on my research.

Prof. Moataz Attallah and his research group in advanced material processing at the University of Birmingham for their input and knowledge in additive manufacturing and for their time spend in selective laser melting both invar spacers spoken about in this thesis.

Lastly, I would like to thank Dr. Jonathan Bass for constantly encouraging me and for challenging me to grow as a researcher.

Contents

List of Figures

9

List of Tables

1   Introduction

Albert Einstein first theorised of the concept of stimulated emission, where by when an electromagnetic wave interacts with an excited molecule or atom, it triggers it to drop into a lower energy level, causing the emission of a further electromagnetic wave. This theory was later picked up by Charles Townes, where in 1954 he took the idea further by building the first maser [1]. Within the maser was a large population of excited molecules, within a reflecting vessel, such that when the molecules started interacting and stimulating together this provoked a feedback loop which amplified the emitting electromagnetic waves from the molecules, causing *"microwave amplification by stimulated emission of radiation"*, hence being known as a maser. Later on in 1960, Theodore Maiman successfully constructed the first laser [2], which unlike like the masers, emitted electromagnetic waves of a shorter wavelength within the light spectral region and are therefore known as an acronym of: *"light amplification by stimulated emission of radiation"*.

The first laser utilised a ruby rod as the gain medium [3], which had silver-coated reflective surfaces at either end of the rod to act as the mirrors, to create the cavity around the medium. The particles were then *pumped* by shining a high-power flash lamp onto the ruby rod, causing the particles to rise from their initial ground state to a higher energy state. Almost instantly the particles in the higher energy state emit a photon, known as *spontaneous emission* and fall into a metastable state. These particles can then go through spontaneous emission again and fall back in the ground state or interact with another photon, causing the release of two photons and subsequently falling back into the ground state, known as *stimulated emission*. The emitted photons from both of these processes then go on to produce more stimulated emission from particles within the metastable state, while simultaneously the pump is pumping the particles in the ground state up to the higher energy state. After a certain time period more particles will be in the metastable state than in the ground state, which is known as *population inversion*. Once population inversion occurs the large number photons produced start circulating round the cavity building a feedback loop through the medium. Resulting in a band of certain frequencies to be coherently amplified and pass through the medium and out of the cavity, creating the lasing output. This laser structure is incredibly similar and typical of most lasers found today, with a diagram displaying the key elements of a laser shown in Figure 1. The only key difference between different lasers even in modern times is the type of atoms or molecules that are used for the laser medium.
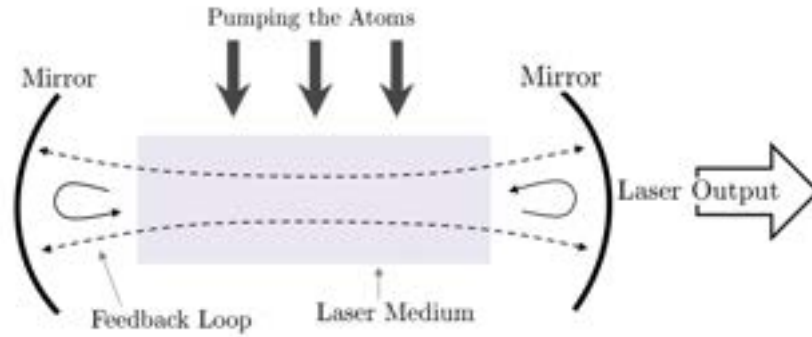
Figure 1: A diagram of the key elements in a typical laser.

Since the invention of the first laser the new technology has had tremendous potential and the science based around it has grown almost exponentially, to the point that lasers are now a multi-billion pound industry and are commonly utilised in many every day devices including, CD/DVD players, laser printers, fiber-optical communications, types of welding and cutting machines and within certain medical instruments. However, lasers also have applications in many scientific applications and in particular in quantum technologies for metrology and sensors, but most lasers on the market do not match the stability requirements for these technologies and lab experiments. Therefore, an external frequency reference needs to be used to stabilise the laser frequency, which is when an optical resonator or cavity can be implemented within an optical system. Optical cavities are an ideal solution to stabilise light as they can easily be tailored to work across a wide range of wavelengths to produce incredibly stable lasers.

1.1   Optical Resonators and Cavities

Optical cavities are commonly configured as two highly reflective mirrors attached to a medium, known as the spacer. The spacer is normally hollow and contains a "cavity", referred to as the bore, where the light is confined along the optical axis, by the mirrors at either end of the spacer, as denoted in Figure 2, where a detailed description of how optical cavities function is given in Chapter 2.
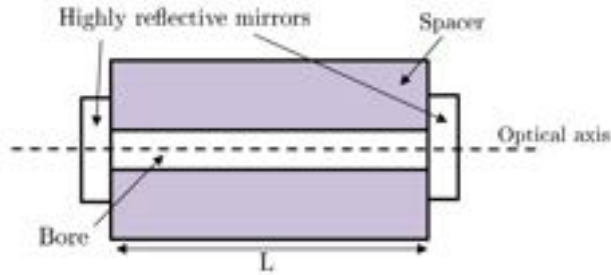
Figure 2: A diagram of a typical Fabry-Perot cavity.

There are other variations of optical cavities that can be utilised within optical systems, for example some optical cavities do not have a medium as a spacer and are free space cavities, where two mirrors are placed parallel to each other normally on mirror mounts. Another example is ring cavities where more than two mirrors (usually three mirrors), are incorporated to make the optical cavity. However for the work mentioned in this thesis only Fabry-Perot cavities with solid spacers are explored and discussed, as solid Fabry-Perot cavities have the added benefit of being easy to isolate from environmental vibrations.

Fabry-Perot cavities generally tend to have their optical axis vertically or horizontally placed. Depending if they are to be mounted as a vertical or horizontal optical cavity, can have a huge impact on the shape of the spacer, although a simple cylindrical design with the mirrors at either end of the cylinder can be optimally designed and mounted both vertically and horizontally. Nonetheless, when an optical cavity is vertically mounted a common geometric design that is normally made use of is a bicone shape (as it is symetrical and allows for simple vertical mounting), where the two mirrors are at either end of each cone similar to [4][5][6]. Where an optical cavity is horizontally mounted then usually the cavity will either be a cylindrical shape with two cuts-out so the spacer has a *mushroom* shape, similar to [7][8], or a cuboid shape that is either mounted flat as seen in [6] or at 45° as seen in [9]. These optical cavity shapes are carefully designed and optimised to ensure each cavity has a low stability. However, there are some uniquely shaped optical cavity spacers which have been developed and built, that have impressively low sensitivities. For example [10] has a cube shaped spacer, while [11] has a sphere shaped spacer. Both of these uniquely shaped optical cavities, exhibit extremely low acceleration sensitivities as later discussed. Within [12] is also a detailed exploration of a variety of shapes for optical spacers which is worth noting.

With the work mentioned here in this thesis, we start by discussing in Chapter 2, firstly the

background theory which is key to understanding optical cavities and how their physical properties initially affect the transmission from a cavity. In addition is a summary of how the electromagnetic radiation from lasers builds up within an optical cavity and a brief exploration into the Gaussian beam and the types of shapes, known as *modes* in which the circulating light could form within an optical cavity. This leads on to how the shape of each highly reflective mirror in a Fabry-Perot cavity and their radii of curvature affects the stability and configuration of a cavity, with a particular investigation on hemispherical configuration, which is the type of configuration that is implemented for each optical cavity discussed within this thesis. At the end of the chapter is a short introduction on the Pound-Drever-Hall stabilisation system and how its unique error signal is utilised within an optical system to ensure an optical cavity stays locked to the laser light.

Next in Chapter 3, is an analysis into the instabilities which cause the sensitivity of an optical cavity to increase and methods by which to keep them minimised. As the length of an optical cavity is directly linked to it's stability, any disturbances which cause any slight changes to the length of a cavity need to be kept to a minimum to reduce a cavity's sensitivity. At the beginning of the chapter is an introduction to the thermal expansion sensitivity and acceleration sensitivity, with a brief exploration on how ANSYS can be used to calculate the magnitude both of them have on the length of an optical cavity, and in particular how the optimum geometric shape can be found where the acceleration sensitivity is ultimately reduced. This leads on to descriptions of the vibrational sensitivity, pressure sensitivity and the thermal noise which all create fluctuations in the length of an optical cavity. In addition, is methods in which each stability could be minimised. At the end of the chapter is a look into the commonly used dielectric mirror coatings and a different type of single-crystal mirror coatings which display an exceptionally low Brownian motion, which would result in a reduced thermal noise in an optical cavity. Also there is a short investigation into the background vibrations which are present in an optical laboratory, including the vibrations that are present on the floor, an optical table, a vibration isolation platform and lastly on a rotational table, which was designed to test the portably of some of the cavities mentioned in this thesis.

The first optical cavity discussed in this thesis is introduced in Chapter 4, where a tunable cavity for a 2.6μm laser is described, with a detailed method about how the cavity was built. This unique cavity was designed and built to be used to stabilise a previously free running 2.6μm laser, which is being utilised within the experiment mentioned in [13] as a re-pumper laser for strontium atoms. Within the chapter is a complete description on the design on the cavity, with a step by

step method to how the cavity was constructed. There is also a detailed discussion on the vacuum system for the cavity, with again a step by step guide to how the cavity was placed and secured within the vacuum chamber.

This lends onto the second and third optical cavities which are discussed here. Chapters 5 and 6 introduce a novel type of optical cavity which utilises additive manufacturing techniques to create the spacers for more portable optical cavities. Both of these invar cavities are designed to be utilised within a strontium (Sr) optical clock, to stabilise the laser for the first stage of cooling of the Sr atoms, similar to the clocks mentioned in [14][15]. At the University of Birmingham is a research group in advanced material processing, led by Prof. Moataz Attallah, which specialises in Selective laser melting. The group researches a range of materials for this 3D printing technique and in particular an alloy, known as invar. Invar is an iron-nickel alloy which is notable for its incredibly low coefficient of thermal expansion (CTE) at room temperature. There are other materials which display similar or even better CTE than invar, which are commonly used as the material of an optical cavity spacer, for example ULE (ultra-low expansion glass) and NEXCERA, but unlike these materials, invar can be 3D printed in considerably more complex geometries, which expands the type of geometries that can be created.

This technique of 3D printing the spacers for optical cavities led to two novel ideas. The first being to have spacer and support as one solid component, here known as the "invar cavity", as shown in Figure 3a, where they are printed together, with the key benefit that the cavity would become reasonably portable, as the cavity could be directly and sturdily attached onto an optical table. This would make the "invar cavity" considerably more portable, when compared to an optical cavity that is mounted onto viton balls, as the cavity would not be able to be misaligned.

(a)

(b)

Figure 3: Photos of both invar optical cavities built during the work mentioned in this thesis, using additive manufacturing with, (a) the invar cavity and (b) the invar lattice cavity.

The second idea is that instead of having the spacer as a solid piece, is to incorporate an internal lattice within the spacer. By implementing a lattice added within the spacer, it would result in a reduction in the weight of the optical cavity, while retaining the stiffness of the initial solid spacer. By decreasing the weight of the optical cavity it would consequently mean that the cavity would bend under gravity less, reducing the acceleration sensitivity in the cavity. As shown in 3b, the lattice cavity was built to be a vertical cavity, by utilising the bicone space shape.

The last two optical cavities mentioned in Chapters 7 and 8 have diamond spacers, and both display especially low acceleration sensitivities. At the moment one of the lowest passive acceleration sensitivities reported for an optical cavity is 2.5×10^{-11}/g which is an ultra low expansion glass (ULE)-silica cavity, with a cube shaped spacer, as mentioned in [10] where g is the acceleration due to gravity on the surface of the Earth in ms^{-1}. In addition there is also a sphere shaped cavity that is a ULE/FS (fused silica) that without active feed-forward correction, displays an acceleraltion sensitivity along the orthogonal axes of $4.0/16/31 \times 10^{-11}$/g, as found in [11]. Here we introduce a thin diamond-diamond optical cavity and diamond-FS optical cavity which from simulated results display acceleration sensitivities as low as $\approx 9 \times 10^{-15}$/g along one orthogonal axis. With the diamond-diamond having an acceleration sensitivity in the y axis (vertical mounted) of $\approx 1.5 \times 10^{-11}$/g and $\approx 4 \times 10^{-14}$/g / $\approx 5.5 \times 10^{-13}$/g in the x and z axes (horizontally mounted), respectively. While the diamond-FS (fused silica) cavity is found to have an acceleration sensitivity in the three orthogonal axes of $\approx 2/5 \times 10^{-13}$/g and 9.25×10^{-15}/g (with 9.25×10^{-15}/g found when the cavity is mounted vertically).

As fully discussed in Chapter 7, the diamond-diamond cavity makes use of a thin circular double bevel cut design for the diamond spacer and has wide, thin diamond mirrors. Within the chapter is a detailed exploration on how the geometry of both the spacer and mirrors affect the acceleration sensitivity of the cavity, with the final optimal geometric sizes for each component. As well as small focus of the possibility of using four ULE rings to minimise the effect of the thermal expansion sensitivity that the cavity would experience around room temperatures.

The diamond-FS cavity is described in Chapter 8, with a background discussion on the Poisson ratio and fracture planes present in diamond, as both are found to have an impact on the optimal geometric design, for where the cavity is least affected by the acceleration sensitivity. At the end of the chapter is a brief analysis on the size of the fused silica (FS) mirrors, with the final diamond spacer dimensions and the next steps in how the cavity will be built and mounted.

2   Optical Resonators

An optical resonator or cavity is a vessel for storing photons for a period of time. The simplest type is referred to as a Fabry-Perot cavity which consists of two highly reflective mirrors facing one another. It is worth noting that there are other more complex geometric cavities that can be utilised, for example, ring cavities, which consist of three or more mirrors but for the work mentioned in this chapter and in this thesis only Fabry-Perot cavities are discussed and explored. In this chapter is a brief discussion on the fundamental properties of Fabry-Perot optical cavities and how they directly affect the characteristics of the transmitted light, as well as a discussion on the photon lifetime within an optical resonator.

Then Gaussian beams are introduced, along with the paraxial wave equation and the key properties of Gaussian beams that are in relation to optical cavities including the Gaussian beam parameters and the Gouy phase shift. This then leads on to Section 2.4 where the modes that can be present within an optical resonator are discussed and in particular Hermite-Gaussian modes. The stability condition of optical cavities is then discussed and how different types of optical resonator configurations fit within the condition, with detailed descriptions of the near-concentric and hemispherical configurations.

Lastly the Pound-Drever-Hall stabilisation method is introduced and how the method could be utilised within an optical system to "lock" the laser light's frequency to an optical cavity. Where firstly is a discussion on how the length of an optical cavity can be varied and the secondly is a discussion on how the frequency of the laser light can be varied, until constructive interference occurs and is kept consistent in the light within an optical cavity.

2.1   Fundamental Properties

There are a number of key physical properties that an optical resonator has, including the free spectral range, linewidth, finesse and Q factor. All of these properties have an effect on the light that is transmitted from an optical resonator. Depending on the application of the laser light that is required, will highly depend on what values the resonator will need for each property. For example, an optical cavity used for the clock laser in a Sr optical clock requires an incredibly high finesse and a stability of ≈ 1Hz, while the cavity used for the first stage cooling of Sr atoms only requires a stability of $\approx$1MHz (value discussed in Section 5.7). It is therefore key to consider all of these properties in relation to the application of an optical cavity in the early designing stages.

2.1.1 Transmission and Reflection

Firstly, before looking into the key properties of an optical resonator it is important to understand how light builds up within a resonator and how it is transmitted. When the light enters an optical resonator it will either constructively interfere when the length of the resonator, L is equal to an integer or half integer number of wavelengths, λ, or the light can destructively interfere or neither. If the light that enters a resonator is neither significantly constructively or destructively interfering then the laser light will simply circulate the resonator a number of times before being transmitted as scattered light, with the amount of light being transmitted from each mirror being proportional to the reflectance of each mirror.

Once the light enters the resonator the amount of reflectance and transmittance by each mirror is based on the reflection coefficients of the mirrors, r_1 and r_2, as shown in Figure 4, where $I_{incident}$ is the incident light intensity.
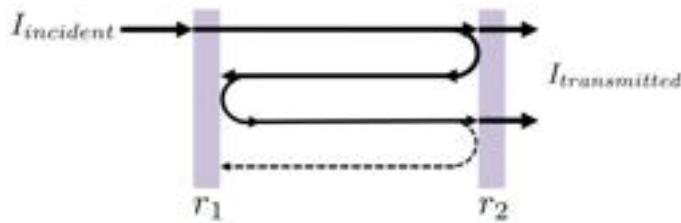
Figure 4: Model of the path light takes within a Fabry-Perot optical resonator, where r_1 and r_2 are the reflection coefficients of each highly reflective mirror and $I_{incident}$ and $I_{transmission}$ are the intensity of the incident light and transmitted light, respectively.

Due to optical cavities requiring highly reflective mirrors, the majority of the laser light that enters an optical resonator, along the optical axis, will reflect a large number of times between the mirrors until being transmitted from the resonator. However, there will still be a minuscule proportion of the light being reflected off the first mirror, before even entering the resonator, as well as a small proportion of light being transmitted at each mirror per each round trip of the light.

The transmitted intensity of light for a resonator, can be found using:

$$I_{transmitted} = I_{incident} \frac{(1 - r_1 r_2)^2}{(1 - r_1 r_2)^2 + 4 r_1 r_2 \sin^2(kL)} \tag{1}$$

where $I_{transmitted}$ is the intensity of the transmitted light and $k = m\pi/L$ [16]. When constructive interference is occurring within an optical resonator then m is an integer and is defined as the *cavity mode*. Additionally when both mirrors have equal reflection coefficients $(r_1 = r_2)$ then the

transmitted light can simplified to:

$$I_{transmitted} = I_{incident} \frac{(1-R)^2}{(1-R)^2 + 4R\sin^2(kL)}, \tag{2}$$

where $R = r_1 r_2$. As the wavelength of light, λ and the frequency of light, v are related through $v = c/\lambda$, the intensity of the transmitted light when constructive interference is occurring is found to have peaks at certain frequencies, known as the *resonant frequencies* of resonator. With the frequency separation of these peaks known as the free spectral range of the resonator.

2.1.2 Free Spectral Range

For an empty Fabry-Perot resonator with length L, a standing wave will arise if the light is constructively interfering (when $L = m(\lambda/2)$). After light completes round-trip $2L$ of an optical resonator and with $k = m\pi/L$ as discussed in chapter 2.1.1, it is found that:

$$L = \frac{m\lambda}{2} \qquad with \qquad m \in \mathbb{Z}. \tag{3}$$

Resulting in the resonant frequencies of a resonator being able to be calculated using:

$$v_m = m\frac{c}{2L}. \tag{4}$$

The frequency spacing between the modes is then found with

$$v_{FSR} = v_{m+1} - v_m = \frac{c}{2L}, \tag{5}$$

which is otherwise know as the Free Spectral Range (FSR), v_{FSR}, of an optical resonator or cavity and is visually represented in Figure 5. However, for a resonator which contains a medium, the FSR needs to consider the refractive index n of the medium. Such is calculated with

$$v_{FSR} = \frac{c}{2Ln}. \tag{6}$$

2.1.3 Full Width at Half Maximum (Linewidth)

The full width at half maximum v_{FWHM} of a frequency peak in a resonator's transmission, otherwise known as the resonator's linewidth is simply the width of each transmitted spectral peak at half the total transmitted intensity as shown in Figure 5. It can be used along with the free spectral range to calculate an optical resonator's finesse experimentally, as it is the ratio of v_{FWHM} and v_{FSR}:

$$F = \frac{v_{FSR}}{v_{FWHM}}. \tag{7}$$

26
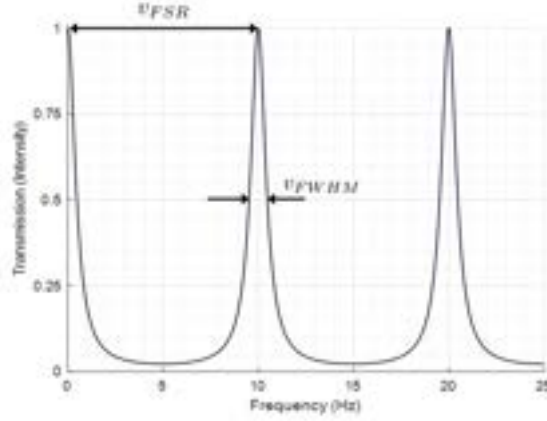
Figure 5: Transmission intensity of an optical resonator with mirror reflection coefficients, r_1, r_2 both equal to 0.85 and a Free Spectral Range, v_{FSR} of 10Hz. Where v_{FWHM} denotes the linewidth.

2.1.4   Finesse

An optical resonator's finesse is dependent on the reflection coefficients, r_1 and r_2 of the mirrors and on other factors which cause loses with in a resonator, for example from the scattering of light within a bore due to the presence of gas atoms. However, when a resonator is under vacuum and it is assumed the bore is completely empty and there are no other factors causing loses within a resonator, it's finesse can be defined by

$$F = \frac{\pi\sqrt{R}}{1 - R} \tag{8}$$

assuming $r_1 r_2 = R$ for a symmetrical resonator, i.e. the amplitude of the wave is reduced by a factor of R on each round trip. The effect of finesse on the resonator transmission is shown in Figure 6.

27
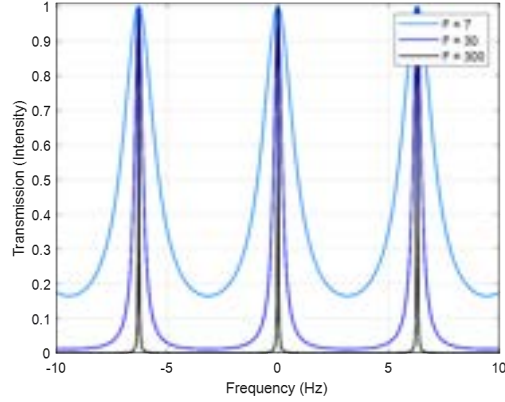
Figure 6: Transmission intensity of an optical resonator with different resonator finesses, where F denotes finesse, for a direct comparison.

2.1.5 Q-factor

The quality or Q-factor of an optical resonator describes the amount of damping within the system. There are two methods of obtaining the Q-factor of a resonator. The first is by calculating the ratio of the resonance frequency v and the full width at half maximum v_{FWHM}:

$$Q = \frac{v}{v_{FWHM}} \tag{9}$$

The relation between Q-factor and finesse can found by using the definition of finesse from equation 7,

$$Q = \frac{vF}{v_{FSR}} = \frac{2LvF}{c} = \frac{2LF}{\lambda} \tag{10}$$

Secondly, is the energy stored within the resonator. If a resonator has a high Q-factor, then the rate at which the energy is lost from the system compared to the amount of energy stored in the system will be low. The definition is be used to calculate the Q-factor by [17]

$$Q = 2\pi \frac{(stored\ energy)}{(energy\ loss\ rate)} = 2\pi \frac{\epsilon}{d\epsilon/dt} \tag{11}$$

where ϵ is the stored energy within the resonator. Where Q is also equal to:

$$= 2\pi v \tau_{photon} \tag{12}$$

where τ_{photon} is the photon lifetime.

2.2 Photon lifetime

The mirrors of an optical resonator cannot have 100% reflectivity, resulting in the incoming photons having a *photon lifetime* within the resonator. The reflection coefficient of each mirror, r,

28

will have a value from zero to one, such that if the mirror is completely transmitting r would be equal to zero and if the mirrors could be completely reflecting, r would equal one. The photon lifetime is not only dependent on the reflectivity of the mirrors but also the length of the resonator L and refractive index n. So that the photon lifetime is defined as:

$$\tau_{photon} = \frac{2nL}{c(1-s)} = \frac{\tau_{roundtrip}}{(1-s)},$$ (13)

where s is the survival factor, which is defined for a two mirrored resonator $s = r_1 * r_2$ and $\tau_{roundtrip} = 1/v_{FSR}$ is the time it takes a single photon to do a "round-trip" within the resonator.

2.3   Gaussian Beam

In optics, the Gaussian beam is a type of electromagnetic beam that lasers often generate. Its mathematical form is used in describing and analysing laser beams and is widely used in Gaussian optics and similar optical systems. In this sub-chapter is an introduction to the paraxial wave equation and its approach to the analysis of optical beams in free space, as well as a short review of some of the important properties of the Gaussian beam which relate to optical cavities.

2.3.1   Paraxial Wave Equation

A method to study the geometric behaviour of Guassian beams within optical systems is called Gaussian optics. Within Gaussian optics is a technique that uses the Paraxial Wave equation to describe the free-space wave propagation, this method can describe almost all laser amplification and laser propagation and therefore is commonly used for laser optics calculations. A detailed derivation can be found in [3]. To summarise this derivation: it can be obtained by starting with the Helmholtz equation:

$$\nabla^2 u + k^2 u = 0.$$ (14)

Where ∇^2 is the Laplacian, k is the propagation constant of the medium ($k = 2\pi/\lambda$) and u is the phasor potential or amplitude of the field distribution in sinusoidal time, when the optical beam is propagating in the z direction:

$$u = \psi(x, y, z)e^{-ikz}.$$ (15)

Such that e^{ikz} is the main spatial dependence of u and where ψ is the complex-valued wave amplitude which represents the transverse beam propagation.

By substituting Equation 15 into Equation 14 the wave equation is found to be:

$$\frac{\partial^2}{\partial x^2}\psi + \frac{\partial^2}{\partial y^2}\psi + \frac{\partial^2}{\partial z^2}\psi - 2ik\frac{\partial}{\partial z}\psi = 0.$$ (16)

As $\psi(x, y, z)$ has a much lower variation on z than x or y, it can be expressed mathematically by the paraxial approximation:

$$\frac{\partial^2}{\partial z^2}\psi \ll \frac{\partial^2}{\partial x^2}\psi, \frac{\partial^2}{\partial y^2}\psi, 2k\frac{\partial}{\partial z}\psi, \tag{17}$$

then the wave equation is reduced by the paraxial approximation to:

$$\frac{\partial^2}{\partial x^2}\psi + \frac{\partial^2}{\partial y^2}\psi - 2ik\frac{\partial}{\partial z}\psi = 0. \tag{18}$$

This equation is referred to as the Paraxial Wave equation and it plays an important role in optics as it describes the propagation of light (electromagnetic waves) in Gaussian beams, which is the form most laser beams take.

2.3.2 Gaussian Beam Parameters

Gaussian-spherical beams (Gaussian beams) are expressed as a solution of Equation 18 [3]:

$$\psi(x, y, z) = \frac{1}{q(z)} exp\left[-\frac{x^2 + y^2}{w^2(z)} - ik\frac{x^2 + y^2}{2R(z)} \right], \tag{19}$$

where $w(z)$ is the beam radius (defined at $1/e^2$ intensity), $R(z)$ is the radius of curvature of the beam's wavefronts at z and $q(z)$ is the complex beam parameter. The complex beam parameter is then related to the beam radius $w(z)$ and the radius of curvature $R(z)$ by:

$$\frac{1}{q(z)} \equiv \frac{1}{R(z)} - \frac{i\lambda}{\pi w^2(z)}. \tag{20}$$
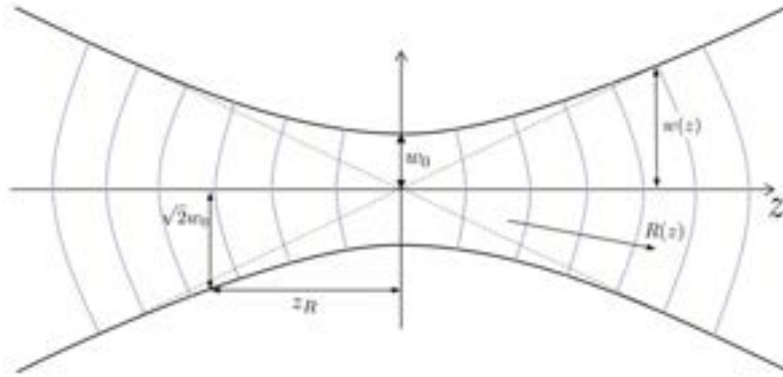
Figure 7: A model of the propagation of a Gaussian beam with parameters: beam waist w_0 (where the beam radius is the smallest), beam radius $w(z)$ at z (defined at $1/e^2$ intensity), radius of curvature $R(z)$ of the beam's wavefronts at z and z_R is the Rayleigh range.

Which in free space obeys the propagation law:

$$q(z) = q_0 + z = \frac{i\pi w_0^2}{\lambda} + z \tag{21}$$

Where $q_0 = (i\pi w_0^2/\lambda)$ and is the initial value of the complex beam parameter at the position of the beam waist, w_0 (where the beam radius is the smallest). Both the beam radius $w(z)$ and radius of curvature $R(z)$ can then be derived by combining the definition of the complex beam parameter, $q(z)$ (Equation 20) to Equation 21 to give:

$$w(z) = w_0\sqrt{1 + \left(\frac{z}{z_R}\right)^2} \tag{22}$$

$$R(z) = z\left[1 + \left(\frac{z_R}{z}\right)^2\right], \tag{23}$$

as shown in Figure 7. Where w_0 is the beam waist and z_R represents the Rayleigh range which is defined by:

$$z_R = \frac{\pi w_0^2}{\lambda} \tag{24}$$

All the key parameters of the Gaussian beam (Equations 22, 23 and 24) are therefore related to the beam waist w_0 and the z/z_R ratio and are only a valid approximation of the Gaussian beam if $\lambda \ll w_0$. Therefore, the complete Gaussian beam propagation can be mapped out by just the beam waist w_0 and the wavelength of the light in the medium λ.

2.3.3 Gouy Phase Shift

When a Gaussian beam passes through a focused point (i.e. at the beam waist w_0) an additional phase shift occurs in the propagation of the Gaussian beam. This phase shift at position z is known as the Gouy phase shift, $\zeta(z)$ [18]:

$$\zeta(z) = tan^{-1}\left(\frac{z}{z_R}\right) \tag{25}$$

resulting in the apparent wavelength being increased close to the waist and the phase velocity in that area being larger than the speed of light.

The shift increases the distance between the wave fronts, compared to the wavelength of a plane wave with the same frequency. So the phase front must propagate faster in order to compensate, so the local phase velocity is increased.

For higher order modes the Gouy phase shift is stronger, causing the resonance frequencies in optical resonators for higher order modes to be slightly higher. So the Gouy phase shift has a large impact on the beam quality within resonators due to lifting the frequency degeneracy of resonator modes.

2.4 Hermite-Gaussian Modes

Modes are formed when the intensity profile of a Gaussian beam does not change during propagation. As for particular electric field amplitude distributions, the shape of the profile stays

consistent even if the optical power or scale of the profile is altered throughout propagation. Modes are calculated as solutions of the Paraxial Wave equation. They are separated into families depending on the type of coordinates. Laguerre-Gaussian modes are expressed using cylindrical coordinates, r and θ, whereas the Hermite-Gaussian modes have rectangular geometry and are within a Cartesian coordinates system, using x and y [3]. The majority of real lasers will oscillate in the rectangular modes as they tend to contain components at such angles that they break the rotational symmetry.
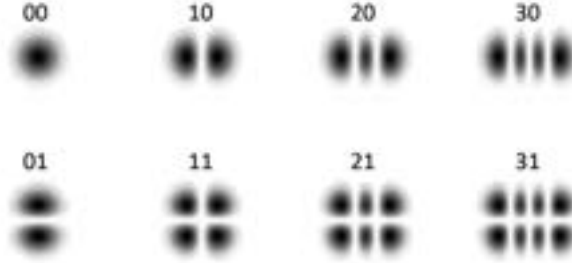
Figure 8: Lowest order Hermite-Gaussian modes intensity distribution.

Hermite-Gaussian modes in free space are typically shown as TEM_{nm} solutions. (Where TEM is transverse electro-magnetic). These solutions are written in either x or y transverse dimensions with the e^{ikz} phase shift factor in the form

$$u_n(x,z) = \left(\frac{\sqrt{2/\pi}}{2^n n! w(0)} \right)^{1/2} \left(\frac{q_0}{q(z)} \right)^{1/2} \left[\frac{q_0}{q_0^\star} \frac{q^\star(z)}{q(z)} \right]^{n/2} H_n \left(\frac{\sqrt{2}x}{w(z)} \right) \exp \left[-ikz - i\frac{kx^2}{2q(z)} \right] \quad (26)$$

where $q(z)$ and $w(z)$ are the same parameters as described earlier. H_n are the Hermite polynomials of order n. From Equation 26 the Hermite-Gaussian modes in two transverse dimensions can be written as

$$u_{nm}(x,y,z) = u_n(x,z) \times u_m(y,z) \quad (27)$$

2.5   Types of Resonators and the Stability condition

The geometry of a Fabry-Pérot optical resonator has a significant effect on its stability, with the resonator configuration depending on the radii of curvature $R_{1,2}$ of the mirrors and the position of the mirrors $z_{1,2}$ with relation to the beam waist, such that the length of the resonator is $L = z_2 - z_1$. When the radii of curvatures ($R_1 = R_2$) and the positions of the mirrors ($z_1 = -z_2$) are identical then the resonator is referred to as a symmetrical resonator. If either of these variables are not equal then the resonator is seen to be asymmetrical.

The geometric quantities of resonators are normally described in terms of the g-parameters:

$$g_1 = 1 - \frac{L}{R_1}, \qquad g_2 = 1 - \frac{L}{R_2}. \tag{28}$$

Subsequently by using these parameters one would find:

$$w_0^2 = \frac{L\lambda}{\pi} \sqrt{\frac{g_1 g_2 (1 - g_1 g_2)}{(g_1 + g_2 - 2g_1 g_2)^2}} \tag{29}$$

$$w_1^2 = \frac{L\lambda}{\pi} \sqrt{\frac{g_2}{g_1 (1 - g_1 g_2)}} \tag{30}$$

$$w_2^2 = \frac{L\lambda}{\pi} \sqrt{\frac{g_1}{g_2 (1 - g_1 g_2)}} \tag{31}$$

where w_0 is the beam waist and w_1, w_2 are the beam spot sizes on each mirror. In order for an optical resonator to be stable the following must be valid:

$$0 \leq g_1 g_2 \leq 1 \tag{32}$$

as shown in Figure 9 [3][19]. As observed in the graph the confocal design sits at the point (0,0). It is the most stable configuration and when the resonator length fluctuates its stability changes along the diagonal line $x = y$, which all symmetrical resonators sit on. Both the plane-parallel and concentric configurations sit on this line but they are on the stability border, resulting in them both being only marginally stable, thus being very susceptible to become unstable. In this thesis two types of resonators were used, plane-parallel and near concentric. In the following is a detailed description of the near-concentric configuration.
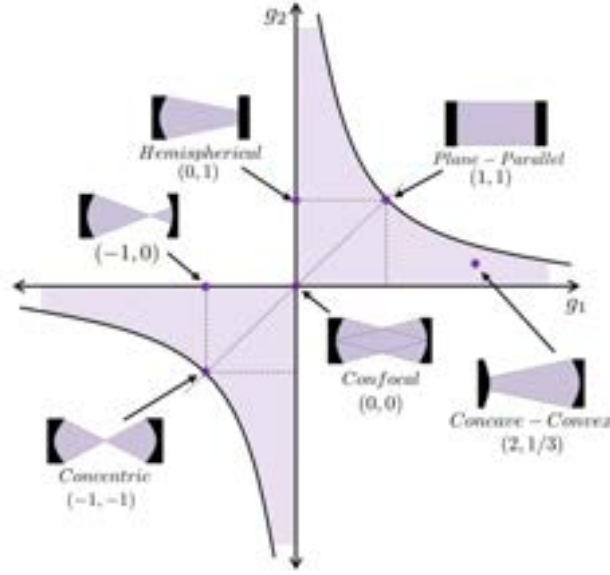
Figure 9: Resonator stability graph displaying where different resonator configurations are positioned depending on their stability, where the shaded range refers to $0 \leq g_1 g_2 \leq 1$ i.e. the stable region. Adapted from [3].

2.5.1 Near-Concentric Configuration

Near-concentric resonators are defined when the length L of the resonator is slightly less than the sum of the two radii $R_1 + R_2$ by ΔL thus [3]:

$$R_1 \approx R_2 \approx R = L/2 + \Delta L/2. \tag{33}$$

Resulting in the resonator being extremely close to the boundary of the stability region, such that it can be assumed to be on the boundary. The configuration of the resonator is as displayed in Figure 10. Due to these parameters, Equations 29, 30 and 31 can be approximated to:

$$w_0^2 \approx \frac{L\lambda}{\pi} \times \sqrt{\frac{\Delta L}{4L}} \tag{34}$$

$$w_1^2 = w_2^2 \approx \frac{L\lambda}{\pi} \times \sqrt{\frac{L}{4\Delta L}} \tag{35}$$

for $\Delta L \ll L$. As the resonator is on the stability boundary it is highly sensitive to misalignment, so any tilt in the mirrors will cause a large alteration in the optical axis. The unique shape of this resonator means they have a significantly small spot size (waist) in the centre of the resonator, with large spot sizes at the mirrors due to an increase in the beam divergence.

34
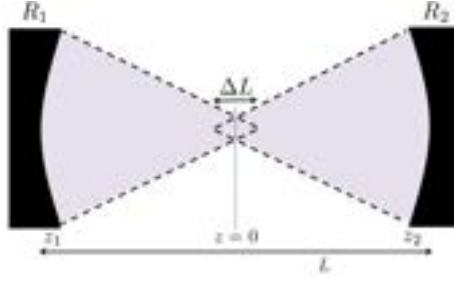
Figure 10: Near-Concentric Resonator configuration.

2.5.2 Hemispherical Configuration

Hemispherical resonators, also known as half-symmetric resonators are outlined when one mirror, R_1 is curved, with a defined radius of curvature and the opposite mirror is planar, $R_2 = \infty$, as shown in Figure 11. Such that:

$$g = g_1 = 1 - L/R_1 \tag{36}$$

$$g_2 = 1. \tag{37}$$

Where $1 \leq g_1 \leq 0$ in order for the resonator to be within the stable region on the stability graph. For this type of configuration the resonator waist is found on the planar mirror, in this case the second mirror. With the waist, ω_0 and the larger spot size, ω_1 being [3]:

$$\omega_0^2 = \omega_2^2 = \frac{L\lambda}{\pi} \sqrt{\frac{g}{1-g}} \tag{38}$$

$$\omega_1^2 = \frac{L\lambda}{\pi} \sqrt{\frac{1}{g(1-g)}}. \tag{39}$$
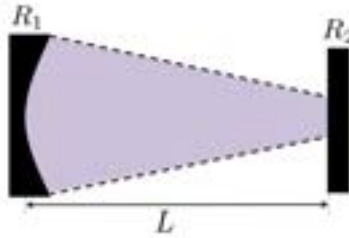
Figure 11: Hemispherical Resonator configuration.

This configuration is utilised for each resonator that is mentioned and designed, in relation to the work discussed in this thesis. As this configuration has the benefit that any small adjustments made to the length of a resonator, will cause the resonator to simply move along the y-axis of the

35

stability condition as shown in Figure 9 and not nudge the resonator out of the stability range, making the configuration reasonably protected against instabilities that cause length fluctuations in a resonator. Another benefit is that this type of configuration has good frequency separation between the optical modes, resulting in it being easy to lock to a single mode at a time.

2.6   Pound-Drever-Hall Stabilisation

Commonly lasers are locked to optical cavities using the Pound-Drever-Hall (PDH) method (where the cavity is *locked* when resonance is achieved i.e. the length of the cavity is equal to an integer number of wavelengths) and can be approached using two slightly different methods. The first method involves locking the length of the cavity to a reasonably stable laser, by making micro adjustments to the length of the cavity.

When a cavity has an adjustable length, then the overall length of the cavity is slowly varied till resonance occurs. Usually the length of a cavity is altered using piezo-actuators (more information found in Chapter 2.6.3) attached to either one or both mirrors (or all mirrors in a ring cavity), allowing for the length of the cavity to be slowly varied by applying voltages though the piezo-cubes, enabling micro or nano-metre adjustments in the length of the cavity.

The second approach requires locking the laser frequency to a fixed length cavity by altering the frequency of the laser light. For a fixed length cavity the laser frequency is altered until the laser light is at resonance with the cavity. Typically, for this method a laser diode is used, where the frequency of the laser light is usually adjustable by simply adjusting the incoming current to the laser.

2.6.1   Error signal

What makes the PDH method unique is it's error signal. As just by looking at the transmission power of a cavity it is impossible to determine whether a change in the transmission is simply a power fluctuation or an actual frequency shift. To overcome this you can observe the reflected light from the cavity using the PDH method, where a general diagram of the PDH set-up is shown in Figure 12. If light is resonant to the cavity then the reflection will be nearly zero and the incoming laser power will have no effect. But if a reflected light is detected, it is not possible to work out if the laser frequency is under or over the required resonant frequency. This is where the error signal from the Pound-Drever-Hall (PDH) method [20] comes into use. The PDH method modulates the light by implements two sidebands either side of the carrier frequency [22] using an phase modulating electro optic modulator (EOM), before the light enters the cavity, where the magnitude of the sidebands is controlled by the amplitude applied to EOM. By

observing the reflected light from the cavity and mixing it with the initial modulation frequency, then this causes a phase change in the reflected light, which is referred to as the error signal. As the reflected light from the cavity is used during the PHD method instead of the transmitted light (as the sidebands are very small in the transmission of a high finesse optical cavity, and therefore a small error signal would be observed), the optical path is altered using a polarising beam slitter (PBS) and a quarter wave plate ($\lambda/4$). Resulting in the light entering the cavity being circularly polarised from linearly polarised. As the light is reflected in the cavity this reverses the circular polarisation of the light, then as the light leaves the cavity it travels through the quarter wave plate making the light the linearly polarised again and now orthogonal to the incoming light. Therefore, when the light passes through the PBS, it is reflected into the photodetector, to allow the light to be mixed with the initial modulated light to produce the error signal. This error signal is then transmitted through a servo amplifier and into the laser to alter the laser frequency to pull the cavity back into resonance [23].
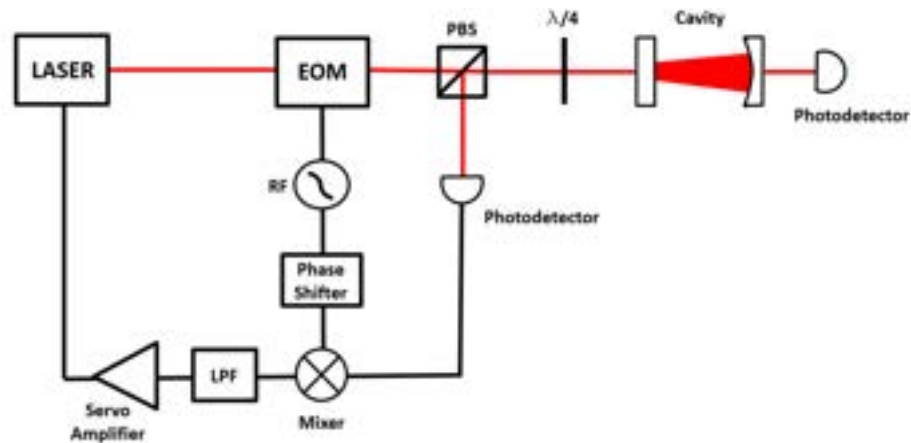
Figure 12: An optical set-up for Pound-Drever-Hall-Stabilisation, where the red lines are optical paths and the black are electronic paths. With EOM for an electro-optical modulator, LPF for a low-pass filter and PBS for a polarising beam splitter. Adapted from [23].

Another method to lock an optical cavity is referred to as the side of fringe lock, which has the added benefit of not requiring an EOM.

2.6.2 Fluctuating the cavity length

For the method where the length of the cavity is fluctuated until the length of the cavity is locked to the laser frequency, the cavity needs to be adjustable for the entire free spectral range of the cavity. For this kind of range in length piezoelectric crystals are commonly utilised as discussed

below.

2.6.3 Piezoelectric-crystals

In 1880, the Curie brothers, Jacques and Pierre revealed their discovery of the piezoelectric effect [24][25]. By looking into crystal structures, including topaz and quartz, they found that by adding pressure to the structures, an electric charge is generated from the crystals. Likewise, later on it was discovered that in reverse, when an electric field is applied to these crystals, that the crystal structures are deformed by the field.

However, these natural mono-crystalline materials only exhibit small displacements, making their practical uses very limited. It was only until around 1950 when piezoelectric ceramics were originally put to use [26], that the piezoelectric effect was expanded into different industries. The most common piezoelectric ceramics used today are based on Lead Zirconate Titanate $(Pb(Zr,Ti)O_3:PZT)$[26]. This is the same material that ThorLabs use for their in-house piezoelectric manufacturing [21]. The piezoelectric chips which ThorLabs manufacture are ideal for tuning the length of an optical cavity, using PDH, as they are milli-scale relatively low voltage piezoelectric chips, that display displacements around $0.7\mu m - 3.6\mu m$, when potential voltages are applied to them.

3 Optical Cavity Design Considerations

When a laser is locked to an optical cavity its length stability is directly related to the frequency stability of the laser through:

$$\frac{\Delta L}{L} = \frac{-\Delta v}{v},\tag{40}$$

where L is the length of the cavity and v is the frequency of the laser light [27]. This direct relation highlights the importance of making the length of the cavity as stable as possible. There are a number of sources of perturbations which affect the length of an optical cavity, including gravitational forces, temperature fluctuations and other external forces. For each perturbation, there are design considerations that are required in order to minimise the length instability that each perturbation causes, as ultimately, the stability of any optical cavity is limited by how much each perturbations impacts a cavity's length.

In this Chapter is a detailed discussion on firstly the thermal expansion of materials and it links to the thermal expansion sensitivity in optical cavities. Then a discussion on how by carefully selecting the materials for both the spacer and the mirrors for an optical cavity and through temperature control methods, the thermal expansion sensitivity can be minimised. This leads on to an exploration on how the gravitational pull affects optical cavities and produces an acceleration sensitivity. In addition for both of these sub-chapters, is an analysis on how the use of finite element analysis in ANSYS can be used to calculate and find the optimum design which minimises the thermal expansion sensitivity and acceleration sensitivity in optical cavities.

Then there is a brief discussion on the vibrational sensitivity, pressure sensitivity and thermal noise (caused by the Brownian motion of particles) and how these sources cause perturbations and individually affect the length of an optical cavity, as well as methods to reduce the impact each of them have on the length of an optical cavity.

This leads on to an introduction of optical mirrors and their coatings, with a discussion on the commonly utilised dielectric coatings and their structure. As well as a brief description on a new type of single-crystal coatings which displays an exceptionally low Brownian motion, which in turn would have a huge impact on reducing the thermal noise in an optical cavity.

Lastly is a brief investigation to the magnitude of background vibrations that are present on the floor, an optical table and on a rotational table within the laboratory. As well as a look into how the use of a minus k platform could be utilised to further protect an optical system from the background vibrations.

3.1 Thermal Expansion Sensitivity

When most solid materials experience a net increase in temperature, they expand and vice versa when cooled, contract. So, when the temperature, T of a solid material is changed, the length change, Δl of the solid material is found using:

$$\frac{l_2 - l_1}{l_1} = \alpha_0 (T_2 - T_1) \tag{41}$$

or

$$\frac{\Delta l}{l_1} = \alpha_0 \Delta T. \tag{42}$$

Where l_1 and l_2 are the initial and final lengths respectively and T_1 and T_2 are the initial and final temperatures [33][40]. α_0 is known as the linear coefficient of thermal expansion, which is unique for each material and denotes how much a material changes in size per degree change in temperature, where the pressure is kept constant. Equations 41 and 42 refer to the thermal expansion in only one linear direction, whereas in practice a material will vary in size in all directions, resulting in an overall change in volume, V. With T_1 and T_2 as the initial and final temperatures respectively, the change in volume is determined using:

$$\frac{V_2 - V_1}{V_1} = \alpha (T_2 - T_1) \tag{43}$$

or

$$\frac{\Delta V}{V_1} = \alpha \Delta T, \tag{44}$$

where V_1 and V_2 are the initial and final volumes and $\Delta V = V_2 - V_1$. α represents the volume coefficient of thermal expansion which for most materials is a positive value, but in some cases can be negative. The most notable negative coefficient of thermal expansion is water at $\approx 0 - 4°C$, where it slightly contracts in volume, as its temperature is increased within this range. For optical cavities the length change which occurs with variations in temperature is referred to as the thermal expansion sensitivity (or thermal sensitivity). The effect directly reduces the stability of optical cavities but it can be reduced by using materials with especially low coefficients of thermal expansion. Some of the most common materials used are ultra-low expansion (ULE) glass, sapphire, and NEXCERA. Which all display a zero crossing in their coefficients of thermal expansion at certain temperatures. For sapphire it displays a zero crossing in its coefficient of thermal expansion at cryogenic temperatures [28][29], resulting in cavities using sapphire needing to be radically cooled down, to experience a low thermal sensitivity. Whereas, ULE and NEXCERA [30][4] both display a zero crossing in their coefficients of thermal expansion close to room temperature, making the materials considerably easier to work with. ULE is a titania

silicate glass and displays a coefficient of thermal expansion of $0 \pm 30 \times 10^{-9}/^\circ$ C at 5°C to 35°C [31]. Its coefficient of thermal expansion does however vary with temperature and can approximately be found using

$$\alpha(T) = a(T - T_0) + b(T - T_0)^2 \tag{45}$$

where a is normally around $1.8 \times 10^{-9}/^\circ C^2$ and b is approimately $-10 \times 10^{-12}/^\circ C^3$ [27].

Table 1: Material Properties for ULE [31] and Fused silica [41]

	ULE	Fused Silica
Density	2210 kgm^{-3}	2203 kgm^{-3}
Young's Modulus	67.6 GPa	73.6 GPa
Poisson's Ratio	0.17	0.17
Coefficient of Thermal Expansion	$0 \pm 30 \times 10^{-9}/^\circ$C	$0.55 \times 10^{-6}/^\circ$C

As a result, commonly optical cavities are built with a ULE spacer and Fused silica (FS) mirrors with the material properties displayed in Table 1, where the mirrors are optically contacted to the spacer (Fused silica is used for the mirrors as it has a small thermal noise (Brownian motion)). These types of cavities show a minimised thermal expansion just below room temperature.

(a)   (b)
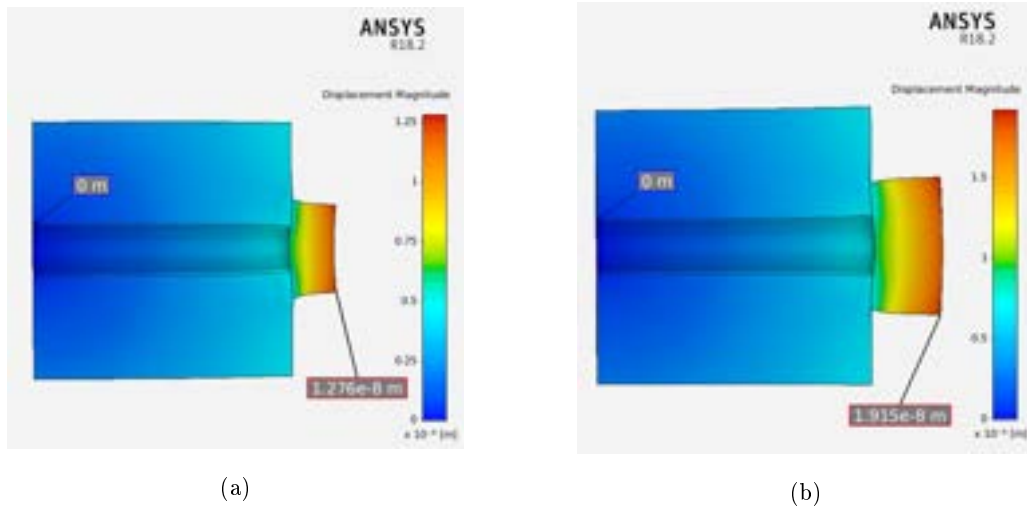
Figure 13: Displacement contour diagrams displaying the thermal expansion of an optical cavity, with an ultra-low expansion(ULE) spacer and Fused Silica (FS) mirror, optically contacted together - (a) at 20°C and (b) at 25°C. Due to symmetry within the cavity, only a quarter of the cavity is simulated. The scale is on the right-hand side of each figure.

The effect of thermal expansion in these types of cavities is shown in Figure 13, where (a) shows the FS mirror contracting at 20°C and vice versa, expanding at 25°C in (b). This directly displays how different temperatures can alter the length between the two mirrors causing a cavity to lose stability.

The axial bending for ULE/FS cavities is however also increased due to the mixing of the two materials, but as shown in Figure 14 the fractional length change between the mirrors displays a zero crossing in its gradient at ≈10°C, which denotes where the cavity's thermal expansion is ultimately minimised.
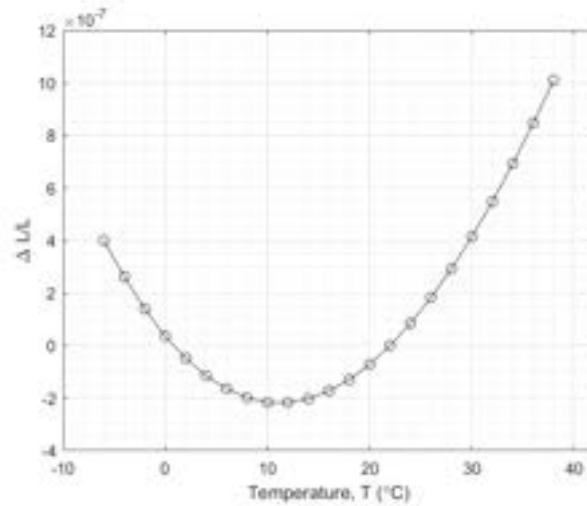
Figure 14: Thermal expansion of an optical cavity with a ULE spacer and FS mirrors, with the fractional length change, $\Delta L/L$ versus the temperature, T (°C). Where the spacer has a length of 60mm, diameter of 30mm and a bore diameter of 6mm and the mirrors have length of 6.35mm and diameter of 12.7mm. Data from simulations computed on ANSYS.

To push the temperature in which the cavity experiences a zero thermal expansion more towards room temperature, a ULE ring can be optically contacted to the back of each FS mirror, as described in [27].

3.2 Acceleration Sensitivity

All materials bend when a force (for example gravity) is applied to them, but how much they bend depends on numerous features of the material, from the mass to how the material is supported. For an optical cavity the way the spacer bends under gravity is directly important to the stability of the cavity. Known as the acceleration sensitivity, when the cavity curves under gravity it causes

the geometry of the cavity to be altered. However, by supporting the cavity at optimal points the overall fractional length change can be minimised, decreasing the acceleration sensitivity.

3.2.1 Airy and Bessel points

Two significant locations of support points, are the Airy and Bessel points. For a uniform bar, the Airy support points are located $0.2113L$ [42] from the end of the bar, where L is the overall length. As seen in Figure 15a, the Airy support points provides minimal bending in the end surfaces, making them nearly parallel.
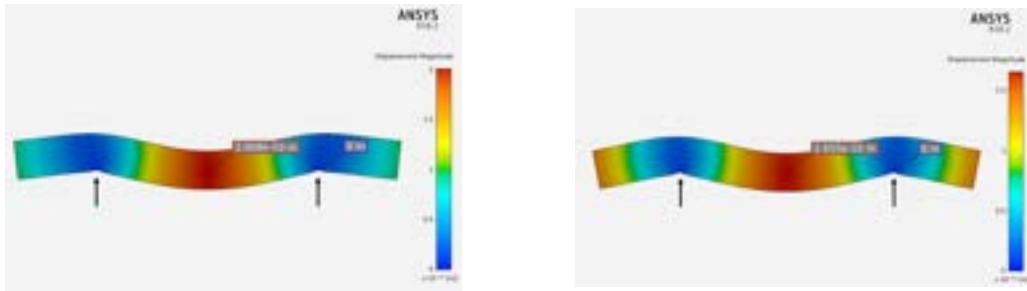
(a) Supported at the Airy points where $z \approx 0.2113L$ (b) Supported at the Bessel points where $z \approx 0.2203L$

Figure 15: Displacement contour diagrams displaying the effect of vertical acceleration on $3 \times 5 \times 30$mm uniform steel bars under 1g of acceleration, with the scale on the right-hand side of each figure. z is the distance each support is from the end of the bar, where the support locations are denoted by the black arrows, with L as the total length.

Whereas, the Bessel support points are situated at $0.2203L$ [42][39] from the end of the bar and result in the bar displaying minimal fractional length change, $\Delta L/L$ in the horizontal direction. The angle at which the end surfaces bend under 1g and the fractional length change for both when the bar is supported at the Airy and Bessel points are shown in Table 2. As seen when supported at the Airy points, θ is reduced and likewise when the bar is supported at the Bessel points the $\Delta L/L$ is reduced.

43

Table 2: The total angle that the end faces of a $3 \times 5 \times 30$mm uniform steel bar bend vertically downwards, θ and the fractional length change, $\Delta L/L$ of the bars, when the steel bars experience 1g of vertical acceleration, when supported at the Airy and Bessel points.

	Airy	Bessel
$\theta(°)$	8.25×10^{-10}	1.23×10^{-9}
$\Delta L/L$	3.44×10^{-10}/g	5.59×10^{-12}/g

For the same uniform steel bar, the relationship between the fractional length change and the position of the supports from the end of the bar, x can be seen in Figure 16. The bar is 30mm long, so it would be expected that the graph would exhibit minimal change in length when $x = 30 \times 0.2203 \approx 6.61$mm. As the graph crosses zero at exactly 6.61mm, it completely agrees with the theory.
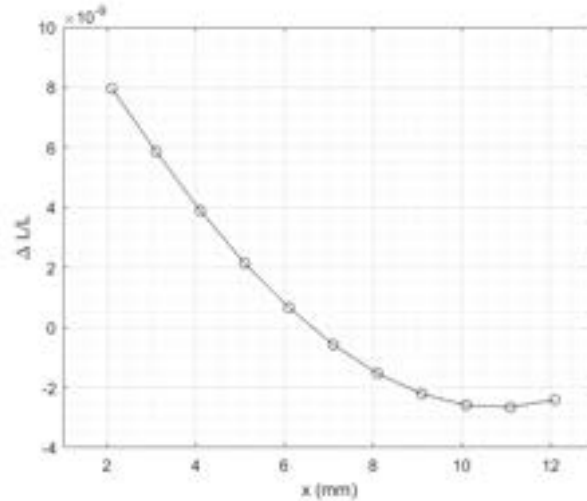
Figure 16: Locating the bessel points of a $3 \times 5 \times 30$mm uniform steel bar, with fractional length change, $\Delta L/L$ versus the symmetrical distance the supports are from the end of the bar, x. The bessel points are found to be at $x = 30 \times 0.2203 \approx 6.61$mm, where the data crosses zero. The points are connected to guide the eye, with the error bars not visible on this scale. Data from simulations computed on ANSYS.

In terms of improving the acceleration sensitivity in optical cavities, the Bessel support points or equivalent (if more than two supports are used or if vertical mounted) need to be found in order to reduce the effect of gravity on the fractional length change. These points can be found for an optical cavity by using finite element analysis and in a similar method to the one described above

in this subsection. However, the angle that the end surfaces may bend under gravity is still notable, as if the surfaces perpendicular to the optical axis bend too much this can cause too much misalignment of the laser light.

3.3 Vibrational Sensitivity

Both seismic and acoustic noises can cause vibrations in optical cavities, causing fluctuations in the cavity length, know as the vibration sensitivity. In general seismic noises, which will affect lab based optical cavities, are produced by human activities including, industrial work and traffic, but will also include noise from natural sources, for example on a windy day this can cause vibrations through a building. Acoustic noise tends to be more local, and can be caused from air moving through ventilators to music being played. To reduce the effect of acoustic noise the cavity can be placed under vacuum or by placing it in a carefully designed enclosure.

To minimise any passive isolations, created by seismic or acoustic noise, from being transferred from the floor to an optical cavity, the cavity can be placed on an optical table with pneumatic legs. Alternatively or additionally an active vibration isolation platform can be implemented to isolate the cavity from the table. For short cavities (approximately less than 10 cm), another way to reduce the vibrational sensitivity is to mount them vertically, so in theory both mirrors will experience the same amount of vibrations, which will cancel out the vibrational effects on the length of the cavity.

3.4 Pressure Sensitivity

With the presence of gas within the bore of a cavity, the optical path length is altered when the air in the bore experiences a change in the pressure, p, such that the change in the optical path is:

$$\frac{\Delta l}{l} = \frac{dn}{dp}\Delta p \tag{46}$$

where n is the refractive index of the air within the bore and in turn $dn/dp \approx 3 \times 10^{-11}\text{Torr}^{-1}$ [45]. To minimise this effect, a cavity can be placed in a vacuum, where the spacer has a small hole through it to the bore to allow the gas within the bore to be removed as shown in [4]. If the vacuum is sealed then there will be no pressure fluctuations, assuming that there are no leaks and zero out-gassing in the vacuum system, leading to a constant refractive index in the cavity bore. If no hole in a spacer is present and both mirrors are optical contacted to the spacer then this too would result in the bore being sealed, leading to the number of atoms within the bore being constant. Therefore, there would be no net change in the refractive index (small local changes in the refractive index will still occur as the gas moves around the bore), but this is only really

possible for fixed length cavities, as cavities with an adjustable length the mirrors are not normally directly contacted directly the spacer, resulting in the bore not being sealed (unless ring piezo-chips or similar are utilised). Also having a large number of atoms within the bore causes more scattering of the electromagnetic laser light within the bore, which will decrease the finesse of an optical cavity.

3.5 Thermal Noise (Brownian motion)

The stability of an optical cavity can never be lowered to an arbitrary level, due to the presence of Brownian motion in the mirror substrates and coatings [46]. Therefore, for cavity's with extremely low sensitivities this can be the limitation on their stability, resulting in these cavity's needing to keep the thermal noise as low as possible. However, this fundamental limit can be minimised through a couple of methods. Firstly, any circumstance which alters the movement of particles, for example by decreasing the number of particles, decreasing the temperature or having large particles, will overall decrease the rate of motion of the particles, which in turn will reduce the rate of the Brownian motion. For an optical cavity the only factor which can be changed in the mirror substrate is temperature. By cooling the cavity down to cryogenic temperatures, this causes less motion in the atoms, resulting in less Brownian motion affecting the length of the cavity. This method is ideal for cavities made from sapphire and other materials which have a zero crossing in their CTE at low temperatures but are impractical for cavities for which this is not the case. However there are other methods to reduce the thermal noise caused by Brownian motion, for example by increasing the length of the cavity as this would reduce the overall effects of Brownian motion in the cavity, also by utilising Fused Silica for the mirror substrate, as Fused Silica itself displays a low Brownian motion.
Another method to reduce the Brownian noise is by using larger spot sizes or coupling to higher order TEM modes. This will minimise the contribution of the individual atoms, as the motion on the whole will be more averaged out. This technique is a practical way to reduce the thermal noise for enhancement cavities where large spot sizes are required and desired. Of course for certain experiments, for example where fiber tip cavities are used, large spot sizes or high order TEM modes are not desirable, this approach would not be practical.

3.6 Optical Mirrors

Mirrors are key elements within an optical cavity with one of their most important factors being their shape, as optical mirrors can either be flat, concave or convex. The shape of each mirror with have a huge impact on the configuration of the cavity and in turn its stability. For example,

if both mirrors are flat then the cavity has a plane-parallel configuration and is quite unstable as any small changes in the length of the cavity will cause misalignment of the cavity. Therefore, it is vital to consider and select the correct mirror shapes for the configuration which is required for the application of the optical cavity (a full discussion on mirror shapes and cavity configurations can be found in Chapter 2.5).

Another crucial element of optical mirrors is their reflection coefficient of the coating. Each optical mirror coating will have reflectivity as a percentage, which will either be for a certain range of wavelengths or for a specific wavelength of light. For mirrors used within an optical cavity the reflectivity is commonly >99.97%, to allow the cavity finesse to be larger than $\approx$ 10k, where the higher the reflectivity, will directly increase the finesse of the cavity. The reflectance of the optical mirrors will however, depend on the size of the finesse which is needed for each individual cavity. Here is a discussion on the commonly used dielectric mirror coatings and a new type of single-crystal mirror coating.

3.6.1   Dielectric Mirrors

Dielectric mirrors are widely used mirrors for optical components, as their unique design allows the mirrors to have especially high reflection coefficients. Dielectric mirrors are composed of the mirror substrate (usually Fused Silica or for where a very low coefficient of thermal expansion is required, Zerodur can be utilised) and the mirror coating.

The mirror coatings are made up of dielectric layers with alternating refractive indices, where n_1 is smaller than n_2. Where a normal angle of incidence is required each layer has a thickness equal to a quarter of the wavelength of light in that layer, as illustrated in Figure 17. By stacking the layers using this method it allows for constructive interference between reflective light from each layer, resulting in the transmitted light being close to zero for each dielectric mirror, where a detailed description of how the constructive interference builds up being found in [16].
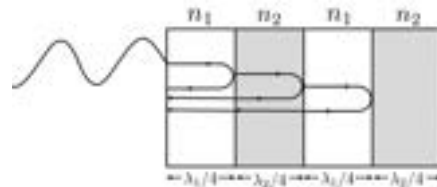
Figure 17: Illustration of dielectric mirror coatings and how their alternating refractive index layers are stacked.

While these types of mirror coatings can have exceptionally high reflectivities they do also have

quite a notable Brownian noise, which in certain ultra-stable optical cavities where all other instabilities have been minimised, this Brownian motion can be the limiting stability factor at an arbitrary level. Therefore, a new type of single-crystal mirror coating might be considered instead as spoken about below.

3.6.2 Single-Crystal Supermirrors

Another option to dielectric coatings is a reasonably new concept of *"supermirrors"* where monocrystalline semiconductor materials like GaAs/AlGaAs are employed to create crystalline mirror coatings [47]. These mirror coatings have exceptionally high reflectivity and display very low Brownian noise, making them convenient options for optical cavities where the Brownian noise is the key contributor to the instability, for example where small spot sizes are necessary, where the length of the cavity is small or simply where all other instabilities have been minimised and the cavity is limited by the Brownian motion at an arbitrary level.

These mirror coatings tend to be optically contacted to the mirror substrate and can exhibit finesses of over 300,000. However, they are currently limited in the range of wavelengths which in they can display these high finesse's as discussed in [49]. They are applicable for ultra-stable lasers for atomic clocks, high precision interferometry and for a range of high-finesse laser cavities.

3.7 Laboratory Considerations

There are certain laboratory considerations that can further reduce any fluctuations in an optical cavity's length, with one of the main considerations being temperature control within the laboratory. Especially if an optical cavity is not placed under vacuum, having the laboratory at a set temperature with minimal temperature fluctuations, can have a huge impact on keeping the thermal expansion sensitivity kept to a minimum.

Another laboratory consideration is to use an optical table or a vibration isolation table to reduce the effect that external acceleration vibrations can have on the length of an optical cavity. Here in this sub-chapter is a brief exploration of the magnitude of vertical and horizontal vibrations that are present on the floor in the laboratory, an optical table, a vibration isolation table and on a rotational table (that was designed to test the portably of optical cavities mentioned in this thesis). All measurements in this sub-chapter were taken using a seismic accelerometer (Wilcoxon model 731A), with a 100Hz measurement bandwidth, 10 V/g sensitivity and $\pm$ 10% sensitivity tolerance. The accelerometer has a 90 degree corner to enable it to be secured in either the vertical or horizontal direction. As a result, the accelerometer is able to measure vibrations in both the vertical or horizontal direction, depending on the direction it is initially set up in. In

Figure 18 is the initial vibrational measurements that were taken in the middle of the floor in the laboratory (where the laboratory is on the first floor in the building). As seen the vibrations are quite low both vertically and horizontally, which is expected as the floor is a stable environment.
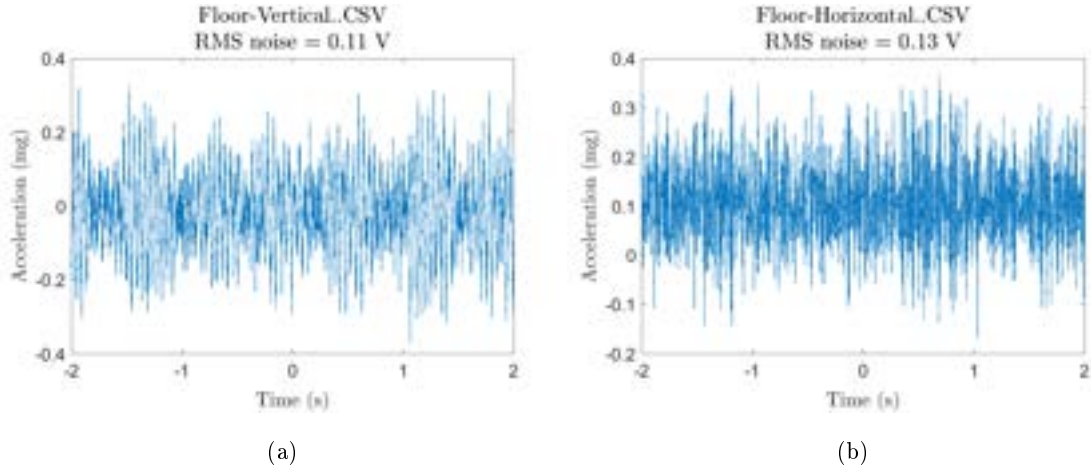
Figure 18: Background acceleration vibrations, measured with an seismic accelerometer (Wilcoxon model 731A), in the middle of the laboratory floor where (a) is vertical vibrations and (b) is horizontal vibrations.

Due to safety concerns it is not desirable to have any electronic equipment on the floor, resulting in experiments usually being elevated and on tables, where tables are commonly approximately 0.75m tall. This height off the floor increases the magnitude of vibrations as the tables are elevated off the floor by four legs making them more prone to external vibrations caused by movement within and from outside the laboratory. Figure 19 displays the background vertical and horizontal vibrations, that were measured on the optical table in the laboratory. As seen the vibrations in both direction are approximately four times the magnitude of the vibrations which were measured on the floor.
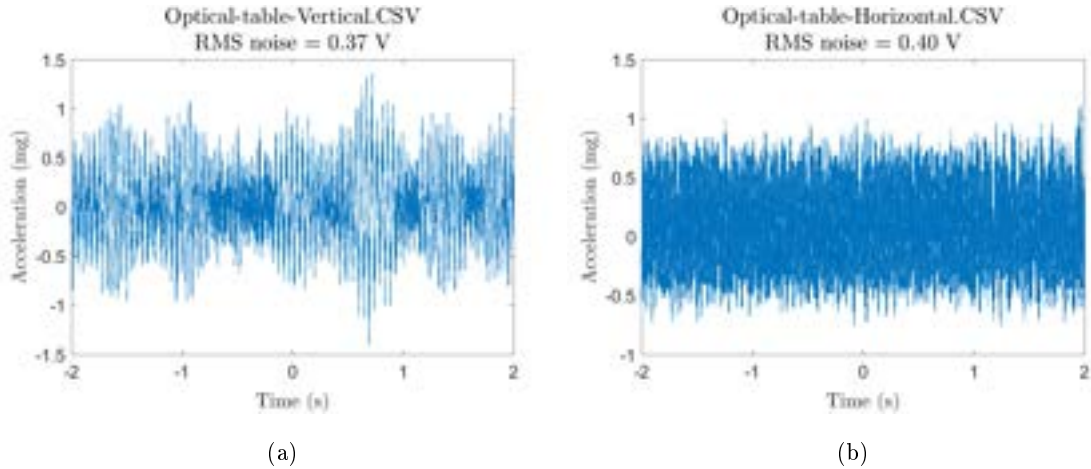
Figure 19: Background acceleration vibrations, measured with a seismic accelerometer (Wilcoxon model 731A), on the optical table where (a) is vertical vibrations and (b) is horizontal vibrations.

As optical tables do not offer sufficient shielding from external vibrations that ultra-stable optical cavities may require, it can be desirable to utilise an vibrational isolation table to offer more protection to an optical cavity, as discussed below.

3.7.1   Minus K

Minus K build vibration isolation platforms that are instead of being active isolating tables that utilise actuators and sensors to electronically reduce vibrations that a table experiences, uses a stiff string and a negative stiffness mechanism to produce passive isolating tables [48]. The background vibrations were measured on the set-up Minus-K platform (model 50BM-8, with a isolation bandwidth of 0.5Hz and 1.5Hz in the vertical and horizontally direction respectively), while the optical system for the invar lattice cavity (as discussed in Chapter 6) was on the platform. It was found that the Minus-K platform isolated the optical system significantly. As seen in Figure 20, the vertical vibrations have a root mean squared of approximately 0.07V (7 $\times 10^{-5}$g) which is approximately five times lower than the vibrations measured on the optical table. However, the background horizontally vibrations were found to be reduced further, as a root mean squared of approximately 0.05V (5 $\times 10^{-5}$g) was found which is approximately eight times lower than the optical table. Making the Minus-K platform an ideal option to reduce the amount of external vibrations an optical cavity experiences.
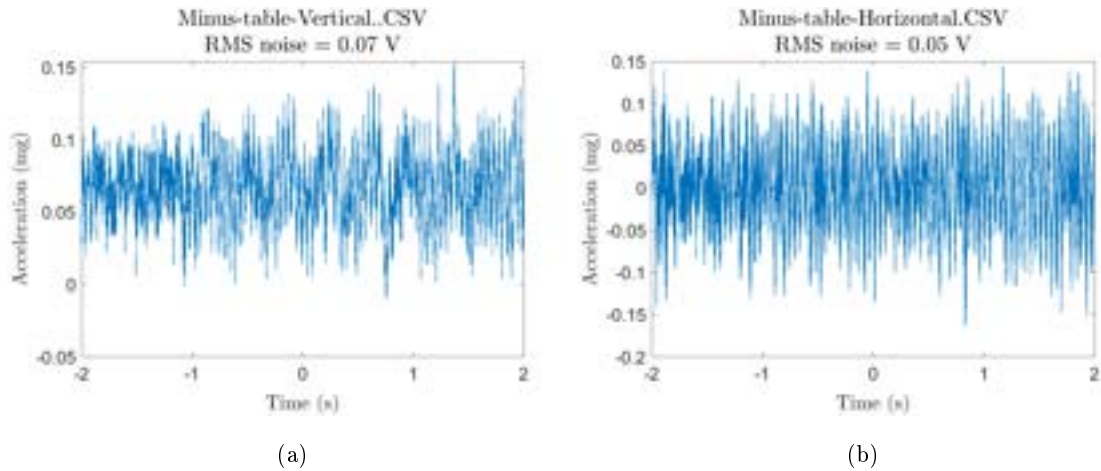
Figure 20: Background acceleration vibrations, measured with a seismic accelerometer (Wilcoxon model 731A), on the Minus K vibrational isolation platform (model 50BM-8) where (a) is vertical vibrations and (b) is horizontal vibrations.

3.7.2 Rotational table

To test the stability and portability of the cavities mentioned in Chapters 5, 7 and 8, a rotational table was designed and built. The table is designed to have an 300mm × 300mm × 12.7mm aluminium optical breadboard attached, with the CAD design of the assembly of the table being shown in Figure 21a. The table has four components, including the two legs, the main pole and the lock pin to hold the table in place at different angles. Both legs and the main pole are aluminium and were anodised to stop the aluminium from bonding, while the lock pin is brass, as a stronger material was required to ensure the pin did not bend under the weight of the optical breadboard. The table is designed, such that the optical breadboard can be rotated in total 180° and can be held in place every 15° by screwing the lock pin into each holding hole. The rotational table is secured onto a main optical table through the holes in the base of each leg, as shown in Figure 21b.

(b)

(a)
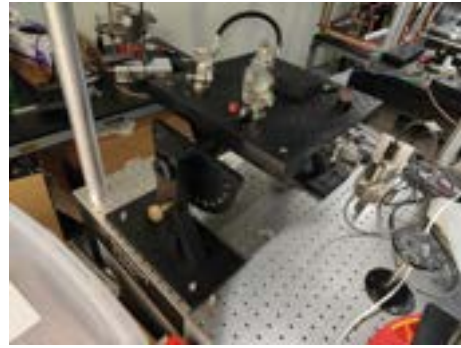
Figure 21: The rotational table designed to test the performance of optical cavity's when they experience acceleration in different directions, with (a) CAD design of rotational table and (b) an image of the rotational table built and attached to the optical table.

Similar to the optical table, background vibrational measurements were taken on top of the rotational table, while it was secured to an optical table and such that the attached optical breadboard was horizontally flat. Figure 22 shows that vibrations measured both vertically and horizontally are quite notable, with a root mean squared of approximately 0.6V (6×10^{-4}g) which is about 50% more than what was measured on the optical table. This is expected as the rotational table does add more height on to the optical table and also has no vibrational isolation design considerations.
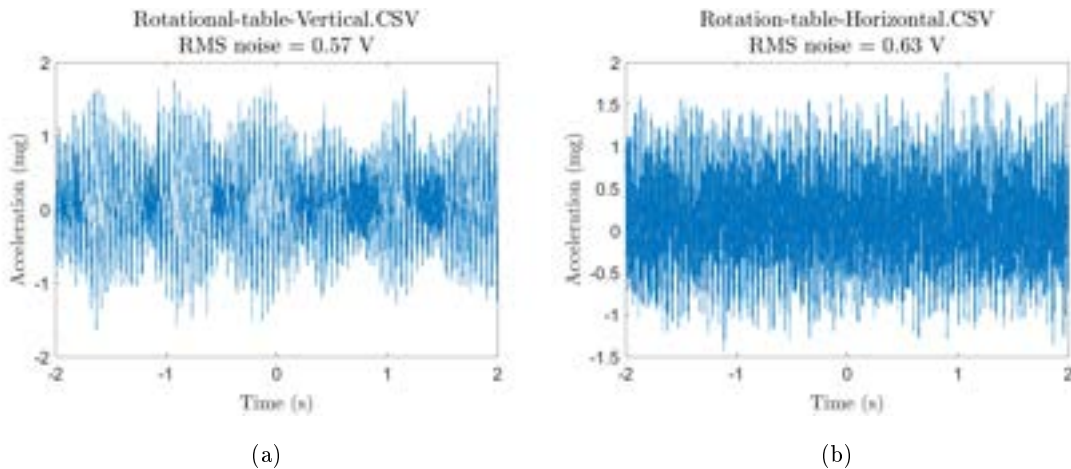
(a)   (b)

Figure 22: Background acceleration vibrations, measured with an seismic accelerometer (Wilcoxon model 731A), on the rotational table where (a) is vertical vibrations and (b) is horizontal vibrations.

In summary, while the floor in the laboratory displayed low acceleration vibrations it is not always safe and practical to work with electronics and optical systems on the floor, which is the case for the laboratory used for the work mentioned in this thesis. Therefore, an optical table is employed but unfortunately the acceleration vibrations measured on the optical table are about four times the magnitude that was measured on the floor, resulting in Minus-K platform being a preferable option for when the minimal acceleration vibrations are required, as the Minus-K platform exhibited similar or smaller accelerations vibrations, when compared to the results found from the floor. Lastly the acceleration vibrations measured on the rotational table, (which was designed to test the portably of optical cavities) are larger than the optical table which is expected. The rotational table displayed larger acceleration vibrations, but they where still reasonably low enough to keep the vibrational sensitivity within an optical cavity kept at a satisfactory level.

4 Assembling a Tunable 2.6μm Cavity

Since the first laser was built back in 1960 [43], slightly different methods have arisen in laser cooling and trapping atoms. By utilizing the fact that when an atom absorbs and re-emits a photon, its momentum its altered, atoms can be slowed down and cooled to almost absolute zero. A common method in trapping atoms is to use a magneto-optical trap which involves using laser cooling with a magnetic field to trap and cool neutral atoms.

Here we look into cooling and trapping of strontium-88 (^{88}Sr) atoms for the use in long range dipolar interactions and precision metrology, with all energy levels explored being displayed in the simplied electronic level structure of ^{88}Sr in Figure 23. In the work mentioned in [13] a 461nm and 689nm laser are used for the first and second stage of cooling the atoms for $^1S_0 \rightarrow {}^1P_1$ and $^1S_0 \rightarrow {}^3P_1$.
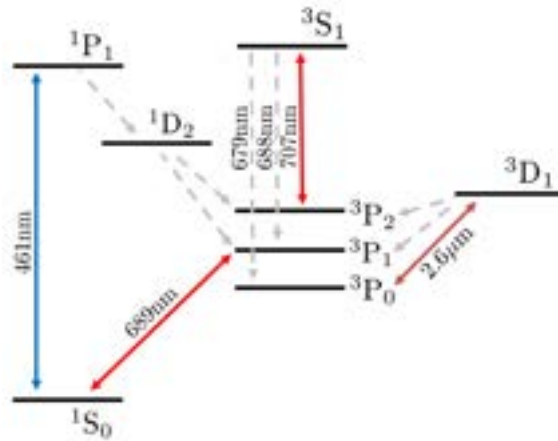
Figure 23: Simplified electronic level structure of Strontium-88 (^{88}Sr), displaying the first and second cooling stages and the re-pumping stages.

A novel re-pumping scheme is then introduced, which utilizes a double re-pumping of $^3P_2 \rightarrow {}^3S_1$ at 707nm and $^3P_0 \rightarrow {}^3D_1$ at 2.6μm. This is instead of $^3P_0 \rightarrow {}^3S_1$ at 679nm and $^3P_2 \rightarrow {}^3S_1$ at 707nm, which are most commonly used as re-pumpers in strontium MOTs. The introduction of this novel re-pump scheme is utilised as it enables the study and production of hard-core lattice bosons with long-range hoping. In their oven at 560°C, a loading number of one billion atoms is continuously re-pumped in the MOT with the double re-pumpers and with an added Zeeman slower. Both re-pumpers used are home built, with the 707nm laser locked to a wavemeter and the 2.6μm laser free running. They had successfully manage to measure the Landé g factor of $^3D_1$ to be 0.4995, which is relativity similar to the theoretical value of 0.4988. The experimental value

for the Landé g factor is to be further improved by locking the 2.6μm laser to a tunable cavity, where the linewidth is $\approx$ 100kHz and a stability of $\approx$ 20kHz is required. In this chapter is a detailed exploration of the assembly of the cavity to lock the 2.6μm laser and a discussion of the vacuum chamber.

4.1 Design of 2.6μm Cavity

The 2.6μm cavity is designed to be a small tunable hemispherical cavity, to allow the cavity to be locked to the frequency of the atom transition, after the frequency of the laser is locked to the length of the cavity. The cavity is also design to be placed under a vacuum pressure of 10^{-7}mbar. The cavity incorporates a ULE spacer and two ULE rings with two fused silica (FS) mirrors, with one mirror being planar and the other being concave to create the hemisphere cavity shape. ULE was selected due to the material's low coefficient of thermal expansion (CTE) and FS was used due to its good transmission at 2.6μm wavelengths, whereas ULE was unsuitable to be used for the mirrors as it has very poor transmission around this wavelength. In total twelve piezo-chips will be used with six on each side of the cavity, with three placed between the ULE spacer and ULE ring and three placed between the ULE ring and FS mirror, as shown in Figure 24. This cavity design was first created by NPL and it is worth noting the tunable cavity design here is built off their original design.
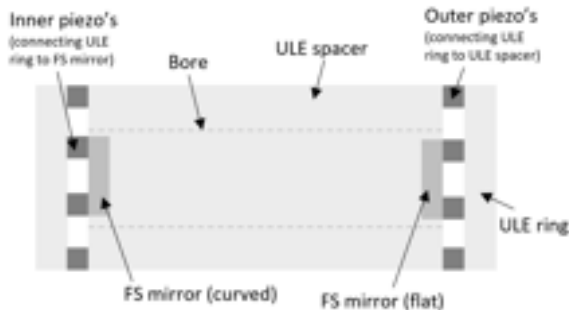
Figure 24: Design of the hemispherical tunable 2.6μm cavity, with a ULE spacer, FS mirrors, two ULE rings and twelve cubed piezo-chips.

The spacer has a length of 30mm, diameter of 25mm and a large bore with diameter 15mm. Both ULE rings are 25mm in diameter, 2.5mm long and have a bore diameter of 6mm. Each mirror is 6.35mm in length and 12.7mm in diameter with coated centres of 7.7mm in diameter. Both mirrors have a reflectivity of 99.98% for 2.6μm light at 0°. All piezo-chips are 3mm cubes, which display a displacement of 3.5μm $\pm$15% when a drive voltage of 150V is applied across the bare

electrodes (within operating temperatures of -25 to 130°C). On one side of the cavity, the piezo-chips connecting the ULE ring to the spacer will be wired, allowing the length of the chips to be altered and in turn to allow the length of the cavity to be varied to enable the cavity to lock to the wavelength of the laser light.

4.2 Constructing the 2.6μm Cavity

The entire assembly, cleaning of the components and later on placing the cavity in the vacuum chamber, was done in a clean laminar airflow cupboard to ensure everything was kept as clean as possible until the vacuum chamber was sealed.

The first stage in building the cavity was to attach three piezo-chips to the backs of both mirrors. To ensure the piezo-chips were evenly placed, small components were 3D printed to help align the chips (full details can be found in Appendix A). The mirrors with the attached piezo-chips are displayed in Figure 25, were the chips where attached with a two part, vacuum epoxy (Loctite®Hysol®1C, also known as Torr Seal). Each chip was attached such that the positive electrode (silver face of each cube with the plus sign closest) was facing the same direction.

(a)   (b)

Figure 25: Both FS mirror's for the 2.6μm cavity with three piezo-chips evenly attached to the back of the mirrors, with (a) being plane-planar and (b) plane-concave with a radius of curvature of 500mm.

The next stage was to wire three piezo-chips to the vacuum wire (a KAPW1X025 - KAPTON® WIRE 0.25mm (30 AWG) 2kVDC 2A L=10m, LewVac vacuum wire with nine wires and corresponding pins). First the soldering equipment was cleaning, including the tip of the soldering iron, where a thin soldering tip was selected. The piezo-chips were then attached using a vacuum compatible leaded solder, to the wires with three wires going to the positive electrodes and three to the negative electrodes (with the remaining pins left available for the temperature controls). As seen in Figure 26, the positive electrodes were attached to the upper three pins and the

negative to the bottom three. Once all wires were securely attached, both the vacuum wire with the piezo-chips attached was cleaned in an ultra-sonic machine for approximately 30 minutes.
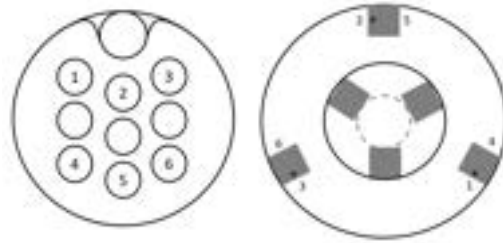
Figure 26: Schematic of how each piezo-chip is wired to the vacuum wire used for the vacuum electrical feed though, with the vacuum wire pins on the left and a diagram of how the piezo-chips are placed in the 2.6μm cavity on the right, where the grey cubes represent the piezo-chips and each positive electrode is represented by a small "+".

Following this the three wired piezo-chips were to be attached to first the ULE ring while the last three un-wired piezo-chips were attached to the other ULE ring. The chips were attached using a similar 3D printed component to evenly place the chips out on each ULE ring and the same vacuum epoxy as mentioned earlier was used, with both ULE rings shown in Figure 27.

(a)   (b)

Figure 27: Both ULE ring's for the 2.6μm cavity with (a) three piezo-chips attached and (b) three wired piezo-chips attached.

The next stage was then to attach both mirrors to the ULE rings using the same epoxy. As shown in Figure 28, each mirror was placed such that the piezo-chips alternate between the mirrors and rings. This was to try and even out any tilt in the mirrors that could be caused by uneven layers of epoxy under each chip.

<center>(a)</center>
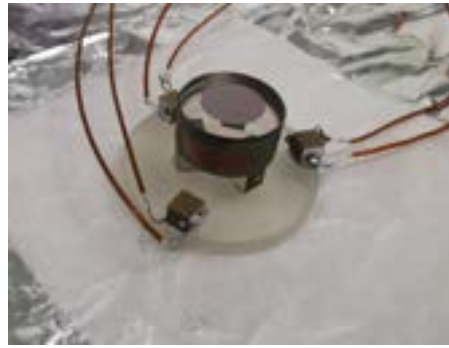
<center>(b)</center>

Figure 28: Both ULE ring's with each mirror attached (a) with non-wired piezo-chips and (b) with wired piezo-chips.

The last stage in assembling the 2.6μm cavity was to attach the ULE rings plus mirrors to the ULE spacer. The spacer was first cleaned and then to ensure both ULE rings were attached parallel to the spacer small ring 3D printed components were used, with the fully assembled cavity displayed in Figure 29.

<center>Figure 29: Fully assembled 2.6μm, ULE-FS tunable cavity.</center>

In Figure 29, it is shown that both of the FS mirrors sit within the bore of the cavity's spacer, due to both mirrors have diameters which are smaller than the diameter of the cavity's bore. This is the key reason why twelve piezo-chips was used for the 2.6μm cavity, as neither mirror could be directly contacted to the spacer and instead had to be connected to the ULE rings, which then could be contacted to the cavity's spacer. Another advantage of using six piezo-chips on each end of the 2.6μm cavity is that it cancels out the impact of the coefficient of thermal expansion of the piezo-chips.

<center>58</center>

This 2.6μm cavity should theoretically display a finesse of 1.57×10^4, due to both mirrors having equal reflectance of 99.98%. The cavity initially will have a length of approximately 41mm with an initial free spectral range of 3.66×10^9Hz and linewidth of 2.3×10^5 but to due the cavity being tunable in length by $\approx 3.5\mu$m, this results in both the free spectral range and the linewidth of the cavity also being tunable. It is also worth noting that the length of the cavity will have been slightly affected by the use of a vacuum epoxy to attach each component of the cavity together.

4.2.1 Vacuum Chamber

The vacuum chamber is made with aluminium and titanium, with the outer section being titanium and the inner parts being aluminium. The chamber is based on a past vacuum chamber used within the team at The University of Birmingham, as described in [44]. It has three sections to house the cavity: the inner, middle and outer sections, with the CAD designs for the chamber being shown in Appendix A. Initially without the cavity, the vacuum chamber was tested using a turbomolecular pump to check for any leaks. After a few attempts, it was found that the wrong sized screws were being implemented in the outer chamber, causing a notable amount of leaks. While waiting for new screws to arrive and once the cavity was fully assembled it was placed into the vacuum chamber, by firstly positioned the cavity within the inner vacuum chamber as shown in Figure 30a. Six, 5/32" Viton balls were used to suspend the cavity within the chamber and hold it in place. After this the inner section of the vacuum chamber was placed in the middle section as displayed in Figure 30b. Similarly as before, six Viton balls were used to suspend the inner chamber. By suspending the cavity and the inner chamber section with Viton balls, this will reduce the vibrational sensitivity in the cavity and will hold it in place to make the whole system more portable.
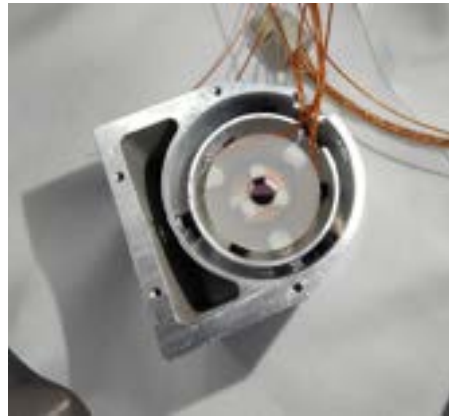
<div align="center">(a)   (b)</div>

Figure 30: Assembled 2.6μm cavity placed in the (a) inner section of the vacuum chamber and (b) the inner section placed within the middle section of the vacuum chamber.

In the outer vacuum chamber section, a peltier element (Thorlabs TEC-6) was glued using a vacuum epoxy at the bottom in the middle, as shown in Figure 31a. The peltier element is connected to a temperature controller (Thorlabs T-Cube), to allow the temperature of the chamber to be altered. On top of the middle chamber a negative temperature coefficient thermistor (EPCOS / TDK B57861S103F40) is attached to allow for the temperature of the chamber to be monitored.
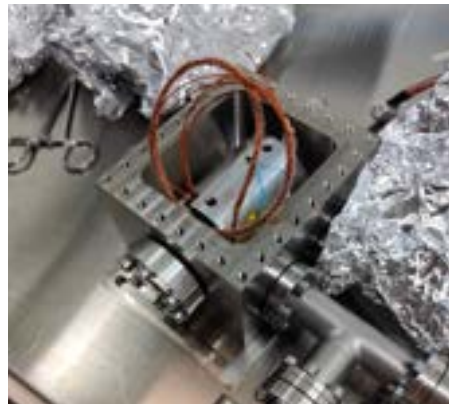
<div align="center">(a)   (b)</div>

Figure 31: Open outer vacuum chamber for the 2.6μm cavity with (a) the peltier element (Thorlabs TEC-6) attached at the bottom (b) the middle chamber placed within the outer chamber with a negative temperature coefficient thermistor (EPCOS / TDK B57861S103F40) attached to the top of the middle chamber.

The middle chamber was closed and then positioned into the outer chamber. The whole system was then checked to make sure cavity mirrors were aligned with the outer vacuum windows, before the chamber was closed and sealed.

4.3   The Next Steps

Once the built cavity was sealed into the vacuum chamber, the next stage was to align the system within the optical system. During this process it was found that even though the mirrors appeared to the naked eye to have a suitable alignment with the windows, to allow the laser light to pass through, in practice this seemed to not be the case. It is not clear whether the cavity was at a tilt or if something was obstructing the lights path, but when positioning the cavity within the optical system no transmitted light was detected.

One of the reasons could be that due to the system relying on the viton balls being in place and the spacer and inner section putting reasonably equal amounts of pressure on each ball, it is possible for either of these two requirements to not be in place, causing a tilt or misplacement in the cavity. Firstly, a viton ball could have been knocked out of its position during assembly of the vacuum system, or during transporting the system between laboratories. Secondly, as there are wires that connect to the cavity, this could cause the cavity to have added pressure from the wires, leading to uneven pressure on the viton balls. This can cause a tilt in the cavity and therefore in the optical axis, stopping the light from being able to pass through the system. Another reason for the light not being able to pass through could be that a wire within the system is blocking the light. This nevertheless is unlikely as the wires would be quite visibly in front of one of the windows. However if there were small scratches or dust particles blocking the optical path this could have been causing too much scatter of the light, resulting in no detectable amount of light being able to pass through.

Moving forward there are a few alterations that need to be made to the vacuum chamber to ensure the cavity is suitably aligned within the chamber. As for this experiment the cavity does not need to be mounted within a portable vacuum chamber design, unlike the work mentioned in [44], a simpler approach could be taken. One suggestion would be to have the cavity spacer sit solely on four viton balls, and have the inner and middle sections of the vacuum chamber replaced with a similar design as displayed in Figure 32. The four viton balls would sit in the four small holes that are symmetrically situated in the semi-circular design. This middle/inner section of the chamber would then directly sit within the outer vacuum chamber, eliminating the inner chamber, which would reduced the risk of misalignment during the assembling stages.
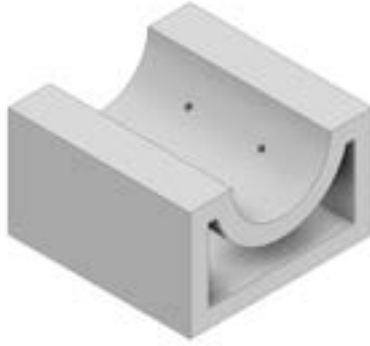
Figure 32: New proposed design to replace the middle/inner section of the 2.6μm cavity's, vacuum chamber

After changes are made to the vacuum chamber and the cavity is successfully placed into the optical system the next step would be to pump the chamber down to approximately 10^{-7}mbar, making the cavity ready for locking to the 2.6μm laser. In order to pump the chamber down to 10^{-7}mbar firstly a turbomolecular pump would be used to pump down the chamber's pressure to 10^{-2}mbar, where then an ion pump will be implemented to further reduce the pressure down to the desired 10^{-7}mbar. At this pressure the chamber will be evacuated of a sufficient amount of air and other particles to allow the cavity to display a stability of <20kHz which is required for the experimental need, discussed at the beginning of the chapter.

Additionally, it would be beneficial to test the cavity before placing it within the vacuum system to allow for the performance of the cavity to be observed, and to compare this with the performance while in the vacuum chamber. However, by initially testing the cavity this increases the time in which the cavity has to gain dust etc, within and on the cavity, which would in turn affect the stability of the cavity.

5 Invar Cavity

Commonly, materials notably expand and contract as the temperature fluctuates, causing a limit on any precise measurements. However, back in 1896, Charles-Edouard Guillaume discovered a nickel and steel alloy which displayed almost no change in length when the temperature was varied. The discovery of this nickle-steel alloy had a remarkable effect on scientific instruments and in turn played a major role in precise measurements. So much so, that in 1920 Charles-Edouard Guillaume was awarded the Nobel Prize in Physics, "in recognition of the service he has rendered to precision measurements in Physics by his discovery of anomalies in nickel steel alloys" [37].

The low-expansion nickel and steel/iron alloy has also been found to be useful in many other applications such as for: thermostatic strips, glass to metal seals, large aero-structure moulds and for moving parts in internal-combustion engines that need control of expansion, for examples in pistons [32]. In addition, invar can be used for structural components in laser and optical systems. As high dimensional stability is required for the material used for the spacer in an optical cavity this makes invar an appropriate material to be used, to reduce any instability caused by thermal expansion sensitivity within a cavity.

Initially the idea of incorporating invar for the material of the spacer in an optical cavity started within the University of Birmingham is a research group led by Prof. Moataz Attallah who specialise in advanced material processing, including additive manufacturing techniques. The group utilise selective laser melting to create complex geometries in a range of materials, including invar. There are other materials like ultra-low expansion glass (ULE) and NEXCERA that display a lower coefficient of thermal expansion than invar, but the ability to have invar be made into complex geometries allowed for some novel optical cavities to be designed and built. Here we present an optical cavity that can be directly attached to an optical table, by having the spacer and support printed as one solid component.

In this chapter we introduce the properties of invar and explore how its exceptionally low coefficient of thermal expansion makes it a good material to be used for the spacer of an optical cavity, as well as brief a focus on super-invar and how it can be used to further reduce the thermal expansion sensitivity in an optical cavity. This leads on to an introduction to selective laser melting and a short description to how each invar component was printed.

Next is a detailed investigation of the optimisation of the geometry of the invar cavity. With the use of finite element analysis and by altering the size of the cut-outs and the position of the supports, it was found that the fractional length change of the cavity, between the centre of the mirrors, changes from positive to negative at a zero crossing, at a number of different geometric

points. At these zero crossings is where the cavity will experience the smallest acceleration sensitivity, make these points where the geometry is at its optimal size. However, as printing and manufacturing errors will cause imperfections in a component, this needs to be taken further, by finding a zero crossing with the shallowest gradient, to allow the geometry to have tolerances that will not drastically increase the acceleration sensitivity of the cavity. Therefore, the point where the zero crossing has a shallow as possible gradient was investigated, as discussed later in the chapter.

At the end of the chapter is a description on how the mirrors were attached to the invar spacer and a discussion on testing the cavity, with a conclusion on the improvements that could be made to the spacer and the applications that the invar cavity could be utilised for.

5.1   Properties of Invar

Iron and nickel alloys display a range of coefficients of thermal expansion, depending on the amount of each metal present in the alloy. With respect to the percent of nickel present, the varying coefficient of thermal expansion can be seen in Figure 33.
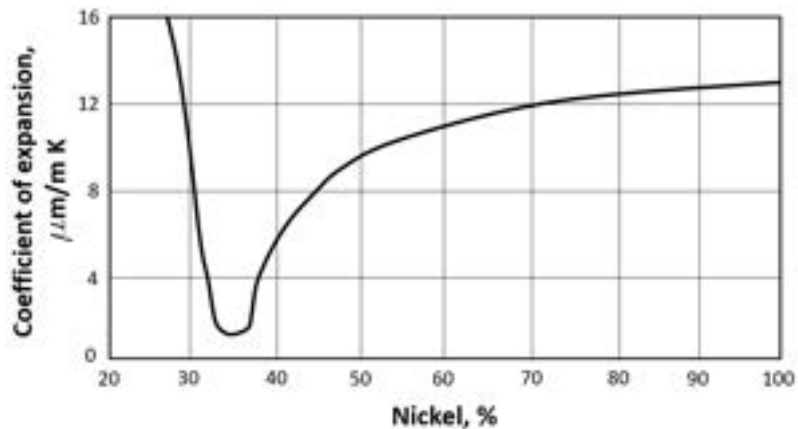
Figure 33: The coefficient of thermal expansion versus percent of nickel for Fe-Ni alloys, containing 0.4% Mn and 0.1% C at 20°C. Adapted from [32].

As shown when the amount of nickel is at ≈36% the coefficient of thermal expansion is at the lowest point. When the alloy contains 36% nickel and 64% iron the thermal expansion is known to be so low that the change in length of the alloy is nearly invariable at room temperatures, resulting in the alloy being named invar, for invariable [32]. Hence for invar or sometimes known as invar 36 (for the 36% of nickel) the coefficient of thermal expansion is $1.6 \times 10^{-6}/°C$ [33]. Which when compared to $12 - 16 \times 10^{-6}/°C$ for other steels [33] is considerably lower, making

invar a desired material for sensitive optical assemblies including being used as a spacer within an optical cavity as it will display minimal thermal sensitivity. Additionally, due to invar being a metal it is considerably more straightforward to manufacture in a general workshop into optical components than most glasses or ceramics that are commonly used.
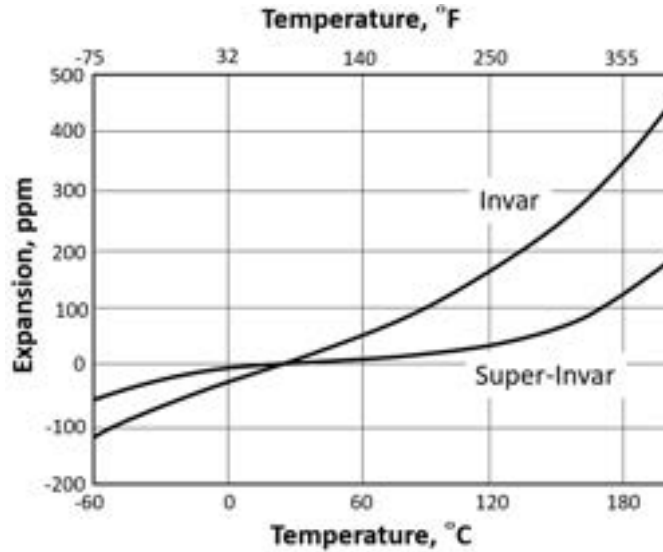
Figure 34: The thermal expansion of invar (64% Fe and 36% Ni) and Super-INVAR (63% Fe, 32% Ni and 5% Co). Adapted from [32].

The thermal expansion of invar does still alter with temperature as shown in Figure 34. This trend shows that the thermal expansion can range from negative to positive within $0 - 60°C$, meaning that a cavity spacer made from invar will still need to be within a reasonably stable temperature environment (for example fluctuations at room temperture will not make a difference but the large fluctuations the British weather exhibits outsite can cause a notable difference). It is also worth noting that invar is not normally composed of purely just iron and nickel, but does usually contain small amounts of other elements including, silicon, manganese and carbon (in total $> 1\%$)[32].

5.1.1 Super-invar

The invar alloy can be adapted by replacing a proportion of the nickel with cobalt, to create an alloy with an even lower coefficient of thermal expansion around room temperture, known as super-invar [32], to the extent that the super-invar alloy containing 63% iron, 32% nickel and 5% cobalt displays a thermal expansion around room temperature as low as $0.72 \times 10^{-6}/°C$ [33]. In addition the low coefficient of thermal expansion stays exceptionally low for a larger range of

temperatures, when compared to invar, as shown in Figure 34. As a result super-invar would be an interesting material to use for a spacer, in an optical cavity.

5.2 Selective Laser Melting (SLM) of Invar

Invar is found to be quite soft and adhesive, making it especially challenging to be machined. For this reason, more recently there have been other forms of manufacturing technologies which are being used to manufacture with the alloy. Selective laser melting (SLM) is currently one of the leading ways to manufacture with invar for when complex shapes are desired [34].

SLM is a type of 3D printing which utilises a laser and a metal powder, where the laser accurately melts and fuses the powder into a solid component. The process involves packing a chamber with the metal powder under a controlled atmosphere, layer by layer placed across a build plate. Then with the use of a high power laser, the powder is melted on a molecular level to create a reasonably uniform and dense part. Like other 3D printing methods, support structures are used for any overhanging features, but due to the weight of the material used, these support structures are utilized a lot more with SLM.

Some of the benefits of using SLM is that the process is handy for prototyping with the added bonus of minimal tooling needing to be completed after. However, there are a few downfalls, most importantly is the process causes the finished product to have a rough surface finish. For the use in optical cavities' spacers this rough surface area can cause an unwanted tilt in the mirrors, resulting in an unstable cavity. One way to reduce this is to use mirrors with large diameters, which in theory would even out any tilt caused by the uneven surface area to a certain degree. Other ways can include: using a lower lasering speed, polishing the ends of the spacer after construction or use mirrors which form a hemi-spherical cavity, which due the configuration of the light in the cavity is reasonably stable and less prone destabilisation caused by misaligned mirrors. Another disadvantage of SLM is that the technique is only really accessible for small parts, and is limited by the size of the machines. For the printing instruments used for these cavity spacers the size was limited to 90×90mm, with a maximum height of 150mm. However, with the use of slightly different printing equipment, the size limitation can be increased to 220×220mm with a maximum height of 250mm.

For SLM being used to manufacture optical cavity spacers, this allows for complex structures to be 3D printed, as a result, two unique spacer designs were produced using this method. The first being a horizontal cylinder with two cut-outs where the spacer is attached to the supports and the base of the cavity and will all be printed in one print. By having the spacer attached to the base this allows the cavity to be more portable and less prone to misalignment from external

66

vibrations. The second design (discussed in Chapter 6), involves an internal lattice in the spacer which will reduce the weight of the cavity, to reduce the acceleration sensitivity.

For both invar cavity spacers mentioned in this thesis they were made using SLM, with a laser power of 150W, laser scan speed of 800mm/s and laser hatch speed of 0.09mm. The invar used is Ni36% with some traces of (Cr, Mn, Si, C, Mg, Zr, Ti, P and S) and Fe the balance. Once the geometry was printed, they were polished using silicon balls. Next, they were both cleaned in an ultra-sonic bath to removed any left over dust on the surfaces before the mirrors where attached.

5.3 Shape of the Invar Cavity

The first step in designing the invar cavity was to select the general shape of the cavity. There were a few initial designs for the invar cavity which where explored, all of which are displayed in Figure 35. Each cavity design has a cylinder bore and are designed to be supported in four locations which are denoted by four small spheres within each subfigure.

From initial simulations it was found that for each of the designs, the acceleration sensitivity could be reduced and minimised by altering the positions of the four support locations, resulting in any of the designs being suitable to be used for the invar cavity. However, it was found more difficult for the simple cylinder design and the cuboid at a 45° angle design, as shown in Figure's 35a & 35d respectively, to find the exact locations of the four supports where the vibration sensitivity was minimised.

(a) A simple cylinder design.

(b) A cylinder design with two square cut-outs, to create a "mushroom" shape.

(c) A simple cuboid design.

(d) A cuboid at a 45° angle.

Figure 35: Four different horizontal optical cavity designs which were explored for potential designs for the invar cavity. For each design they are designed to be supported by four small symmetrical supports, represented by four small sphere in each figure.

Ultimately, the final shape for the invar cavity was selected to be the mushroom shape, as show in Figure 35b, as the added square cut-outs for the mushroom shape compensate for vertical forces, similarly as discussed in [7] and [35]. Which due to the most notable vibrations for horizontally mounted cavities in normal laboratory conditions are found to be in the vertical directions [36], this gives the mushroom design an added advantage over the other considered designed. Additionally, as the mushroom shape has these square cut-outs it has the added benefit of having extra dimensions to be explored in the optimisation of the cavity, as not only can the position of the supports be altered along the cavity, but the height and width of the cut-outs can also be varied.

68

5.4 Optimisation of Geometry

A simple "*mushroom*" cylinder design was created with dimensions shown in Figure 36, with the spacer and support made from invar and the mirrors made from Fused Silica (FS), with the material properties shown in Table 3. The mirror dimensions were set at $m_d = 12.7$mm and $m_L = 6.35$mm, but all dimensions for the spacer were to be determined.

Table 3: Material Properties of invar [38] and fused silica [41].

	INVAR	Fused Silica
Density	8050kgm^{-3}	2203kgm^{-3}
Young's Modulus	141GPa	73.6GPa
Poisson's Ratio	0.29	0.17

The first step taken in designing the spacer was to select the length, L of the spacer. Due to the amount of time it takes to fabricate invar using selective laser melting, a reasonably small length was selected of $60mm$. Taking into account both the mirror sizes and the length of the spacer, a realistic diameter of the bore, d and spacer diameter D was also selected at 6mm and 30mm respectively. This left the height of the cut-outs, y, the width of the cut-outs, x, the position of the supports, w & z and the size of the supports, S_d & S_h to be optimised. All four supports were placed such that they are parallel with each other, along the width and length of the cavity. Where if $z = 0$mm this would indicate that the supports were placed at the ends of the spacer and as z is increased the supports are moved closer to the middle of the cavity. Additionally, for all simulations the position of the support along the width of the cut-out w, was such that it is placed in the middle of the cut-out depth x.

(a) Angle view of cavity geometry.

(b) Front view of geometry.
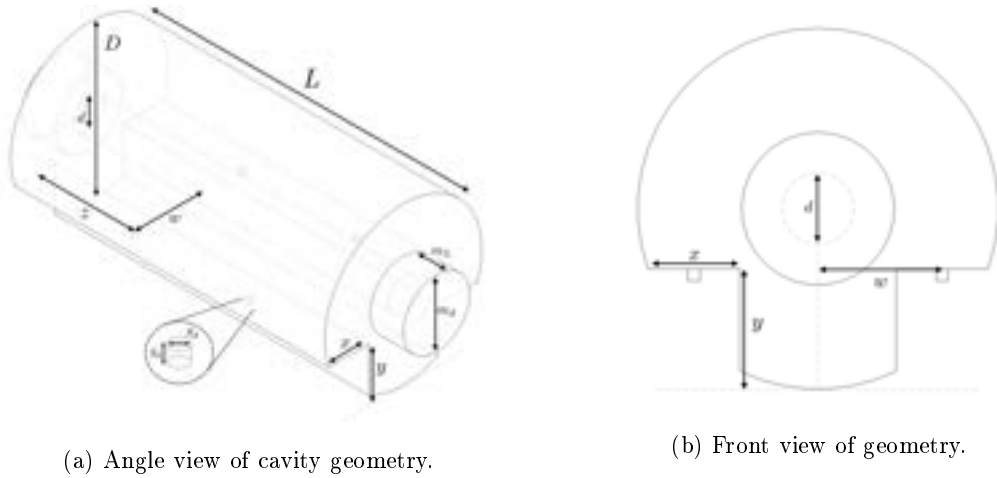
Figure 36: Diagram of the invar *"mushroom"* cavity design with geometric dimensions.

All simulations were completed without the base but including the four supports. It was assumed that supporting the geometry in ANSYS (software that uses finite element analysis for structural analysis) on the supports would produce the same axial displacement in the spacer, then if a base were included, with the benefit that as less geometry is used in the simulations, this would shorten the simulation times.

It was initially found that the larger the supports were in both diameter and height then the more the cavity is affected by the acceleration sensitivity. Therefore, the size of the supports needed to be kept to a minimum, resulting in the diameter of the supports, S_d being kept at 1mm and similarly the height of the supports, S_h being 1mm as at these diameters the supports will still be larger enough to with stand the weight of the cavity.

The next step was to optimise the size of the cut-outs by placing the cavity under 1g of vertical acceleration and finding the fractional length change between the centre of the two mirrors. First, the height of the cut-outs y, was varied along with the position of the support of the supports along the length of the spacer z, with the results shown in Figure 37a. The white squares represent when $-7.5 \times 10^{-11}/\text{g} > \Delta L/L > 7.5 \times 10^{-11}/\text{g}$ where the *"zero crossing"* occurs in the acceleration sensitivity (where the cavity has minimal axial displacement along the optical axis). From Figures 37a & 37b is it clear that for every value of z explored there is a minimal region in the acceleration sensitivity, whereas, there is only a small range in the y values where a *"zero crossing"* can be seen, resulting in the value for y needing to be carefully selected, in order for the cavity to display a minimised acceleration sensitivity.

(a) In the z, y space

(b) Versus height of cut-out y
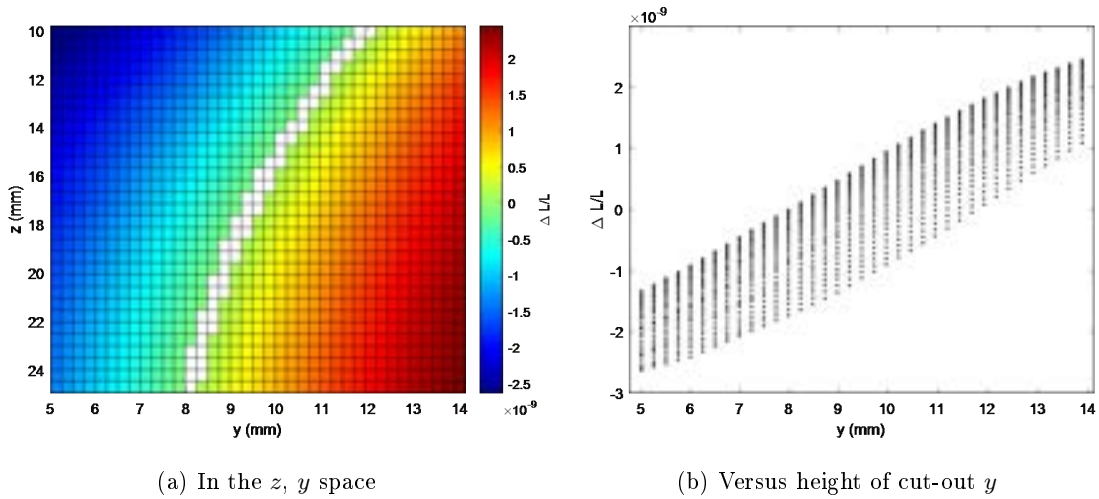
Figure 37: Invar cavity acceleration sensitivity (fractional length change $\Delta L/L$) under 1g of vertical acceleration, with relations to altering the size of the cut-outs, y(mm) and position of the supports, z(mm). Data from simulations computed on ANSYS.

Next, the depth of the cut-out, x was investigated. The zero crossing gradient of the acceleration sensitivity was explored for four different depths as show in Figure 38. As seen for the range of values tested that by decreasing x this in turn lowered the zero-crossing gradient. Additionally, for lower values of y, this further lowers the gradient, leading to the conclusion that smaller overall cut-out's in the cylinder spacer display lower zero crossing gradient and in turn minimal fractional length change in the optical axis, under 1g.
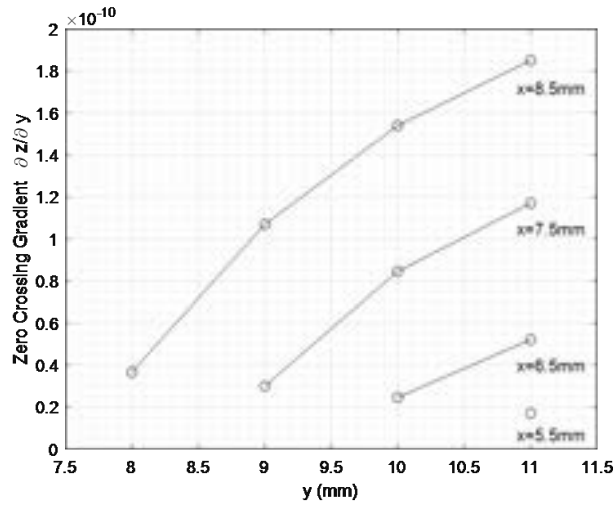
Figure 38: The zero crossing gradient of the acceleration sensitivity (fractional length change $\Delta L/L$) of the invar cavity under 1g of vertical acceleration, for different cut-out depths, y (mm). The points are connected to guide the eye, with the error bars not visible on this scale. Data from simulations computed on ANSYS.

5.4.1 Final Dimensions

The complete range of values tested and final values for the invar spacer and the FS mirrors are displayed in Table 4. After these where selected, the shape and dimensions for the base of the cavity were designed. In order to allow minimal bending in the base from the weight of the cavity, solid cuboids were added under each pair of supports, on either side of the cavity which led straight onto the solid base as shown in Figure 40a. The base has four M6 clearance holes and are separated by 50mm, to allow for the base to be directly attached to a metric optical table.

72

Table 4: Final dimensions for the invar cavity.

Parameter	Range Explored	Final Value
L	N/A	60mm
D	N/A	30mm
m_L	N/A	6.35mm
m_d	N/A	12.7mm
S_d	1-3mm	1mm
S_h	1-4mm	1mm
x	5.5-8.5mm	5.5mm
y	5-14mm	11mm
z	10-25mm	19.96mm

For the final invar design the final acceleration sensitivity was found to be 1.53×10^{-12}/g, with a gradient at the zero crossing of 1.7×10^{-12}/mm with the final finite-element analysis shown in Figure 39. As seen only the spacer, mirrors and small support were placed in the simulation, with the end faces of the four supports being constrained. Each angle displays that the spacer slightly deforms around each support, when placed under 1g of vertical acceleration.

(a)   (b)
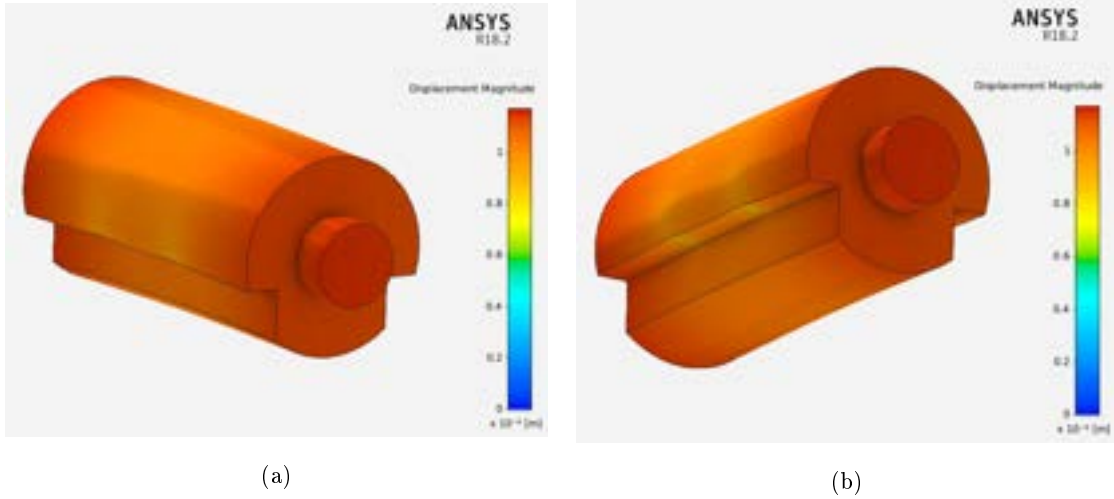
Figure 39: Displacement contour diagrams displaying the effect of vertical acceleration under 1g of acceleration for invar cavity with it's final dimensions. With (a) showing the contour from an above angle and (b) from a below angle displaying the displacement around the supports, with the scale on the right-hand side.

Figure 40 shows a comparison between the final CAD design and the printed and polished spacer. As seen the printed invar spacer and base displays a certain amount of surface roughness, which is to be expected due to the way it is fabricated. In case more polishing is needed on the end of the cavity, where the mirrors will be attached, only semi-permanent adhesive was used to attach the mirrors, while the initial tests are carried out on the cavity. However, the thermal expansion of the adhesive used could largely dominate the performance of the cavity.

(a)

(b)
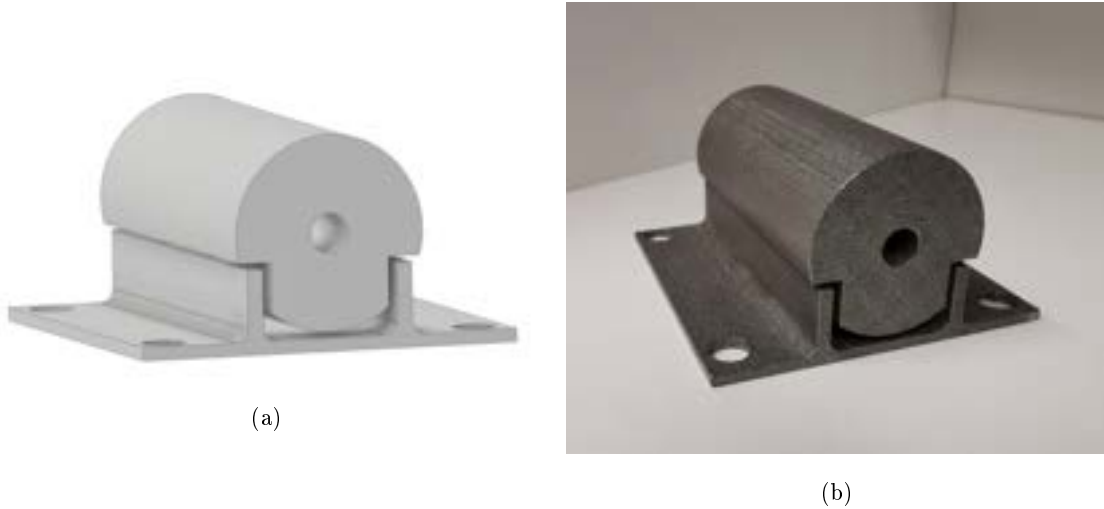
Figure 40: Final invar spacer and base geometry from the dimensions displayed in Table 4, with (a) the CAD design and (b) and image of the SLM invar spacer and attached supports and base.

5.5 Building invar Cavity

Building the invar cavity involved two steps: firstly cleaning the spacer and the mirrors, then secondly was attaching both FS mirrors. The invar spacer was cleaned first in an ultrasonic bath, then the mirrors were cleaned after, just before being attached to the spacer. Each FS mirror is 6.35mm in length and 12.7mm in diameter with a reflectivity of 99.97% ($\pm$0.02%) for 689nm light. For attaching the mirrors a temporary bonding adhesive was used, called Norland optical adhesive (NBA107). This allowed for the mirrors to be removed, in case further polishing was needed to be made to the spacer. The adhesive needs UV light for curing and is designed such that de-bonding is simple by only using hot water with some added detergent or using acetone.

Figure 41: Image of the fully constructed hemispherical invar cavity, ready for testing.

A small plastic 3D printed component was used to ensure the mirrors were attached in line and with the bore, in the middle. The first mirror has a plane-planar shape, while the second mirror is concave with a radius of curvature of 500mm ($\pm0.5\%$), resulting in the cavity having a hemispherical shape. These mirrors were used for the initial testing of the cavity as they were already available in the laboratory. For the final invar cavity where a permanent adhesive is to be used for attaching the mirrors, new mirrors with appropriate coating's for the wavelength of the type laser being used with the cavity, will be purchased and utilised.

For the these initial mirrors the stability of the cavity was calculated using the stability condition mentioned in Section 2.5. Where g_1 is the planar mirror and therefore equal to one and g_2 is the concave mirror, making it equal to 0.88. It is clear the cavity sits well within the stability condition:

$$0 \leq g_1 g_2 \leq 1 \tag{47}$$

as $g_1 g_2 = 0.88$. Due to the mirrors creating a hemispherical cavity, it results in the cavity being especially robust to misalignment, as one mirror is planar.

Given the mirrors have reflectances of 99.97% the cavity should display an approximate finesse of 1.05×10^4, but due to the error on the reflectance of each mirror this could range from 6280 to 3.14×10^4. The initial length of the cavity was to be 60mm, which would have resulted in a free spectral range of 2.500×10^9Hz and then a linewidth of 2.38×10^5Hz (assuming the reflectances are 99.97%). However the printed length of the cavity is $\approx 59.8 \pm 0.1$mm making the actual free spectral range of the cavity to be slightly larger at $\approx 2.51 \times 10^9$Hz.

5.6 Scanning the Invar Cavity

Once built the invar cavity was position into a simple optical system with the diagram of the system being displayed in Figure 42. Laser light, with a wavelength of 689nm entered the system from another bay within the laboratory, through a 20m long optical fiber. The incoming laser light was initially 30mW when it entered the long fiber but after passing through the fiber and the electro-optical modulator (EOM) the power was reduced to approximately 2mW. The RF signal generator was implemented to scan the frequency of the side bands that the EOM adds. To begin with large steps in frequency of 5MHz and then 3MHz, were slowly made in the range of 1.6GHZ to 100MHz. As no transmitted optical modes were observed, the frequency was then scanned in small steps of 1MHz, quickly and slowly within the same frequency range. Only scattered light was observed during the scanning process. However, occasionally moving ripples would be detected in the scattered light, which was initially thought to be high order modes. But as the detected light moved when the light was slightly misaligned by marginally altering the position of a mirror it was concluded that this was not a transmission from the build-up of light within the cavity.
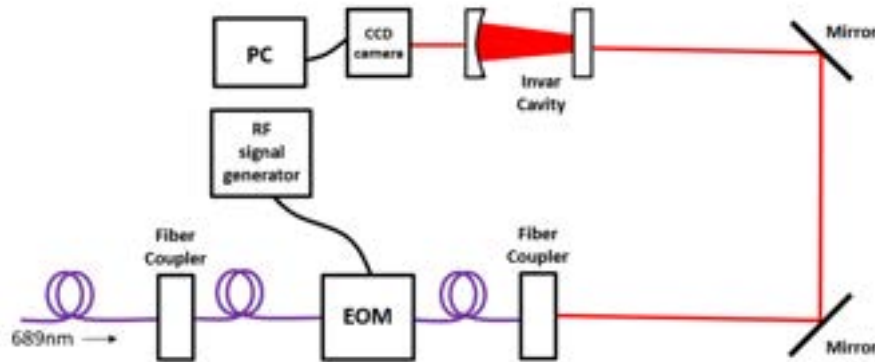
Figure 42: Optical set-up for invar cavity, where the purple lines represent optical fibers, red lines are free space optical paths and the black are electronic paths. Where the EOM stands for the electo-optical modulator, CCD camera is a charged-couple device camera and RF signal generator is a R & S®SMA100B RF and microwave signal generator.

A few steps were made to see if any optical modes could be observed including, altering the position of the CCD camera and swapping the direction of the cavity round so the light was no longer entering the cavity through the planar mirror but instead the curved mirror. Still after no modes were detected, the next step was to question the parallelism of the cavity, as discussed

below.

5.6.1 Parallelism of the Invar Cavity

After no cavity modes where detected during the frequency scan, the parallelism of the two
mirrors was questioned. The distance between the length of the spacer was measured at the top
(above the mirrors) and at the bottom of the spacer (below the mirrors). The top was measured
to be 59.62 ± 0.10mm and the bottom was 59.76 ± 0.10mm, resulting in there being a measured
potential difference in 0.14mm within the length of the spacer, where this difference results in a
tilt of $0.27°$ or 972 arcseconds, which is very sizeable when compared to the normal tilt of <30
arcseconds which the research group here in The University of Birmingham usually works with for
a spacer. However, both length measurements are within the errors of the measurements,
resulting in there being a potential for no sizeable tilt in the ends of the space. Nonetheless, with
both mirrors attached to the spacer is it difficult to accurately measure the tilt as the cavity can
not be laid down on either end. Therefore, to be able to accurately measure the tilt in the spacer
the mirrors will need removing as the potential tilt could be constantly pushing the light away
from the optical axis, resulting in the light not being able to build up along the axis and no
modes being transmitted from the cavity.

5.7 Summary and Applications

With the use of finite element analysis in ANSYS the acceleration sensitivity of the invar cavity
was reduced to 1.53×10^{-12}/g, where a low gradient at the zero crossing was also reduced to
1.7×10^{-12}/mm. At this low gradient, the acceleration sensitivity of the cavity will be reasonably
protected from any errors caused during the printing process. After the invar cavity was printed
and built, it was found that no optical modes could be detected, which is thought to be due to the
large tilt in the parallelism of the cavity.
Therefore, as the parallelism of the invar cavity was found to be potentially off by approximately
972 arcseconds, the next steps were to remove the mirrors so that the parallelism of the cavity can
be accurately measured and alterations made to the invar cavity if necessary. The mirrors were
successfully removed from the spacer with the use of warm water and a detergent, and the spacer
was sent to a workshop within the university. Once alterations are made, the mirrors would need
to be reattached to the spacer, either by the temporary adhesive or by a permanent solution, with
a possible permanent solution being hydroxide catalysis bonding. Unfortunately, due to backlog
the spacer was not returned from the workshop early enough for the cavity to be reassembled.
Once the invar cavity is reassembled the next steps would be to place the cavity back into the

optical system so the stability of the cavity can be tested and measured. If it is found difficult again to find any modes within the frequency scan then the reflected light will also be observed and additionally, mode matching could be attempted.

If the invar space was to be produced again, it is suggest that the print be slightly longer than needed, to allow for the spacer to be accurately polished to make two parallel and smooth ends, for the mirrors to be attached too. Additionally, the tilt in the two ends of spacer should be accurately measured before attaching the mirrors.

This type of compact and portable cavity was initially designed to be used to stabilise a laser for the first stage of cooling of strontium (Sr) atoms (where mirrors with coating for 461nm laser light is used) with a natural linewidth of $\Gamma = 2\pi \times$ 32MHz [50], within a portable strontium optical clock, similar to the clocks mentioned in [14][15]. For the natural linewidth of $\Gamma = 2\pi \times$ 32MHz an optical cavity would require a stability of approximately 1MHz or better (a factor of ten or less of the natural linewidth). As invar displays a low coefficient of thermal expansion of $1.6 \times 10^{-6}/^\circ$C [33], it results in the cavity having a theoretical temperature stability of 100kHz at temperature fluctuations of 96μK, for light at 461nm, which is well within the stability required to be used for the first stage of cooling. To achieve this temperature stability the invar cavity will be placed into a temperature controlled chamber, to minimise any length fluctuations caused by temperature fluctuations.

6   Invar Lattice Cavity

Due to invar being able to be printed into complex shapes, an idea arose, that instead of having a solid material for the spacer of the optical cavity, that an internal lattice could be incorporated. This in turn would reduce the weight of the cavity while still retaining most of the stiffness and strength, resulting in the cavity being less affected by gravity and decreasing the acceleration sensitivity. Here in this Chapter, is a discussion on utilising an internal lattice into a spacer for an optical cavity, as well as an investigation on how the internal lattice structure is optimised, and lastly a description on how the invar lattice cavity was constructed and tested.

6.1   Style of the Lattice Cavity

Originally, the shape and size for the lattice cavity was going to be the same as the solid INVAR cavity, discussed in Chapter 5, to allow for a direction comparison between the two cavities. But after months of designs and simulations it was discovered that as the supports are directly below the lattice, as shown in Figure 43, that no notable improvement could be found. Therefore, a different style of cavity which is vertically mounted was considered and adapted. Both types of cavities and their advantages and/or disadvantages of being used with a lattice are discussed in further detail within this sub-chapter.
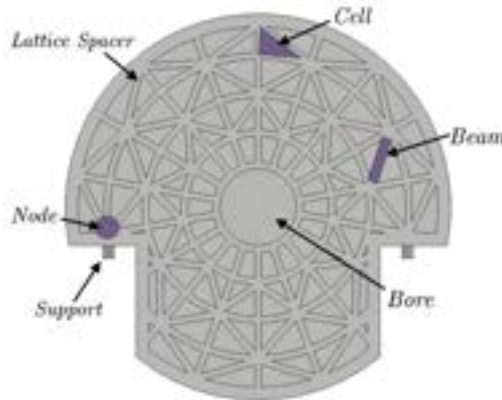
Figure 43: CAD design for horizontally supported invar lattice design, indicating where the supports would sit, including lattice annotations.

6.1.1   Horizontal "Mushroom" Lattice cavity

During the initial lattice tests on the horizontally mounted mushroom cavity, it was found that if a 3D lattice was used within the spacer, then the amount of bending of the spacer around the

supports relied heavily on if the supports were situated in the middle of a cell, on a node, or on a beam of the lattice, creating complications in accurately finding where the supports should be placed, in order to be at the exact zero crossing of the acceleration sensitivity.

Therefore, next lattices which are 2D (similar to as displayed in Figure 43) and extended through the length of the cavity were investigated. When the position of the supports was ranged along the length of the cavity, they would always be placed on the same part of the lattice. Resulting in the smooth and consistent results, similar to if a solid spacer was used. It was found that when the supports are placed directly under a node of the lattice, that this very slightly improved the acceleration sensitivity, compared to a solid spacer. But, due to the weight of the cavity being placed immediately on the lattice, there was too much deformation in the lattice, as displayed in Figure 44, resulting in no significant improvement in the acceleration sensitivity.
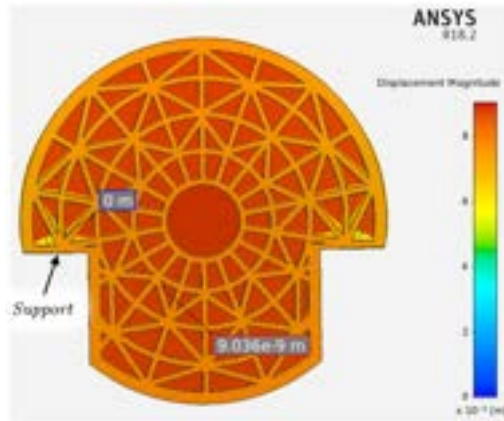
Figure 44: Displacement contour diagrams displaying the effect of vertical acceleration on a horizontally supported lattice cavity, under 1g of acceleration, exhibiting deformation in the lattice structure around the supports. With the scale on the right-hand side of the figure.

It is worth expressing that no topological optimisation or lattice building software was available and that it is almost certainly possible to obtain a significant improvement with this type of cavity, but unfortunately without specialist software or considerably more time available, no significant results were found.

6.1.2 Vertical Lattice cavity

However, if a vertical cavity was used similar to [4] [5] [6] [51], then the lattice would not be immediately placed over the supports, meaning that the lattice would not be directly deformed under its own weight. From these papers there are two slightly different styles to consider when

mounting a cavity vertically. The first is a double cone shape (shown in Figure 45a) and the second is a cylinder shape (shown in Figure 45b). Initially both shapes were investigated to see which would demonstrate the least overall acceleration sensitivity under 1g, when a solid spacer was used.

<div align="center">(a)   (b)</div>

Figure 45: The CAD designs for both types of vertical cavities initially tested, with (a) double cone shape and (b) cylinder shape.

For both shapes shown in Figure 45, the length of the cavity was kept the same at $L/l = 60$mm and the size of the middle rim was also kept constant with a diameter, R_d/r_d of 40mm and length, R_L/r_l of 8mm. As well as all mirrors were the same size with $M_d/m_d = 12.7$mm and $M_L/m_L = 6.35$mm and all support diameters, S_d/s_d were kept at 1mm , with all dimensions of both shapes displayed in Figure 46. It was found very early on that both shapes experience a zero crossing in the acceleration sensitivity (when the overall fractional length change of the spacer crosses zero under 1g), when the support lengths are varied between 1mm and 6mm. The relationship between the acceleration sensitivity and support length was found to be due to the change in how the rim of the cavities change shape in the axial displacement, as the support length is increased.

(a) Double cone, design

(b) Cylinder, design
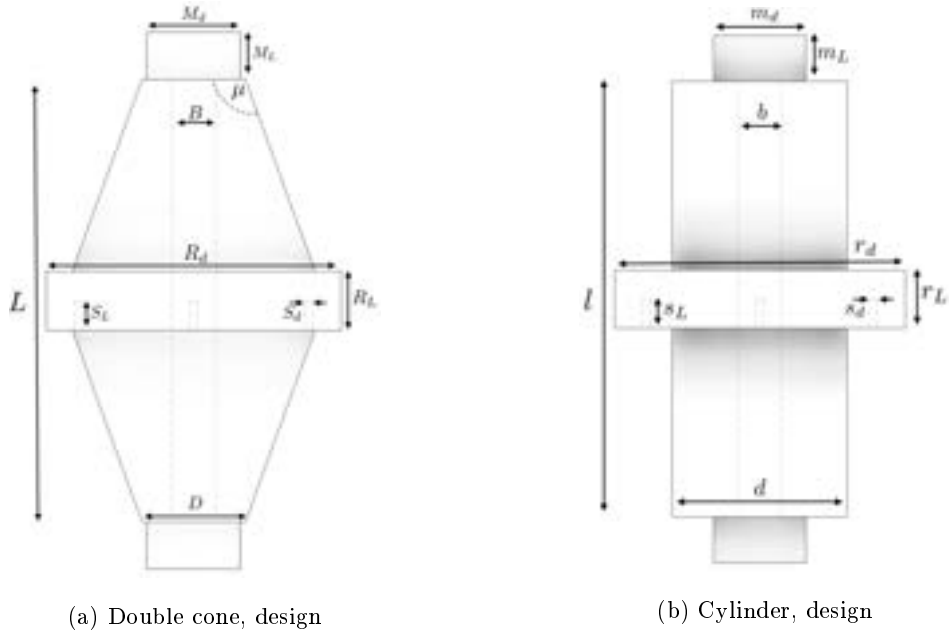
Figure 46: Diagran of the geometries of each vertical cavity design with dimensions.

For the double cone shape, firstly the effect of changing the angle of the cone, μ on the fractional length change of the cavity under 1g was explored, while the length of the supports, S_L was kept constant at 4mm and where $D = 14$mm. As seen in Figure 47, as the angle, μ is initially reduced from 110°, the fractional length change dramatically falls until $\mu \approx 100°$ where it appears to level off and even slightly increase. This relationship could be relating to the specific support length, S_L at which the acceleration sensitivity crosses zero being decreased as the angle is reduced or the gradient of the acceleration sensitivity graph being altered or both. To explore this further, the next step taken was to look into the fractional length change of the cavity under 1g with various angles, against varying support lengths.
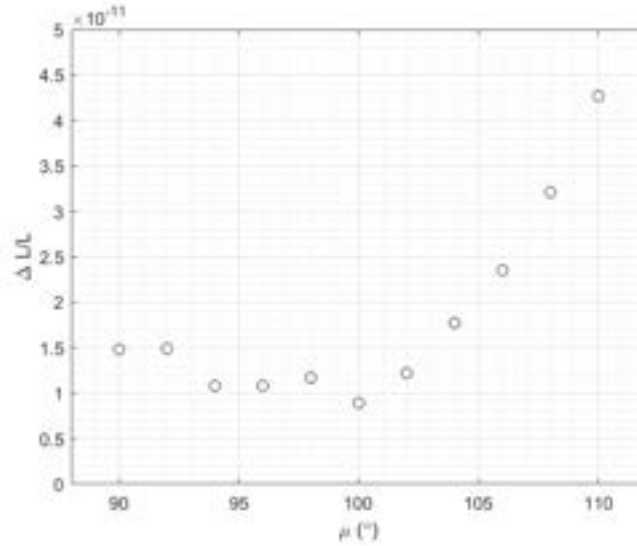
Figure 47: The acceleration sensitivity (fractional length change $\Delta L/L$) under 1g of vertical acceleration versus the angle, μ of the double cone optical cavity shape, when solid and vertically mounted, with $S_L = 4mm$, with the error bars not visible on this scale. Data from simulations computed on ANSYS.

As seen in Figure 48a, it shows that both the gradient of the acceleration sensitivity and the support length in which the data crosses zero is slightly different for each angle, μ of the double cone design. Interestingly, it was found that when $\mu \approx 109°$ the gradient of the acceleration sensitivity flips sign from negative to positive, indicating that there is a specific range of cone angles, μ for which the gradient is minimised. Figure 48b shows that when $\mu = 109°$, there is no zero crossing in the acceleration sensitivity but when $\mu = 110°$ the gradient becomes completely positive and the graph crosses zero when $S_L \approx 3.3$ mm. Similarly, when $\mu = 108°$ the gradient becomes completely negative and has a zero crossing around $S_L \approx 5.6mm$. Therefore, it can be concluded that the optimal angle for the double cone cavity shape with the set dimensions given earlier is just either side of 109°, as this is where the gradient of the acceleration sensitivity is at its lowest when crossing zero.
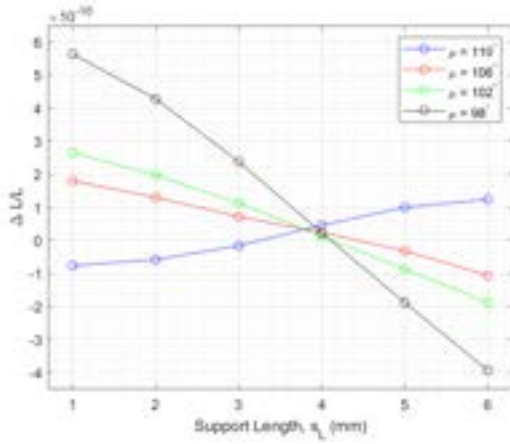
(a) Where $\mu = 110°, 106°, 102°, 98°$ (b) Where $\mu = 110°, 109°, 108°$
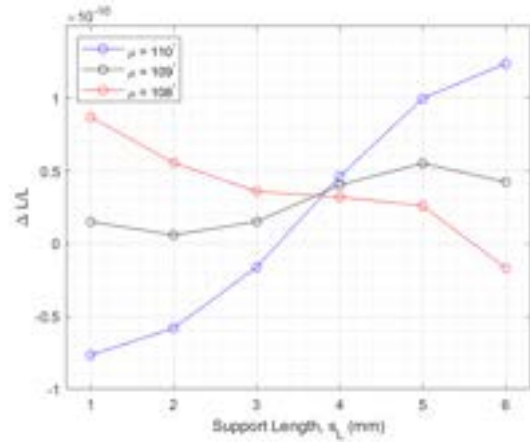
Figure 48: The acceleration sensitivity (fractional length change $\Delta L/L$) under 1g of vertical acceleration versus the support length, s_L for a range of different cone angles, μ, for the double cone optical cavity shape, when solid and vertically mounted. The points are connected to guide the eye, with the error bars not visible on this scale. Data from simulations computed on ANSYS.

For the cylinder shape the spacer diameter, d was varied between 14mm and 32mm with the support length, $S_L = 4$mm. As seen in Figure 49, the cylinder shape appears to display a similar pattern to the double cone shape as at larger radii, the cavity is showing larger fractional length changes, but for a portion of diameters ($\approx 14 - 24$mm), there is no obvious change. Next, the gradient and the zero crossing of the acceleration sensitivity was analysed for individual diameters.

Figure 49: The acceleration sensitivity (fractional length change $\Delta L/L$) under 1g of vertical acceleration versus the spacer diameter, d of the cylinder optical cavity shape, when solid and vertically mounted, with $S_L = 4mm$, with the error bars not visible on this scale. Data from simulations computed on ANSYS.

Firstly for diameters, $d = 16,20,24$ mm the fractional length change, $\Delta L/L$ was plotted versus the support length, s_L. As seen in Figure 50a, there are minor changes between the different diameters. But for $d = 20$mm and $d = 24$mm they almost have identical results, whereas when $d = 16$mm, the gradient of the fractional length is slightly reduced. However, when the larger diameters were tested, they showed substantial changes in the gradient and zero crossing. Similarly to the double cone shape at larger angles, μ the cylinder shape shows a change in gradient to positive when $d \approx 31$mm as shown in Figure 50b, resulting in there too being a range of diameters for which the gradient of the acceleration sensitivity is minimised.

When incorporating a lattice to reduce the weight of the spacer it was found to be difficult to find a zero crossing, if the gradient of the acceleration sensitivity was negative, as this would increase the length of the support hole beyond where the spacer rim was, resulting in no zero crossing being found. Whereas, when the gradient was positive for most lattice structures a zero crossing could be found when $S_L/s_L \approx 1.5 - 3.5$ mm. Hence when selecting the geometry of the spacer it was preferable to choose an angle, μ or diameter, d that showed a positive gradient in the acceleration sensitivity.

(a) Where $d = 16, 20, 24mm$ (b) Where $d = 28, 30, 32mm$

Figure 50: The acceleration sensitivity (fractional length change $\Delta L/L$) under 1g of vertical acceleration versus the support length, s_L for a range of different spacer diameters, d, for the cylinder optical cavity shape, when solid and vertically mounted. The points are connected to guide the eye, with the error bars not visible on this scale. Data from simulations computed on ANSYS.

As, ultimately either style could be used, it really came down to which shape would be the best suited to be used with an internal lattice and to be fabricated using selective laser melting. For the double cone shape the ideal angle, μ would be 110° and similarly for the cylinder shape the ideal diameter, d would be 32mm. Therefore, for both shapes the acceleration sensitivity was plotted against support length, S_L/s_l, as shown in Figure 51. Both shapes display almost identical relationships, with very similar zero crossings. But the double cone shape exhibits a very slight reduction in the gradient and as the cone shape will have a smaller volume compared to the cylinder shape, it will have a lower print time, making the double cone shape the more preferable out of the two, to use for the vertical lattice cavity.

Figure 51: The acceleration sensitivity (fractional length change $\Delta L/L$) under 1g of vertical acceleration of solid cylinder vertically mounted cavity with diameter = 32mm (black line) against a solid bicone vertically mounted cavity with angle, $\mu = 110°$ (blue line), when both are solid. The points are connected to guide the eye, with the error bars not visible on this scale. Data from simulations computed on ANSYS.

6.2 Lattice Considerations

Once the style of the vertical cavity was selected, next was incorporating an internal lattice. As no lattice optimisation software was available, all lattice designs where designed by hand and individually created as CAD designs in Autodesk Inventor, before being structurally analysed using finite element analysis in ANSYS. There was a number of features of the internal lattice which where considered, including the size of the lattice cells, the type of lattice cells, the thickness of the outer shell and the proportion of the cavity which was to contain a lattice. Later on in Section 6.3 while optimising the final lattice structure, the thickness of the lattice is also explored. From primary simulations there was a number of observations noticed, the first being was when there is an integer number of cells along the length and width of the cavity this allows the cavity to keep a good proportion of stiffness, when compared to when part cells are incorporated. Additionally, if the cell size of the lattice was too small this would cause a number of issues in the testing process, the first being that ANSYS (student version R18.2) has a limit in it's meshing of 32k cells/nodes for a structural model. Therefore, if the lattice cell size is too small it results in ANSYS being unable to mesh the entire geometry. Another disadvantage of small lattice cells is this drastically increases the time needed to design and simulate each geometry, therefore as a

87

result no lattice with a cell size less than 2mm was investigated fully.

The first stage in designing the lattice cavity was to find the optimal lattice structure and the type of lattice cells this would include. Due to the vertical cavity's shape and for ease of creating each lattice design, every lattice structure was designed in 2D along the optical axis, between both mirrors and revolved round the optical axis. Figure 52 shows a couple of examples of lattice structures which were designed and tested. Any lattice structure that was designed that did not align with this type geometric design, was found to not have a zero crossing in the acceleration sensitivity when tested. It is worth noting that if optimisation software was available then there probably would have be other types of lattice structures found that are suitable for this type of cavity.

(a) (b)
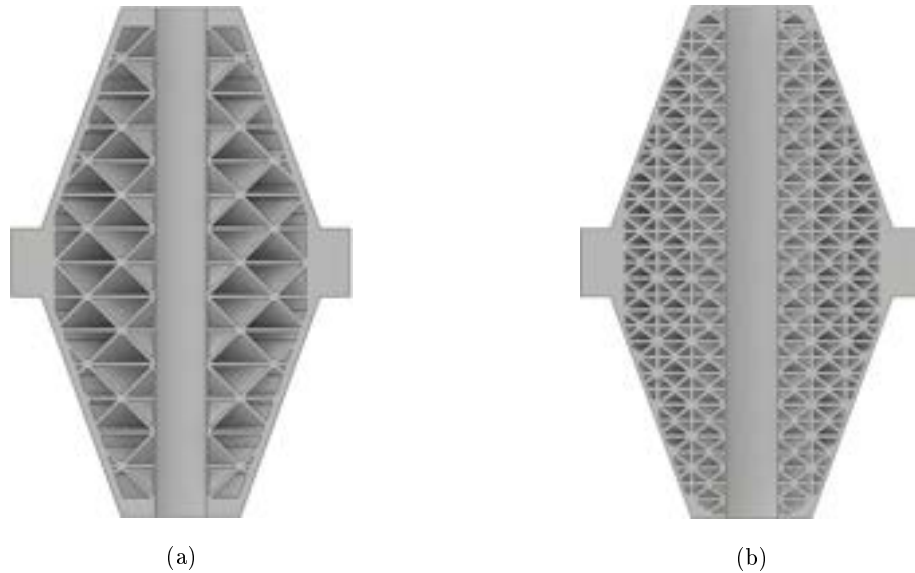
Figure 52: Two representations of the types of lattice structures which were designed and tested for the lattice cavity. Any structure that was designed and tested that did not align with this type geometric design, was found to not have a zero crossing in the acceleration sensitivity.

After multiple types of lattices structures were designed and tested and it was found that lattices with square lattice cells, straight vertical and horizontal beams (when compared to the optical axis) and diagonal beams connecting them deformed the least when placed under 1g, and had the best weight to stiffness ratio. This type of lattice is displayed next in Figure 53 where other properties of the vertical cavity is explored, to further reduce the acceleration sensitivity.

In the next stages of designing the internal lattice the shell thickness, size and the proportion of the cavity to include a lattice was observed. It was found that if the outer shell of the cavity was

too thin as displayed in Figure 53a, when compared to the design shown in Figure 53b, this would cause the stiffness of the cavity to be greatly reduced. Whereas, if the shell was too thick this would result in the weight of the cavity not being reduced enough to observe a notable reduction in the acceleration sensitivity. It was concluded that a thickness between 1-1.5mm would be suitable for this 60mm × 40mm sized cavity, with the top and bottom part of the shell being slightly thicker at around 2mm. Additionally, the optimal lattice cell size was found to be 4mm × 4mm and if the size of the lattice cells was smaller or larger than this, it would have a negative affect on the stiffness of the lattice structure.

(a)   (b)
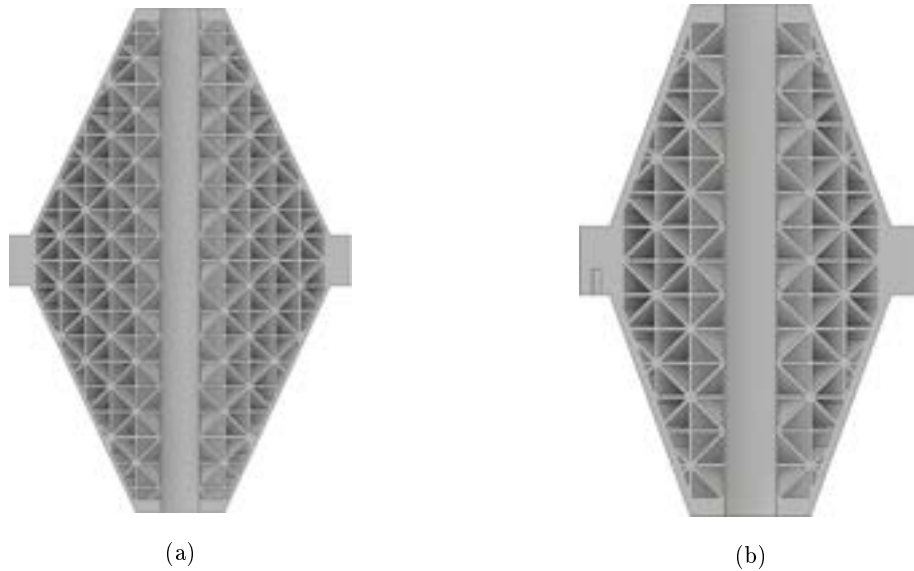
Figure 53: Two representations of internal lattice structures, designed for the invar lattice cavity, showing a direct comparison of a thin outer shell, as shown in (a) and a thicker outer shell, as shown in (b).

When investigating the proportional amount of the cavity which was to include the lattice, it was explored firstly the effect of having part of the inner rim solid and secondly the effect of having the entire inner rim to be solid. For example in Figure 54, it displays these two different options, where Figure 54a has part of the inner solid and Figure 54b and the entire inner rim full.

(a)   (b)
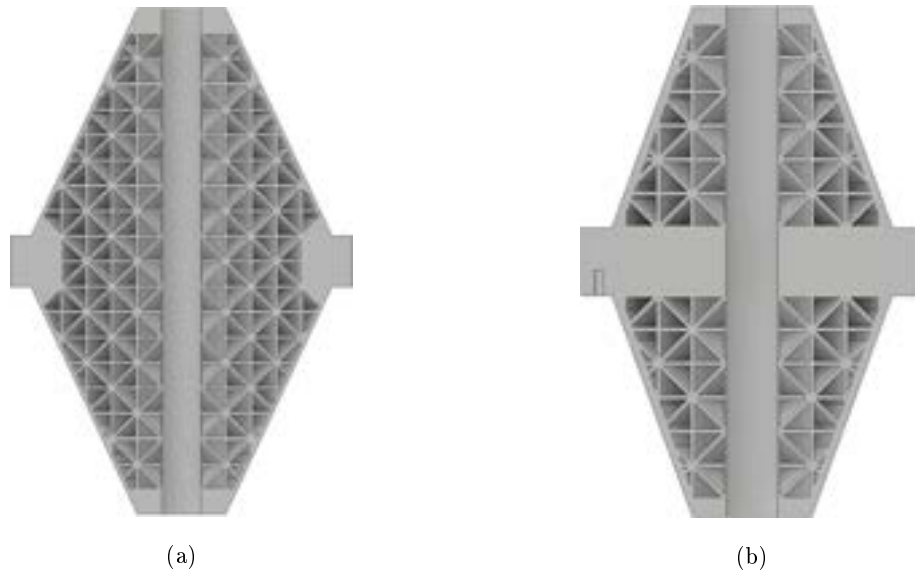
Figure 54: Two representations of internal lattice structures designed for the invar lattice cavity with different proportional amounts of the inner rim being solid, as shown in (a) being part solid and (b) being entirely solid.

It was found that by making the entire or even part of the inner rim solid that this does increase the stiffness of the cavity, but also adds to much weight to the structure. It was not investigated looking into including the internal lattice to the outer rim of the cavity as this is where the support holes lay.

It was also explored briefly if the weight of the cavity could be minimised by simply hollowing out the cavity spacer or hollowing out certain parts of the spacer. However, without a continuous internal lattice structure the results from the simulations showed these structures produced similar or higher vibration sensitivities when compared to the initial solid version.

6.3   Optimising the Final Lattice Structure

Figure 55 displays the lattice which was found to exhibit the leading ratio of weight reduction to stiffness retention out of all the designs tested. The lattice design is composed of approximately 30 square cells (4mm × 4mm sized cells), containing two isosceles triangles, revolved around the optical axis (y-axis in the case of vertical cavities). With a shell thickness of 1mm around the lattice and with a thickness of 2.25mm at the top and bottom of the structure, where the mirrors sit.
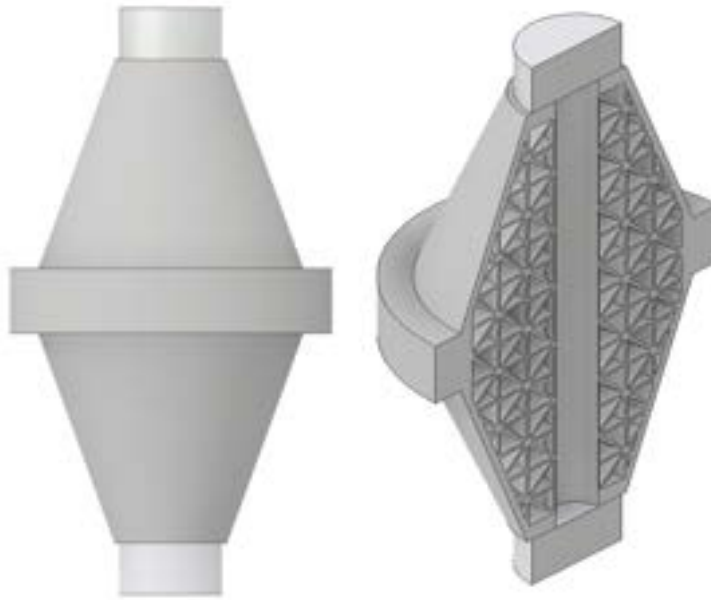
Figure 55: CAD design of the vertical lattice cavity. On the left is the full design and on the right is a cross section of half the cavity.

6.3.1 Ideal Improvement

To see how much the acceleration sensitivity can be decreased against the amount of weight reduced, an "ideal improvement" test was completed. By lowering the density value of the INVAR material in ANSYS and keeping all other parameters constant, this ensured that there was no change in the stiffness and a direct comparison could be made. The density was reduced from 8055kgm^{-3} to 4055kgm^{-3} and 2055kgm^{-3}, which were approximately a 49.7% and 74.5% decrease in weight respectively.
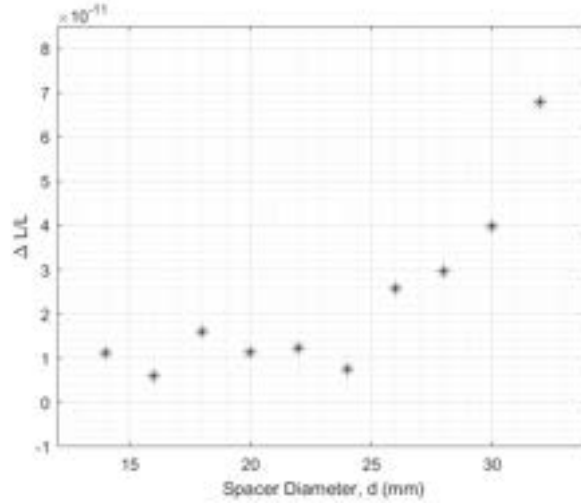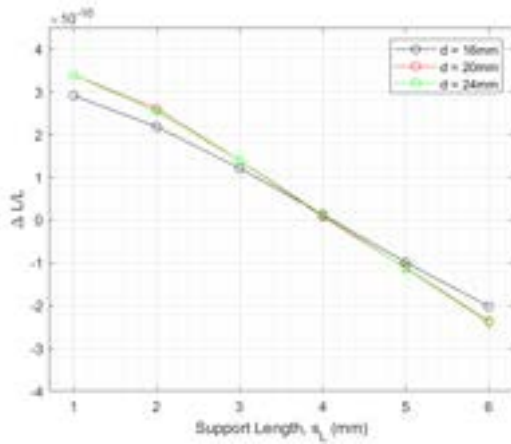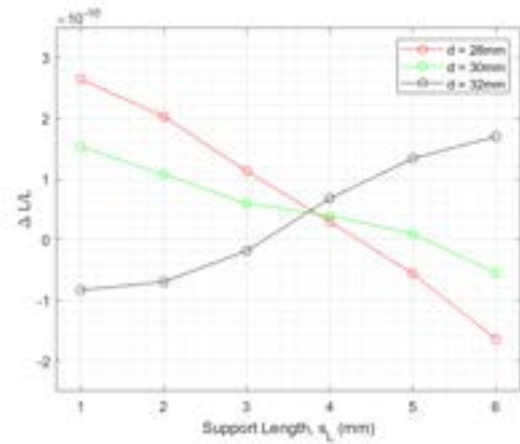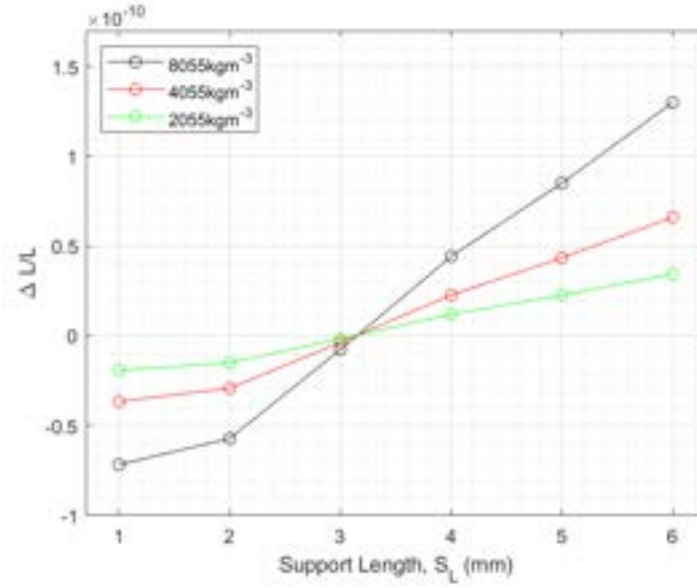
Figure 56: The acceleration sensitivity (fractional length change $\Delta L/L$) under 1g of vertical acceleration of the invar vertical double cone cavity versus support length, S_L for different densities of invar in-putted into ANSYS, as denoted by the key in the top left-hand corner. The points are connected to guide the eye, with the error bars not visible on this scale. Data from simulations computed on ANSYS.

As seen in Figure 56, by reducing the density and in turn the weight of the spacer, the zero crossing of the fractional length change of the cavity is decreased. With a density of 8055kgm^{-3} the zero crossing gradient was found to be $\approx 5.91 \times 10^{-14}$m^{-1}. When the density of the INVAR was altered to 4055kgm^{-3} and 2055kgm^{-3}, the corresponding zero crossing gradients were $\approx 2.63 \times 10^{-14}$m^{-1} and $\approx 1.36 \times 10^{-14}$m^{-1}, showing a $\approx 49.2\%$ and $\approx 73.9\%$ reduction in the zero crossing gradient respectively. From this, it is clear that the amount the weight is lowered to is a rough comparison to the limit to which the gradient can be reduced and in turn the limit to which the acceleration sensitivity of the cavity can be reduced to. So if the weight of the spacer is halved with the use of an internal lattice, it can be expected that the improvement on the acceleration sensitivity could be as high as 50%, assuming the stiffness of the cavity is kept constant with an optimal lattice design.

6.3.2 Optimising the Lattice Size

To optimise the lattice shape as shown in Figure 43, two approaches were taken. One was to alter the size of the lattice cells and the next was to vary the thickness of the lattice. When the lattice

cell size was increased or decreased, it resulted in there being part lattice cells within the rim of the spacer design. When these part cells were present in the lattice, the overall stiffness would be greatly affected, causing the lattice to deform and in turn increase the fractional length change. The second approach was to change the lattice thickness, LT as defined in Figure 57. The lattice thickness was initially at 0.25mm and was later adjusted to 0.2mm and 0.3mm.
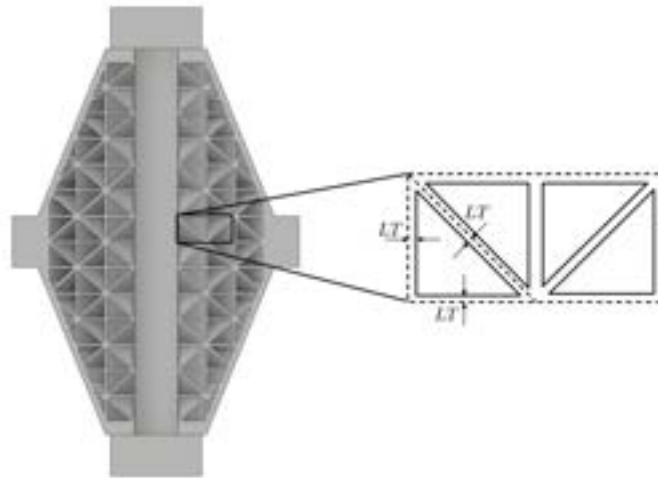
Figure 57: Zoomed in image of the lattice, for the invar lattice cavity, displaying the lattice thickness, LT dimensions

It was found as the lattice thickness was increased to $0.3mm$, this increased the weight of the cavity and in turn increased the zero crossing gradient of the acceleration sensitivity. Whereas, when the lattice thickness was decreased to 0.2mm the zero crossing gradient was further reduced. A direct comparison between each lattice thickness and initial spacer '*Full*' (representing the initial solid spacer) can be seen in Figure 58. When the lattice thickness was further narrowed to 0.15mm, this showed to weaken the structure too much and had a negative effect on the acceleration sensitivity.
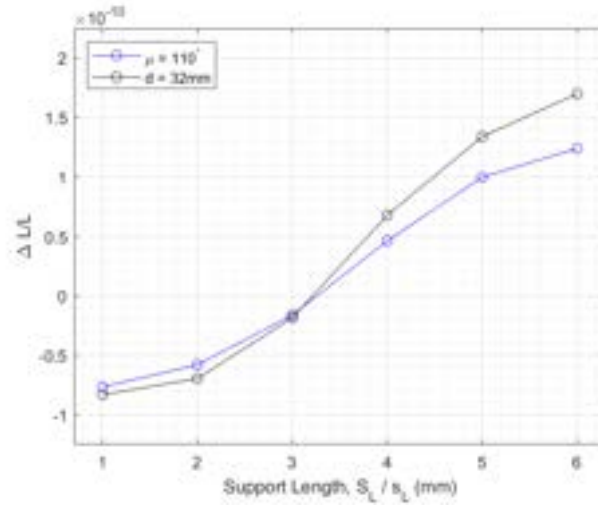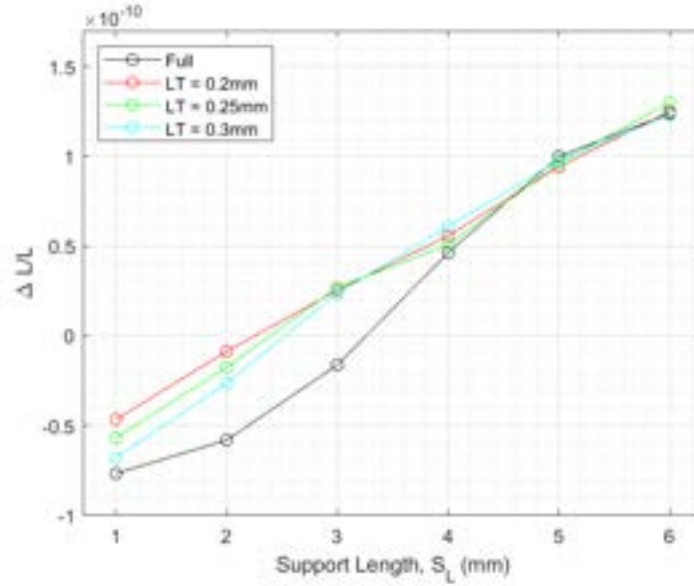
Figure 58: The acceleration sensitivity (fractional length change $\Delta L/L$) under 1g of vertical acceleration for the lattice invar cavity, versus the support length, S_L for the solid spacer, 'Full' and each Lattice thickness, LT, as denoted in top left-hand corner. The points are connected to guide the eye, with the error bars not visible on this scale. Data from simulations computed on ANSYS.

The initial weight of the solid spacer was 0.258kg and was initially reduced by 45% to 0.142kg for the $LT = 0.25$mm lattice. At this weight the spacer displayed a 28.6% decrease in the gradient at the zero crossing of the acceleration sensitivity which allowed for a 30.1% lowered acceleration sensitivity when compared with the solid spacer.

	Full	$LT = 0.2$mm	$LT = 0.25$mm	$LT = 0.3$mm
Zero Crossing gradient	6.23×10^{-11}/mm	3.40×10^{-11}/mm	4.45×10^{-11}/mm	5.00×10^{-11}/mm
Weight	0.258kg	0.128kg	0.142kg	0.155kg
Reduction in Weight	N/A	50.4%	45.0%	40.0%
Reduction in Zero Crossing gradient	N/A	45.4%	28.6%	19.7%
$\Delta L/L$	3.26×10^{-12}/g	1.97×10^{-12}/g	2.28×10^{-12}/g	3.72×10^{-12}/g
Reduction in $\Delta L/L$ under 1g	N/A	39.6%	30.1%	$Increased - 14.1\%$

Figure 59: Table to show the comparison of properties for each lattice thickness, LT and the solid spacer for the vertical lattice cavity. Data from simulations computed on ANSYS.

However, when the lattice thickness was increased from 0.25mm to 0.3mm this gave the lattice spacer a weight of 0.155kg which is 40% lower than the initial solid spacer. Even though this lattice thickness displayed a 19% reduction in the zero crossing gradient, when the acceleration sensitivity was obtained, it was found to be slightly higher than the solid spacer. It is unclear why

it negatively affects the acceleration sensitivity, but it may be due to the lattice marginally deforming more when the support length is $\approx$ 2.5mm (the approximate support length where the $LT = 0.3$mm acceleration sensitivity crosses zero).

But when the weight was reduced to 0.128kg for $LT = 0.2$mm this decreased both the zero gradient and the acceleration sensitivity further than the $LT = 0.25$mm lattice, to give a total reduction in the zero gradient of 45.4% and a decrease of 39.6% in the acceleration sensitivity, when compared to the solid spacer. A direct comparison between all lattice thickness's and the solid spacer can be seen in Figure 59. From this table it is clear that when the lattice thickness is 0.2mm this has the most significant impact in minimising the acceleration sensitivity.

6.3.3   Final Dimensions

Once the inter lattice was optimised the final step in designing the spacer was to find the support length where the acceleration sensitivity was ultimately minimised. By varying the length of the supports by 0.2mm increments around the zero crossing, as shown in Figure 60, it was found that the ideal length of the supports is at 2.2mm.
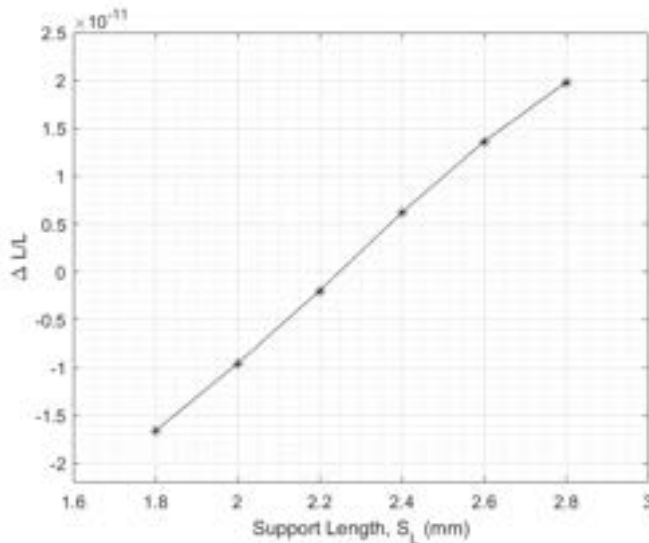
Figure 60: The acceleration sensitivity (fractional length change $\Delta L/L$) under 1g of vertical acceleration of the finalised lattice cavity structure (using the dimensions from Table 5), versus the support length, S_L. The points are connected to guide the eye, with the error bars not visible on this scale. Data from simulations computed on ANSYS.

Lastly, the complete final dimensions for the lattice cavity can be found in Table 5. With these dimensions the lattice cavity displays an over fractional length of 1.97×10^{-12}/g, which is

approximately 40% lower compared to 3.26×10^{-12}/g for a solid spacer of the same dimensions. While this is not an incredible improvement it shows confirmation that the acceleration sensitivity of an optical cavity can be decreased by reducing the weight of the spacer, with the use of an internal lattice.

Table 5: Final dimensions for invar lattice Cavity.

Parameter	Final Value
L	60mm
B	6mm
R_L	8mm
R_d	40mm
M_L	6.35mm
M_d	12.7mm
S_d	1mm
S_L	2.2mm
μ	110°
LT	0.2mm

For the final lattice design the finite-element analysis can be seen in Figure 61. On the right side is the full cavity, which is supported at the three support holes and on the left side is half the geometry, supported on the two supports within the half and constrained by the half-face. As shown in the figure, there is little deformation within the lattice and the majority of the axial displacement is within the rim of the spacer, allowing for minimal fractional length change between the centre of the two mirrors.
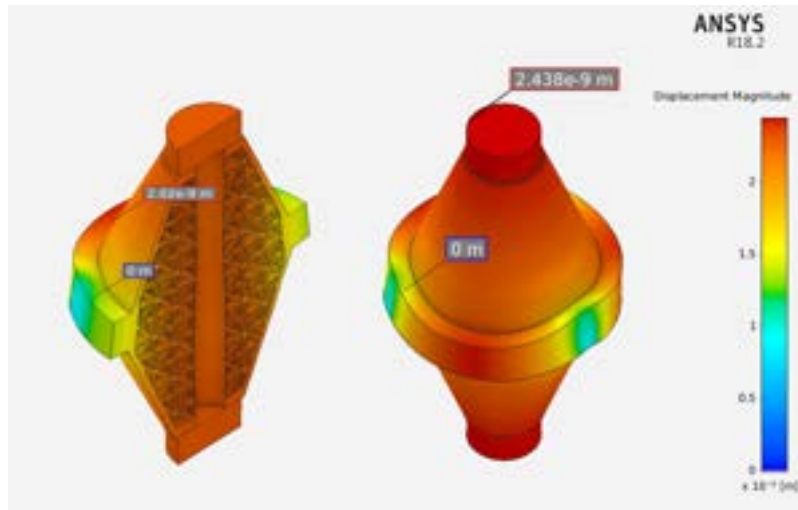
Figure 61: Displacement contour diagrams displaying the effect of vertical acceleration on the final lattice cavity under 1g of acceleration. With the left-hand geometry being a cross section of half the cavity and the right side is the full design. The scale is on the right-side of the figure.

6.3.4 Supporting the Lattice Cavity

It is vital that the weight of the cavity is placed at the specific length of the supports holes, in order to keep the acceleration sensitivity to a minimum. To ensure the weight is accurately placed and due to issues with printing such a complex shape, it was decided that the support of the cavity and the spacer were printed as two separate pieces.

For the support structure, ultimately it needed to be minimal, in order to reduce the printing time, while at the same time retaining a reasonable level of stiffness. The design is constructed of three main poles, three thin support poles and a base, which will all be printed together as one body. As shown in Figure 62a the base has four M6 clearance holes with 6.6mm diameters. On each side of the base the holes are separated by 25mm and along the length of the base they are 50mm apart, to ensure the support structure can be secured on to the optical table. The three support poles are 0.9mm in diameter and 3.2mm in length, to allow them to link flawlessly with support flanges (dimensions were chosen slightly smaller than the support holes, to give account for printing uncertainties).

(a)

(b)
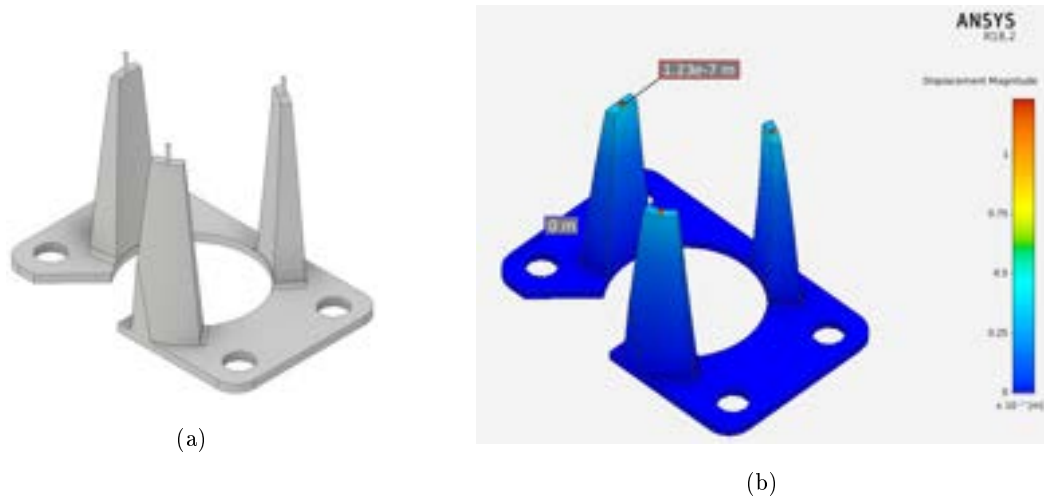
Figure 62: The design for the support structure of the lattice cavity, with (a) the initial CAD design and (b) the displacement contour diagram displaying the effect of vertical acceleration on the three support polls under the weight of the cavity. With the scale on the right-hand side.

Lastly the three main poles led from the base to the thin support poles, with chamfers of various degrees on every side of each pole (between the poles and the base). The chamfers are used to reduce the bending in the main poles, once the cavity is placed on top. The support structure was simulated multiple times while being designed to ensure reasonable stiffness is present. The displacement magnitude of the final design is shown in Figure 62b, which displays only notable displacement in the thin support polls, which is to be expected.

6.4 Constructing the Lattice cavity

Initially, the lattice cavity spacer was to be printed as a whole, but after a few attempts of trying to print the spacer in this way, it was found that the left over invar dust was getting stuck within the cells of the lattice. Due to the lattice being completely enclosed, there was no way of removing the extra dust or any trapped air (that could cause problems if the cavity was to be placed under vacuum for thermal isolation). Firstly, it was thought to add small 1mm holes per lattice cell to the design to remove the dust, but the initial simulations showed that the added holes had a large effect and increased the acceleration sensitivity of the cavity, due to them decreasing the sturdiness in the outer shell of the spacer.

This led to the idea that the lattice spacer could be printed in two halves and then later joined. As shown in Figure 63, when the lattice is divided in two halves parallel to the bore, this results in there being no enclosed lattice cells. Also, when the two halves are printed with the sliced face

downward, this produces a much simpler geometric design (minimal hangovers) to print. With time restrains, it was decided to go ahead with printing the spacer in two halves, as redesigning the spacer with limited time was deemed too uncertain. For the supporting base of the cavity, no issues were found while printing the structure.

Figure 63: Final CAD design for the lattice spacer, in two halves to display the internal lattice.

The final printed lattice spacer and supporting base are shown in Figures 64 and 65, respectively. As seen in Figure 64b, the lattice spacer on one half of the outer shell has a sizeable print error. This type of print error is likely produced due to the complex structure of the lattice cavity and chance of these types of printing errors can reduced by using a slower lasing speed for the SLM. While this will affect the performance of the cavity, as the error is only in the outer shell of the design and not affecting the structure of the lattice, the current print was used instead of trying to reprint the half. This decision to not reprint also related to the time and cost to print each half of the spacer, as well as the the print wait time on the SLM machine.
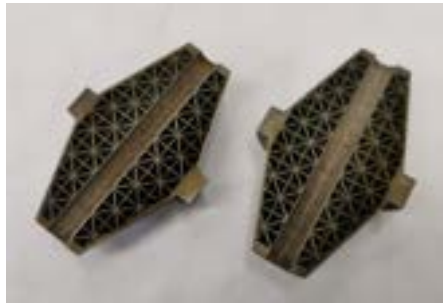
(a)   (b)

Figure 64: Final printed lattice spacer using SLM as discussed in Chapter 5.2. (a) both halves upright showing the internal lattice and (b) both halves face down to show the outer shell.

Figure 65: Final printed lattice support structure using SLM as discussed in Chapter 5.2.

The first stage in constructing the lattice cavity was to attach the two spacer halves together. While being printed both halves gained small printing errors and had small indents on the rims. Therefore, both sides needed to be flatten down before joining them together. Initially, both sides were to be flattened using a milling machine. But it was found that the lattice structures were not stiff enough to withstand the force of the milling machine. Resulting in the one lattice structure becoming slightly deformed, as shown in Figure 66a. Therefore, a different route was taken in finishing off smoothing the lattice faces. The first lattice half was finished off by hand sanding and the second lattice half was completely hand sanded.

(a)   (b)

Figure 66: The lattice spacer with (a) dis-figuration in the lattice structure, after the lattice spacer half was electrically sanded, and (b) final sanded down lattice spacer halves.

Both sanded halves are shown in Figure 66b. Just before attaching, both halves were cleaned using an ultra sonic bath and left for a couple of hours to allow the solvent to completely evaporate from within the lattice structure. To attach both halves, simple super glue was used, as it was a non-permanent adhesive that was ideal for a metal-metal attachment. It is unknown the effect that the super glue would have on the thermal and mechanical sensitivity of the cavity. The idea for using super glue is that it is a non-permanent adhesive to initially bond the cavity for testing, therefore, a more appropriate permanent adhesive will be used for the final construction. The next stage in constructing the lattice cavity was to add new holes in the rim of the spacer, as during 3D printing the support holes in the rim were too small, as not enough tolerance was given between the diameter of the holes, to the diameter of the support poles. Also during sanding of both halves of the spacer, the spacer became slightly deformed from the initial circular shape, as shown in Figure 67a. The new holes were drilled 60 degrees away from the initial holes, as displayed in Figure 67b.

(a)   (b)

Figure 67: Final assembled lattice spacer with, (a) initial deformed support holes from the SLM and (b) after the new support holes were added to the cavity's rim.

Once the new holes were added, the last stage in building the lattice cavity was to attach the FS mirrors. Both mirrors are 6.35mm in length and 12.7mm in diameter with a reflectivity of 99.97% ($\pm$0.02%) for 689nm light. Firstly both the spacer and the mirrors were cleaned. Both mirrors were then attached using a Norland optical adhesive (NBA107). The adhesive is a temporary bonding adhesive, that needs UV light for curing. It is designed to be used to temporarily bond polished optical components to polished metal surfaces. This adhesive was originally used to allow for the mirrors to be easily removed by simply using hot water with some added detergent or using acetone, in case further adjustments were needed to be made to the spacer.

Figure 68: Image of the fully constructed hemispherical lattice cavity, ready for testing.

The bottom mirror is a plane-planar mirror, while the top mirror is concave with a radius of curvature of 500mm ($\pm$0.5%), making the cavity a hemispherical cavity, with the built lattice

shown in Figure 68. Similarly to the invar cavity, these mirrors were used for the initial testing of the lattice cavity as they were already available in the laboratory. For the final construction of the lattice cavity, new mirrors with appropriate radius of curvature for the length of the cavity and coating for the wavelength of the type laser being used with the cavity, will be utilised.

For the the initial mirrors used with the lattice cavity, the stability of the cavity was calculated using the stability condition mentioned in Section 2.5. Where g_1 is the planar mirror and equal to one and g_2 is the concave mirror and equal to 0.88, it is evident the cavity sits well within the stability condition:

$$0 \leq g_1 g_2 \leq 1 \tag{48}$$

as $g_1 g_2 = 0.88$. As one mirror is planar this results in the cavity being especially robust to misalignment.

Similarly as with the invar *"mushroom"* cavity in Chapter 5 this cavity should display an approximate finesse of 1.05×10^4, as the mirrors have reflectance's of 99.97%, but as each mirror has an error on the reflectance of 0.02% the finesse could range from 6280 to 3.14×10^4. Also if the cavity retained its initial length of the cavity of 60mm, it would have resulted in a free spectral range of 2.500×10^9Hz and following this a linewidth of 2.38×10^5Hz (assuming the reflectances are 99.97%).

But from printing errors and through some of the alterations made after the two spacer halves were printed, including sanding the ends of the cavity, the actual cavity length is measured to be $\approx 60.1 \pm 0.1$mm, which results in the cavity having a slightly lower free spectral range of $\approx 2.49 \times 10^9$Hz.

6.5 Testing the Lattice cavity

Similarly to the invar cavity mentioned in Chapter 5, the lattice cavity was initially placed within a simple optical system, as shown in Figure 69 with the diagram for the optical setup shown in Figure 70.
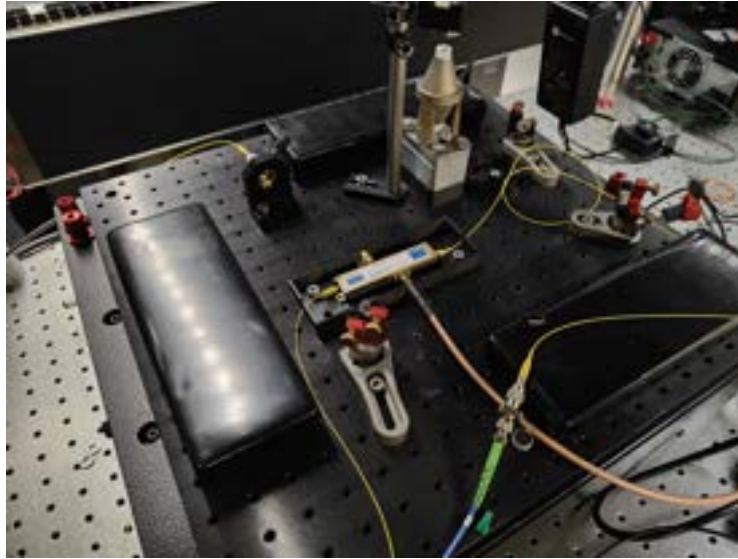
Figure 69: Image of the laboratory optical set-up for the lattice cavity, with the optical system on the Minus-K platform.

The incoming 689nm laser light enters the bay from a long 20m optical fibre, which is coupled to another bay within the laboratory. The initial incoming power to the long fibre is approximately 30mW but after passing through the long fibre and through the electo-optical modulator (EOM), the power is reduced to approximately 2mW. The EOM adds sides bands to the incoming signal while the RF signal generator, scans the side bands through a range of frequencies. The light is then aligned into the lattice cavity by utilising three mirrors. A CCD camera is above the lattice cavity to detect the transmitted light from the cavity. The entire free space optical system is on a Minus-K platform to reduce the magnitude of external vibrations the system experiences.
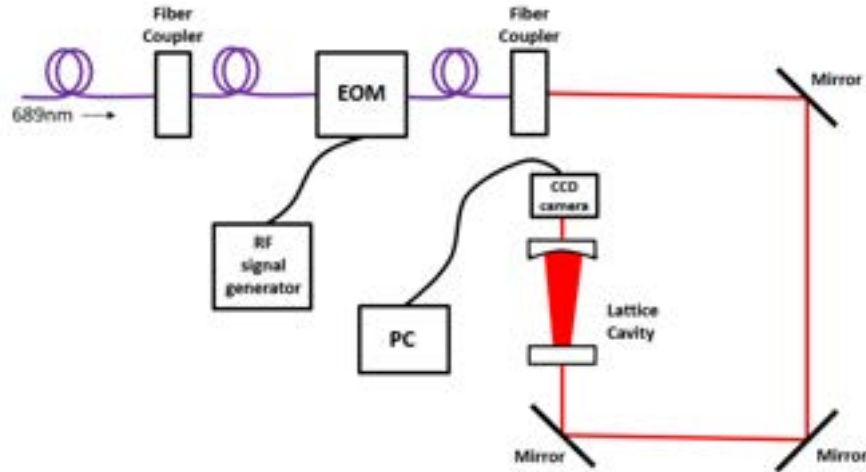
Figure 70: Optical set-up for lattice cavity, where the purple lines represent optical fibres, red lines are free space optical paths and the black are electronic paths. Where the EOM stands for the electro-optical modulator, CCD camera is a charged-couple device camera and RF signal generator is a R & S®SMA100B RF and microwave signal generator.

After multiple attempts to see a mode signal from the lattice cavity onto the CCD, by making large steps in the frequency of the side bands between 1.6GHz and 100MHz of 5MHz and then 3MHz slowly and by making small steps of 1MHz both quickly and slowly, within the same frequency range, no signal was detected. As the full range of the free spectral range of the side-bands was covered, this resulted in a few ideas to investigate why no mode signal is being observed as mentioned below.

6.6 The Next Steps

The next steps for the lattice cavity are to firstly, accurately measure the parallelism of either end of the lattice cavity. A calliper was initially used and showed that within reason, the length of the cavity at either end of each mirror flat is 60.1±0.1mm, so the cavity should be reasonably parallel. But it is difficult to accurately measure a length to the precision which is required here with a calliper. So a more accurate method where a dial indicator needs to be utilised to allow the parallelism of the cavity to be measured to the nearest 30 arcseconds. Once measured, if adjustments need to be made to the parallelism of the lattice cavity, then the mirrors would be detached using warm water and detergent, to remove the temporary adhesive to allow adjustments to be made to the geometry of the spacer.

Secondly the CCD camera could be used such that it is focused on the inner mirror surface so the light bouncing off the mirror's coating could be studied to try and calculate where and if there is any build-up of light within the cavity. Also, the reflected light could be observed for frequency modes and mode matching could be attempted.

In addition the lattice could be redesigned such that it could be printed in one piece, to remove any uncertainties that have arisen by having the spacer printed in two halves and attached together, as discussed below.

6.6.1 Improvements to the Lattice Spacer geometry

To ensure the lattice spacer could be printed as one component, small holes of 1mm in diameter would need to be added to the design. Each lattice cell would need a hole to the surface of the spacer, so that any trapped dust from the selective laser melting could be removed after the component was printed. There will also be the possibility that the holes would have a negative effect on the stiffness of the cavity so the spacer may need to be redesigned to ensure a sufficient magnitude of stiffness is still present within the spacer to keep the acceleration sensitivity to a minimum. In addition the spacer should be printed with some added length to each end of the spacer and without the support holes in the rim. This would allow for the spacer to have each end of the spacer flattened down, to ensure the faces are parallel and to have the support holes accurately drilled/machined in after, to account for any printing errors that could occur. Additionally, the tilt in the two ends of spacer and the length of the cavity should be accurately measured before attaching the mirrors.

As discussed at the end of Chapter 5, this type of cavity is designed to be utilised with a 461nm laser for the first stage of cooling Sr atoms within a Sr optical clock. For the final cavity mirrors with coatings for 461nm light will be attached to the lattice spacer.

7 Diamond-Diamond Cavity

Pure carbon has several allotropes, with the most common being graphite and diamond. Graphite is a soft, slippery material and is formed of individual layers, called graphene that are covalently bonded carbon atoms in a hexagonal shape. The layers are bonded together by weak van der Waals bonds which allows for the layers of graphene to easily slide over each other, giving graphite its soft characteristic. Whereas, diamond is an incredibily stiff material and is the hardest natural mineral, formed by giant carbon-carbon covalent structure, with the atoms arranged in a tetrahedral structure [52] as shown in Figure 71. This structure gives diamond its famous stiffness and makes the material excellent for cutting and polishing.

Figure 71: Diamond's tetrahedral structure, formed with carbon-carbon covalent bonds.

Naturally occurring diamond is most commonly formed approximately 100 miles below Earth's surface (in the upper mantle, under high-pressure and temperatures environments) but can be found closer to the surface, due to natural movements below the Earth's crust. (For example, a seismic event like a volcanic eruption brings diamond crystals towards the surface.) There are however, other places in which diamonds are thought to be formed including subduction zones (between moving tectonic plates) or within an asteroid crater, due to the mount of heat and pressure created by the strike.

Due to the rarity and price of mining diamonds, methods of creating lab based diamonds were developed and have become a lot more popular recently, especially for diamonds used in the industrial and for engineering applications. Synthetic diamond has been produced since as early as the 1950's under synthetic high temperature and high pressure environments and later on was also formed using chemical vapour deposition [52][53]. High pressure, high temperature (HPHT), uses the same conditions in which diamond is naturally formed but with an added catalyst or molten metal solvent to act to minimise the kinetic barrier. With this method most diamonds formed have a slightly yellow tinge in colour, due to the presence of nitrogen impurities,

commonly known as nitrogen vacancies. Whereas, chemical vapour deposition (CVD) on the other hand uses a gaseous source of plasma carbon and thermal dissociation of hydrogen at 2000°C, to create high quality, large, single, mono or poly-crystal diamonds.

These single crystal or polycrystalline diamonds that are produced using CVD are perfect to be used as optical components, not only due to diamond's high stiffness but also its low coefficient of thermal expansion. As seen in Figure 72, diamond at room temperature has a coefficient of thermal expansion as low as ≈ 1 ppm °C^{-1}, which with temperature starts to increase. But at lower temperatures and in particular at cryogenic temperatures, diamond starts to display a coefficient of thermal expansion close to zero.
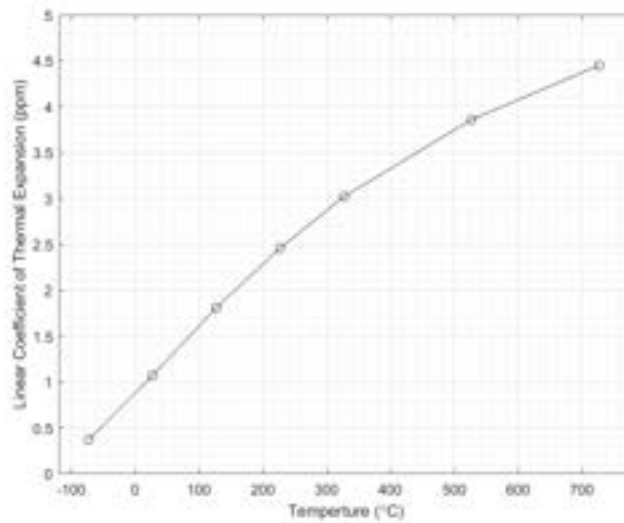
Figure 72: Diamond's coefficient of thermal expansion verses temperature (°C), data from [52]. The points are connected to guide the eye.

Another key property of diamond, making it a desirable material for optical components, is its unusually wide transparency window, which ranges from UV wavelengths starting at 226nm, all the way into the infra-red sprectrum, up to 500μm [54], which is much wider than typical materials used for optical components.

In relation to the research mentioned here, diamond's high stiffness is mostly utilised in the exploration and design of a diamond-diamond optical cavity, as smaller elements are needed for the cavity to display a very low overall deformation from the weight of the mirrors and spacer under gravity. This results in the diamond-diamond cavity weighing a minimal amount (approximately 5.6 grams) and in turn will have a much lower acceleration sensitivity of

$\approx 4 \times 10^{-12}$ averaged from each direction or as low as $\approx 8 \times 10^{-15}$, when horizontally mounted.

7.1   Vertical Cavity designs

Due to time limitations and cost of forming larger single or polycrystalline crystals of diamond using CVD, small sized optical mirrors and spacer are explored in creating the diamond cavity. As a result an optical cavity with an uncommonly thin spacer was designed and developed. The initial diamond cavity design is shown in Figure 73 and 74. The diamond spacer was developed to be only a couple of millimetres thick and a handful of centimetres in diameter, which compared to other common and novel cavity designs [10][11][55][7][36][8] is incredibly thin.

The initial vertical diamond cavity was designed to be mounted by precisely placing it on a single Viton circular ring, ensuring that the cavity is evenly planar on the ring mount as shown in Figure 73. Both the mirrors and spacer will be diamond and are designed to be optically contacted together.
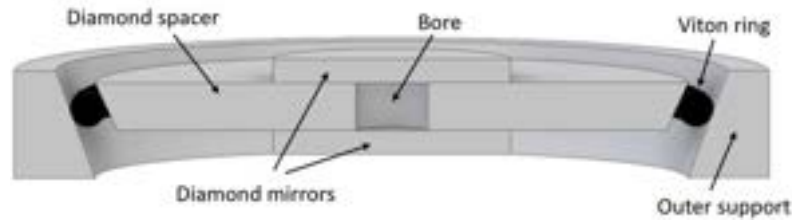
Figure 73: A model of the vertical, circular single bevel diamond cavity and how it would be supported using a viton ring.

For the initial simulations the bevel cut was used as the support and the standard diamond material provided in ANSYS was used, with the properties displayed in Table 6 (displayed in Chapter 7.1.1). With the dimensions displayed in Figure 74, for the initial simulations the following were used: $s_L = 2$mm, $m_d = 10$mm, $m_L = 1$mm, $b = 3$mm and $\alpha = 45°$ under 1g ($g = 9.81$ms^{-2}), which gave fractional length change between the centre of the two mirrors of 3.79×10^{-11}/g.
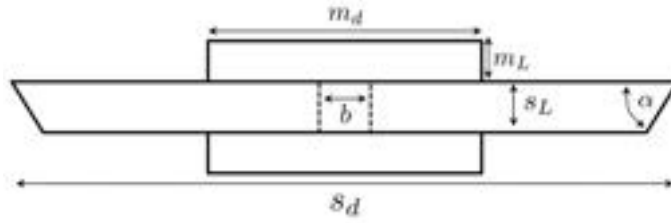
Figure 74: Diagram of the side view of vertical, circular single bevel diamond cavity design with geometric dimensions.

The first steps in optimising the geometry were to see if firstly, altering the outer shape from a circle, to different polygon shapes, could further reduce the acceleration sensitivity, while also investigating how the angle of the bevel cut, α affects the acceleration sensitivity of the cavity, as discussed below.

7.1.1   Different vertical Spacer shapes

The outer shape of the spacer was altered to see the effect on the acceleration sensitivity under gravity, 1g (9.81ms^{-2}). The original circular design was compared to a triangular, square and a hexagon design. The size of the spacer was compared against the angle of the bevel, α, with the dimensions: $s_L = 2$mm, , $m_d = 10$mm, $m_L = 1$mm and $b = 3$mm kept the same.

Length of upper spacer face sides (mm)	Area of upper spacer face (mm^2)	Vertical cavity shapes (bottom view)	Vertical cavity shapes (side angle view)
25 (diameter)	490.9		
33.7	491.8		
22.1	488.4		
15.1	592.4		

Figure 75: Vertical cavity designs and their corresponding dimensions.

The size of each spacer was kept similar, by comparing the area of upper spacer side and having these areas all within a few mm^2 of each other. The areas of the designs for each shape are shown in Figure 75, along with the CAD designs. For the non circular designs it was assumed that strips of Viton would be placed under each bevel cut side, along the entire length.

Table 6: Diamond Material Properties used for ANSYS (the material properties are used from the material library in ANSYS as discussed in Appendix B).

	Diamond
Density	3510kgm^{-3}
Coefficient of thermal expansion	$1.18 \times 10^{-6} C^{-1}$
Young's Modulus	1140GPa
Poisson's Ratio	0.2

All four designs were tested with the spacer and both mirrors as diamond, with the properties shown in Table 6. Each placed as vertical cavities under 1g ($g = 9.81$ms^{-2}) with the bevel cut as

the support. The bevel cut angle, α is varied between $45 - 85°$ and the fractional length change is compared. As seen in Figure 76 all four shapes follow the same relationship, that by increasing the bevel cut angle, α the fractional length change between the mirrors is reduced, showing a reduction in the acceleration sensitivity.

Figure 76: The acceleration sensitivity (fractional length change $\Delta L/L$) under 1g of vertical acceleration versus bevel cut angle, α of vertical diamond spacers of different shapes, with $s_L = 2$mm, $m_d = 10$mm, $m_L = 1$mm and $b = 3$mm. The points are connected to guide the eye, with the error bars not visible on this scale. Data from simulations computed on ANSYS.

There are slight differences between each shape, as the lower α is, the more difference in the $\Delta L/L$ between the shapes, as the hexagon appears to display more axial displacement in the cavity. Yet as bevel cut angle, α is increased the difference between the shapes becomes less obvious. Of course these minimal variations could be due to the spacers of each shape having minor changes in the volumes. It is noted that the hexagon spacer does have the largest area of the upper spacer face and this could be the reason for the larger fractional length change. Overall, it is observed that the larger the bevel cut angle, α, the less the axial displacement between the centre of the two mirrors. However, by increasing α too much towards 90°, this could cause issues with mounting the cavity as the friction between the Viton and diamond would have to be enough to ensure the cavity stays in place. Therefore, any angle over approximately 75° would be unsuitable to use, resulting in the lowest fractional length change this cavity would display being $\approx 1.5 \times 10^{-11}$/g, which would produce a considerably stable cavity. It is worth

noting that no other optimization was explored in the vertical cavity design. As a result this is not a final acceleration sensitivity number and could be further reduced by optimising the mirror length, mirror diameter, spacer length, spacer diameter and bore diameter. In this case, the design was adapted to be come a 3D cavity as discussed in the next subchapter.

7.2 Circular Double Bevel Design

The initial vertical design was next adapted to allow for the cavity to be mounted and/or rotated in any direction, by adding another bevel cut opposite to the original, evolving the design to a circular double bevel shape, as displayed in Figure 77. In this case two Viton rings would be used, by placing them on each bevel and applying a compressive force on to them.
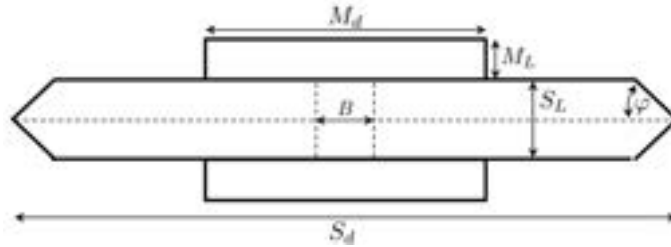
Figure 77: Diagram of the side view of circular double bevel design, for the diamond-diamond cavity with geometric dimensions.

Other shapes, for example a triangle and square were explored with the double bevel shape, but as these were found to have similar results to the circular shape, it was decided to go ahead with the circular shape, as this design would be simpler to mount, due to singular Viton o-ring being used instead of multiple strips of Viton. Also as diamond is a brittle material having it polished into shape with multiple corners would become a cause for concern.

7.2.1 Initial Geometry Simulations

To begin with parameters were initially altered and tested to see their effect on the fractional length change, $\Delta L/L$ of the diamond spacer. The mirror length, M_L and spacer length, S_L were found to have minimal difference on improving the fractional length change. Whereas, the mirror diameter, M_d, spacer diameter, S_d, bore diameter, B and angle of the bevel cut, φ had significant effects on the fraction length change. All initial simulations were ran with equal compressive forces (1N) applied to both bevel cuts parallel to the optical axis, with the outer corner connecting the two bevel cuts being used as the support.

By increasing the mirror length the fractional length change slightly decreased but overall had little impact, so the mirror length of 1mm was chosen. This was a little different to the spacer length as by decreasing the spacer length the fractional length change was marginally decreased, but overall had a minimal effect on the acceleration sensitivity. Therefore, for ease of mounting the cavity a spacer length of 2mm was selected.

The effect of changing the mirror diameter had an appealing result on the fractional length change, as by increasing the mirror diameter the fractional length change greatly decreases, until a certain value where it levels off. The relationship is shown in Figure 78a, where at ≈ 13mm the graph levels off and then even slightly increases, showing that mirror diameter has a notable effect on improving the acceleration stability of the cavity. It was additionally found, that by changing the angle of the bevel cut, φ the fractional length change crosses zero at around $\approx 60 - 62°$ (depending on the parameters of the cavity selected, within the range of values investigated) and a similar relationship is noticed in the zero crossing gradient when the mirror diameter is changed, as when the mirror diameter is firstly increased the zero crossing gradient sharply decreases until ≈ 13mm again where it levels off as shown in Figure 78b. Within the same range, the angle, φ where the fractional length change crosses zero stays reasonably constant at $61°$, as the mirror diameter is increased. As a result of these findings a mirror diameter of 13mm was chosen.

(a)   (b)

Figure 78: (a) the acceleration sensitivity (fractional length change $\Delta L/L$) under 1g of vertical acceleration in each orthogonal direction averaged versus the mirror diameter, M_d and (b) the zero crossing gradient of the acceleration sensitivity versus the mirror diameter, M_d for the diamond-diamond cavity. The points are connected to guide the eye, with the error bars not visible on this scale. Data from simulations computed on ANSYS.

For the spacer diameter, a range of values was tested, from 25mm to 30mm. Smaller than 25mm would cause difficulties in the supporting and assembly of the cavity and the upper limit was kept at 30mm to keep the cost of the spacer to a minimum. From this only angles $56 - 66°$ were explored to allow for the pattern around the zero crossing to be visible as shown in Figure 79. As seen for each spacer diameter within the range investigated there is a zero crossing, as shown by the white section where the fractional length change is, $9.9 \times 10^{-13}/\text{g} > \Delta L/L > -9.9 \times 10^{-13}/\text{g}$.
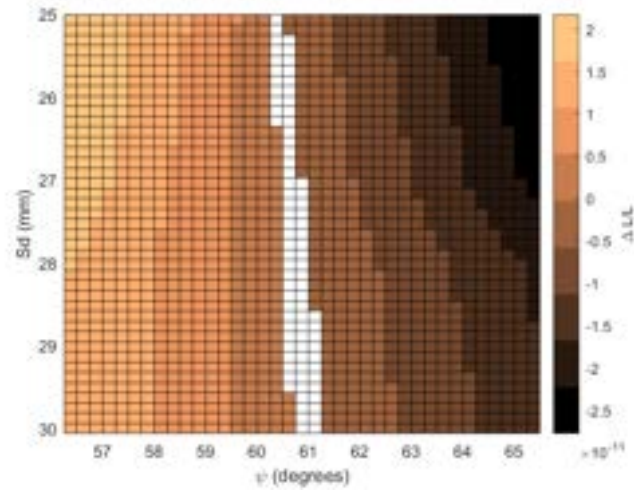
Figure 79: The acceleration sensitivity (fractional length change $\Delta L/L$) under 1g of vertical acceleration in each orthogonal direction averaged for the diamond-diamond cavity, versus both the spacer diameter, S_d and the angle of the bevels ψ. Data from simulations computed on ANSYS.

At the larger mirror diameters the gradient of the fractional length change is moderately decreased as represented by the increase in the horizontal white squares in Figure 79. This relationship is later displayed in Figure 80a, where the zero crossing gradient versus the spacer diameter is plotted, showing the gradient appears to linearly decrease as the spacer diameter increases.

The zero crossing angle at each spacer diameter was also explored, as if the angle is too large or small this could cause issues with mounting the cavity. As seen in Figure 80b, the zero crossing angle is very consistent and only slightly increases by $\approx 0.6°$ within the range of spacer diameters explored. As a result of these investigations 30mm was selected as the spacer diameter.

(a)   (b)
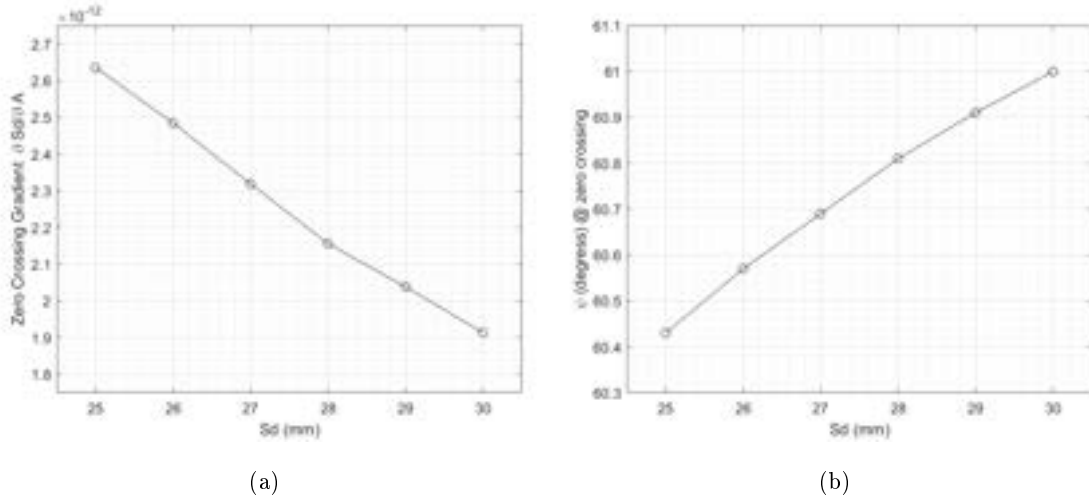
Figure 80: For the diamond-diamond cavity, (a) the gradient of the zero crossing for the acceleration sensitivity (fractional length change $\Delta L/L$) under 1g of vertical acceleration in each orthogonal direction averaged versus the spacer diameter, S_d and (b) the angle in which the zero crossing occurs. The points are connected to guide the eye, with the error bars not visible on this scale. Data from simulations computed on ANSYS.

The last initial dimension which was investigated was the bore diameter. To ensure 99.99% of the beam lay within the bore diameter and for ease of aligning the beam through the bore, the smallest bore diameter which was investigated was 3mm. The bore was then increased to 6mm every millimetre and the acceleration sensitivity was observed. As seen in Figure 81 the fractional length change slowly increases as the bore diameter is increased. Therefore, the smaller the bore diameter the smaller the acceleration sensitivity, leading to 3mm being determined to be the bore diameter.
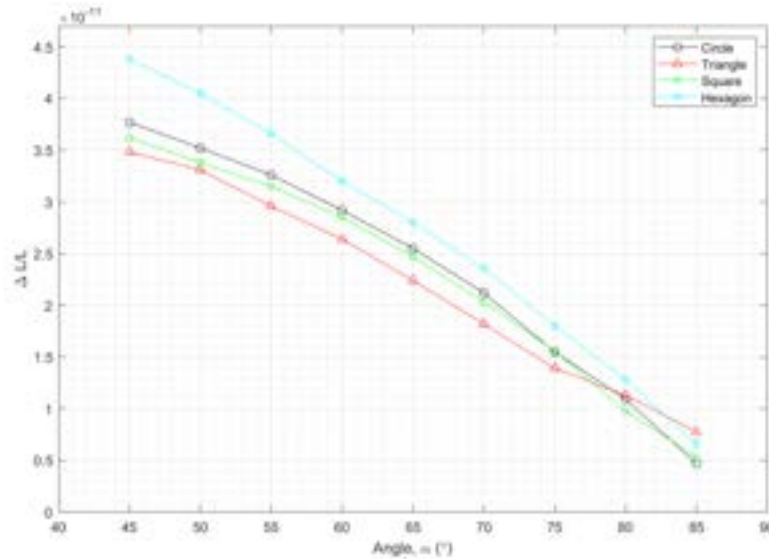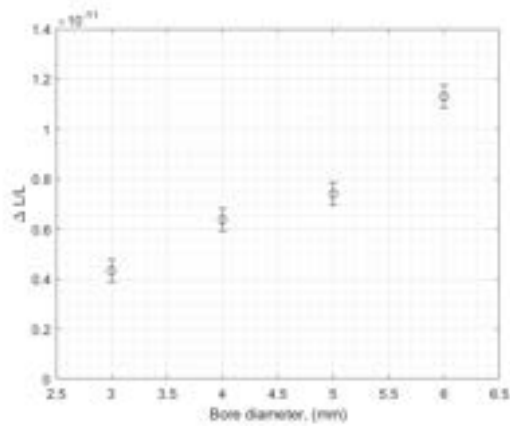
Figure 81: The acceleration sensitivity (fractional length change $\Delta L/L$) under 1g of vertical acceleration for the diamond-diamond cavity in each orthogonal direction averaged versus bore diameter, B (mm). (With all fractional length changes being made positive before averaging.) Data from simulations computed on ANSYS.

7.2.2 Finding the Optimal Bevel Angle, φ

Once the sizes of the mirrors and spacer were selected, the last dimension to be determined, was the angle of the symmetrical bevels, φ. Initially, the angle was varied every degree between 56 and 66 degrees. It was found that as the angle φ is slowly increased the fractional length change decreases and at approximately 61° crosses zero as shown in Figure 82.
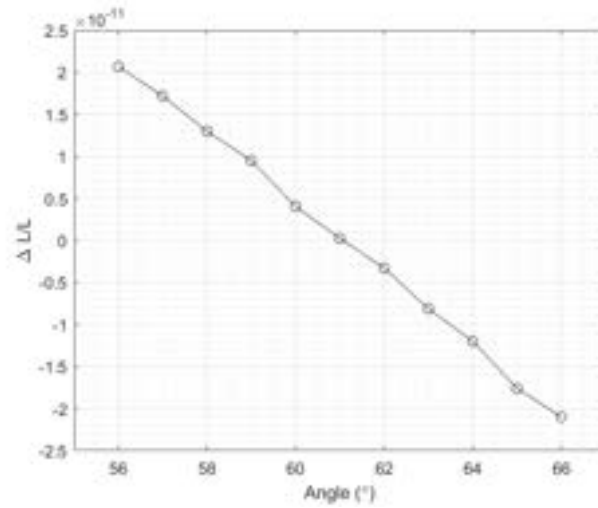
Figure 82: The acceleration sensitivity (fractional length change $\Delta L/L$) under 1g of vertical acceleration in each orthogonal direction averaged versus for the diamond-diamond cavity versus angle (°), of symmetrical bevels between 56-66°. The points are connected to guide the eye, with the error bars approximately equal in size to the "o" markers at each point. Data from simulations computed on ANSYS.

Next, a closer look of where φ crosses zero was explored to the nearest 0.2°. As seen in Figure 83 the fractional length change crosses zero at approximately 61°. However the results do not produce a smooth graph and has large error bars, resulting in a finer mesh needed to improve the accuracy of the results, but due to the errors on polishing the diamond to the nearest 0.2° this is not necessary.
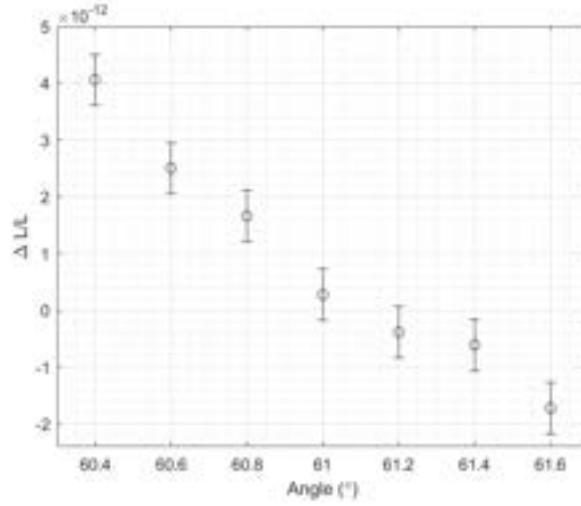
Figure 83: The acceleration sensitivity (fractional length change $\Delta L/L$) under 1g of vertical acceleration in each orthogonal direction averaged for the diamond-diamond cavity versus angle, ° of symmetrical bevels between 60.6-61.4°, every 0.2°'s. Data from simulations computed on ANSYS.

Therefore, the final dimensions for the simulated double bevel circular diamond cavity can be found in Table 7, with the range of the values investigated. M_L and S_L were kept constant at 1mm and 2mm respectively after initial simulations displayed that they had a minimal effect on the acceleration sensitivity. For later designs of this type of cavity it would be interesting to investigate increasing the spacer diameter, S_d to values larger than 30mm to see if this could further reduce the acceleration sensitivity in the cavity. With these final values the fractional length change, under 1g $(9.81ms^{-2})$ in each direction was found and is displayed in Table 8.

Table 7: Outline of parameters investigated of the diamond-diamond cavity and final parameters that where selected.

Parameter	Range investigated	Final value
M_L	-	1mm
M_d	6-17mm	13mm
S_L	-	2mm
S_d	25-30mm	30mm
B	3-6mm	3mm
ψ	$35 - 66°$	$61°$

As the results show in Table 8 when the cavity is mounted vertically (where 1g is applied in the

119

y-direction) this causes a larger displacement between the mirrors, than when the cavity is horizontally mounted. As the cavity bends under the weight of the spacer and the two mirrors, as shown in the displacement contour in Figure 84a. However, the cavity bends reasonably evenly between the two mirrors so the axial displacement in the centre of the two mirrors still produces a low acceleration sensitivity when the cavity is mounted in this way.
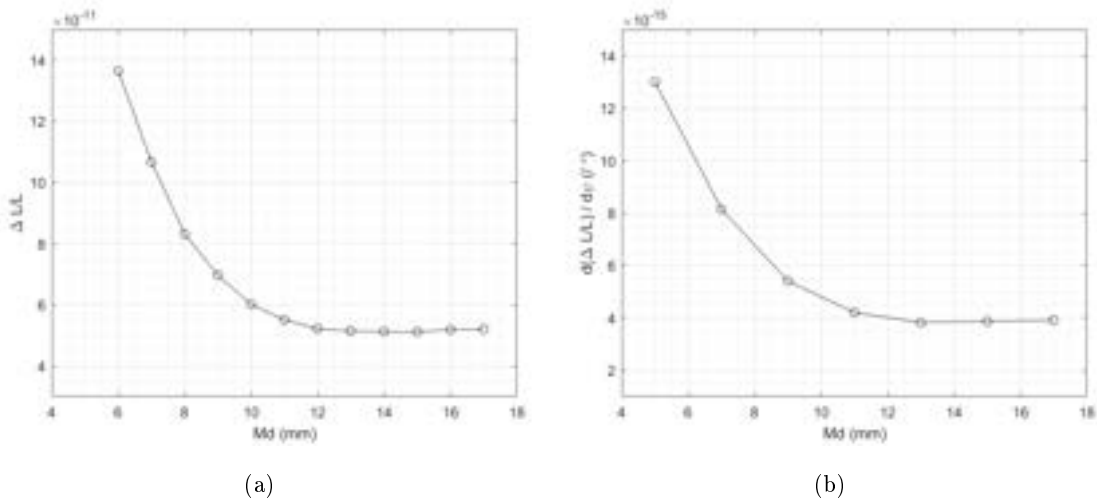
Table 8: Numerical values for the acceleration sensitivity (fractional length change $\Delta L/L$) when 1g of vertical acceleration is applied in each orthogonal axes for the diamond-diamond cavity.

X	Y	Z	$\Delta L/L$
1g	0	0	$-7.63 \times 10^{-14}/\text{g}$
-1g	0	0	$7.12 \times 10^{-14}/\text{g}$
0	1g	0	$-1.51 \times 10^{-11}/\text{g}$
0	-1g	0	$1.45 \times 10^{-11}/\text{g}$
0	0	1g	$-5.34 \times 10^{-13}/\text{g}$
0	0	-1g	$5.97 \times 10^{-13}/\text{g}$

But when the diamond cavity is mounted horizontally (where 1g is applied in the x or z direction), this significantly reduces the acceleration sensitivity even further. As it was found that the fractional length change could be as low as $7.63 \times 10^{-15}/\text{g}$ when the cavity is mounted in the x-direction, as shown in Table 8. This minuscule length change between the centre of the two mirrors is displayed also in the displacement contour in Figure 84b. It shows that when vertical acceleration is applied to the cavity it causes no notable bending in the mirrors and the displacement is most around where the 1N force is applied, where the cavity would be mounted. It is expected that the results for both orthogonal directions x and z to have identical results as the cavity is perfectly symmetrical, similarly both values for the y orthogonal axis, however when the geometry is meshed within ANSYS this creates an unsymmetrical mesh, as it is not possible to have a mesh with infinite meshing cells. For the simulation results within this chapter the student home version ANSYS R1 and R2 was utilised, which does not have the highest meshing options available, so small errors in the results are expected, especially when values to the 10^{-15} are being calculated. A full discuss on the versions of ANSYS used can be found in Appendix B.
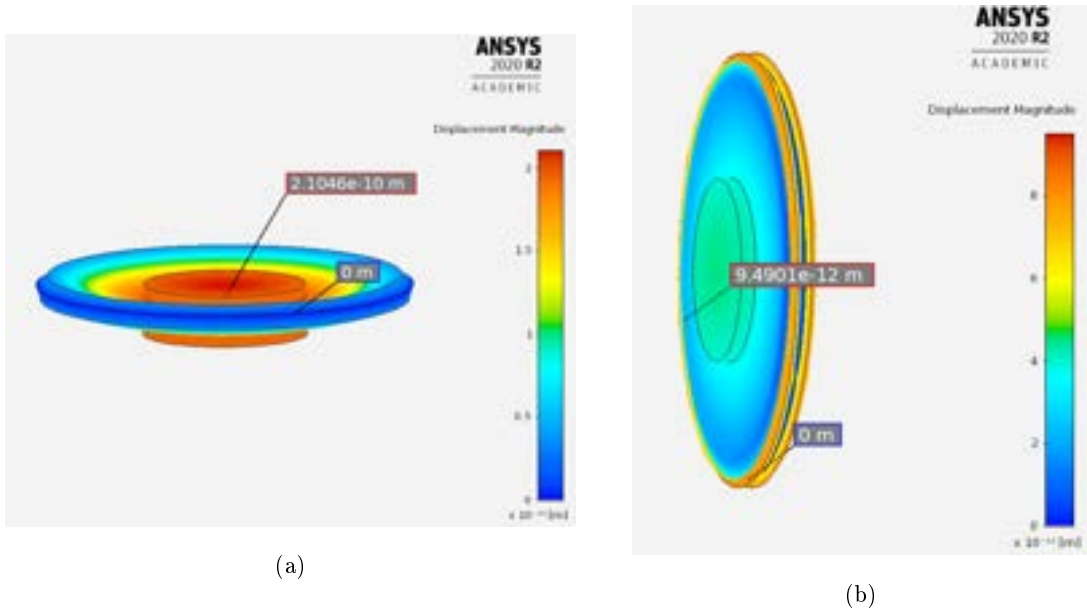
Figure 84: Displacement contour diagrams displaying the effect of vertical acceleration under 1g of acceleration on the diamond-diamond cavity when (a) vertically and (b) horizontally mounted, using the dimensions specified in Table 7, with the scale on the right-side of each figure.

Therefore, this type of design for an optical cavity has the potential to have a remarkable stability when horizontally mounted but also its a reasonably stable cavity in all mounting directions. However, the stability of the cavity will also largely depend on the environmental temperatures it operates in. If the cavity was placed under cryogenic temperatures (where diamond displays its lowest CTE at nearly zero), then the cavity length would be almost unaffected by thermal effects. Whereas, if the cavity was used at room temperature the stability of the cavity would only last for a short period of time, making the cavity only applicable for systems, that require stability for these short time periods, such as quantum enabled radar.

Due to the diamond-diamond cavity short length of 2mm the cavity will have a large free spectral range of $74.9{\times}10^9$Hz, resulting in the cavity needing to be used along side a frequency comb, in order for the cavity to be utilised within quantum technologies. Following this and assuming the mirrors for the cavity have equal reflectance's of 99.99%, the diamond-diamond cavity with display a finesse of $3.1{\times}10^4$ and a linewidth of $2.4{\times}10^6$Hz.

For the mirrors for the diamond-diamond cavity, one planar and one concave mirror will be utilised to create a hemispherical shaped cavity. As one mirror is planar this will make the cavity exceptionally robust to misalignment. As discussed in Section 2.5 for a cavity to sit within the

stability condition,

$$0 \leq g_1 g_2 \leq 1. \tag{49}$$

As the first mirror is planar, g_1 is equal to one. However, for the second mirror a where a suitable a radius of curvature of 100mm is used for the concave shape, this would make g_2 equal to 0.98, making $g_1 g_2 = 0.98$. As the cavity is only 2mm in length this results in the diamond-diamond cavity being located close to the upper end of the stability condition. It is worth noting that to be able to manufacture a diamond mirror with a radius of curvature of 100mm it may result in the mirrors for the cavity needing to be slightly longer than 1mm thick.

7.3 Diamond-ULE Cavity, CTE tuning

As mentioned earlier in this chapter, a way to reduce the thermal expansion sensititviy would be to cool the diamond cavity down to cryogenic temperatures, where diamond exhibits a lower coeffeient of thermal expansion, close to zero. However, another method was explored to minimise the thermal expansion sensitivity, similar to [27], where ULE rings are introduced to allow the cavity to have a zero crossing in the coefficient of thermal expansion at more manageable temperatures.

In [27] they look at typical types of cavity design with ultra-low expansion glass (ULE) used for the cylinder shaped spacer with fused silica (FS) mirrors. They investigate pushing the zero crossing in the cavities' CTE closer to room temperature, by optically contacting ULE rings to the backs of fused silica mirrors. Through this method they demonstrate that the zero crossing of a ULE/FS cavity can be modified over a range of more than 30°C, with room temperature within this range.

Here a comparable idea was considered, where four ULE rings were incorporated with the diamond mirrors and spacer. Two ULE rings were placed on each side of the diamond spacer, with the first pair (inner ULE rings) attached between the diamond spacer and the outer ULE rings. The diamond mirrors are then attached on the inner surface of the outer ULE rings as shown in Figure 85, with all surfaces optically contacted together.
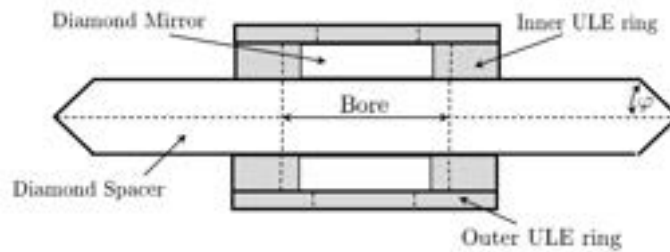
Figure 85: Diagram of the side view of diamond cavity with four optically contacted ULE rings (as demonstrated by the grey colour).

All dimensions of the diamond-ULE cavity are shown in Figure 87, with the ranges explored shown in Table 9. It was found that the zero crossing in the cavity's CTE could be found at $\approx 40 - 70°$C. But by introducing ULE which has a much lower stiffness compared to diamond, this has a large effect on the acceleration sensitivity of the cavity, as when the cavity is mounted horizontally, this causes the two ULE rings on each side of the spacer to significantly axially bend as shown in Figure 86b. This results in the fractional length between the centre of the two mirrors to be largely increased.

However, when the cavity is mounted vertically it bends in a similar way to the diamond-diamond cavity and produces similar results. The only difference is the outer ULE rings slightly bend under the weight of the diamond mirrors as shown in Figure 86a, which in general increases the fractional length between the mirrors by $\approx 25 - 40\%$, when compared to the diamond-diamond acceleration sensitivity results when the cavity is vertically mounted.
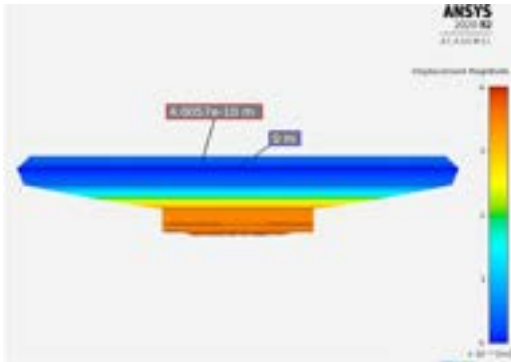
(a)
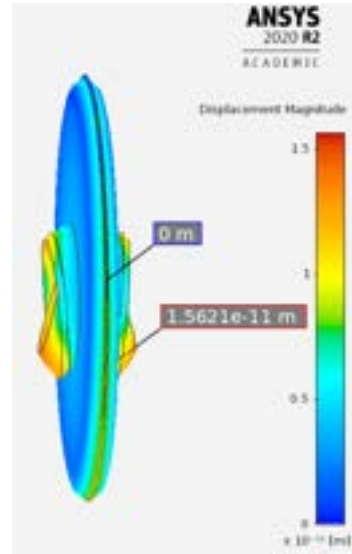
(b)

Figure 86: Displacement contour diagrams displaying the effect of vertical acceleration under 1g of acceleration on the diamond-diamond cavity with the four ULE rings incorporated when (a) vertically and (b) horizontally mounted, with the scale on the right-side of each figure.

The full dimensions of the diamond-ULE cavity can be seen in Figure 87. The outer diameter of the outer ULE ring and inner ULE ring were varied at the same values, along with the spacer bore diameter and inner ULE ring diameter also varied at the same values. To be able to make a direct comparison in the acceleration sensitivity between the diamond-diamond and diamond-ULE, similar dimensions were kept. Both the spacer diameter, S_d and spacer length S_L were kept at 30mm and 2mm respectively. Also the mirror length, M_L was kept at 1mm and the angle of the bevel was kept at $\approx 61°$ but varied slightly by a few degrees for optimization where needed.
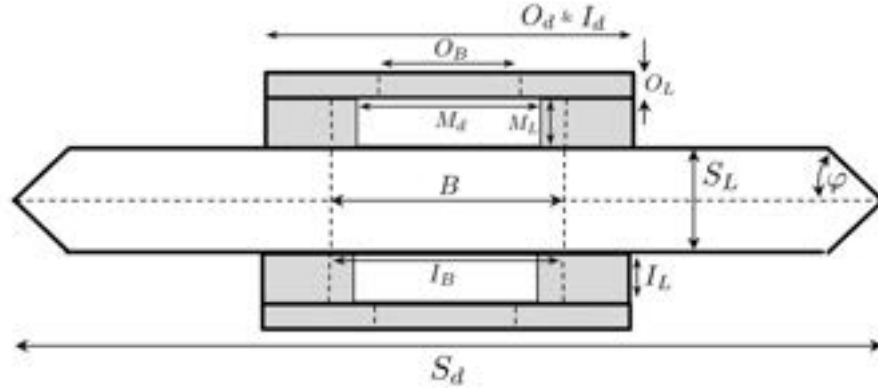
Figure 87: Diagram of the side view of circular double bevel diamond cavity design with four added ULE rings (as demonstrated by the grey colour), with added geometric dimensions.

All dimensions which were varied are displayed in Table 9, with the range explored. Initially the inner and outer ULE ring lengths (I_L and O_L) were varied between 0.25mm and 1.25mm each but it was found that when $I_L = 1$mm and $O_L = 0.5$mm it gave the most promising results.
The final stages of optimising the geometry involved three tests. The first was keeping the mirror diameter, M_d, outer bore, O_B, inner bore, I_B and bore, B constant at the lowest ranges explored, as displayed in Table 9. Then the outer diameter of both ULE rings was increased from 9mm to 15mm by single millimetres at a time. The second test was similar to the first but the outer diameter of the ULE were kept constant at 15mm and all bore values as well as the mirror diameter were increased through their full ranges. Lastly, all parameters mentioned in Table 9 were increased together from their lowest values to their highest, one millimetre at a time. The last method provided the most consistent and favourable results. It was found that the fractional length between the mirrors could be as low as the results shown in Table 10, when 1g ($9.81ms^{-2}$) is applied in each direction. The final dimensions are shown in Table 9.

Table 9: Outline of parameters investigated for the diamond-ULE cavity, with $S_L = 2$mm, $S_d = 30$mm, $M_L = 1$mm, $I_L = 1$mm and $O_L = 0.5$mm kept constant.

Parameter	Range investigated	Final value
M_d	$5 - 11$mm	$7mm$
I_B & B	$6 - 12$mm	$8mm$
O_B	$4 - 10$mm	$5m$
O_d & I_d	$9 - 15$mm	$12mm$
ψ	$55 - 65°$	$60°$

125

As seen when the cavity is vertically mounted this gave just slightly larger but similar values when compared to the diamond-diamond design. However, when the cavity is mounted horizontally this considerably increased the amount that the cavity axially bends under 1g. Despite this, the average fractional length change when the cavity was mounted horizontally was found to be as low as 1.56×10^{-11} and the overall average for all directions was 1.59×10^{-11}.

Table 10: Numerical values for the acceleration sensitivity (fractional length change $\Delta L/L$) when 1g of vertical acceleration is applied in each orthogonal axes for the diamond-ULE cavity.

X	Y	Z	$\Delta L/L$
1g	0	0	$1.72 \times 10^{-11}/$g
-1g	0	0	$-2.05 \times 10^{-11}/$g
0	1g	0	$1.53 \times 10^{-11}/$g
0	-1g	0	$-1.80 \times 10^{-11}/$g
0	0	1g	$-1.38 \times 10^{-11}/$g
0	0	-1g	$1.07 \times 10^{-11}/$g

Next for the final dimensions of the diamond-ULE cavity the length changes related to thermal adjustments were calculated. The CTE of ULE was approximated about its zero crossing temperature, t_0 with:

$$\alpha_{ULE}(t) = a(t - t_0) + b(t - t_0)^2. \tag{50}$$

Where α represents the coefficient of thermal expansion, with a as the linear temperature coefficient and b as the quadratic coefficient. Here it was assumed that $a = 1.8 \times 10^{-9}/°\mathrm{C}^2$, $b = -1 \times 10^{-11}/°\mathrm{C}^3$ and $t_0 = 22°\mathrm{C}$ [27]. The CTE of diamond was assumed to be constant at $1 \times 10^{-6}/°\mathrm{C}$ for the range of temperatures explored.

As seen in Figure 88 the diamond-ULE cavity exhibits a zero crossing temperature of $\approx 75°\mathrm{C}$, which is quite notably higher than room temperature. Nevertheless, working with a CTE which is higher than room temperature is more practicable than cooling the cavity down to cryogenic temperatures.
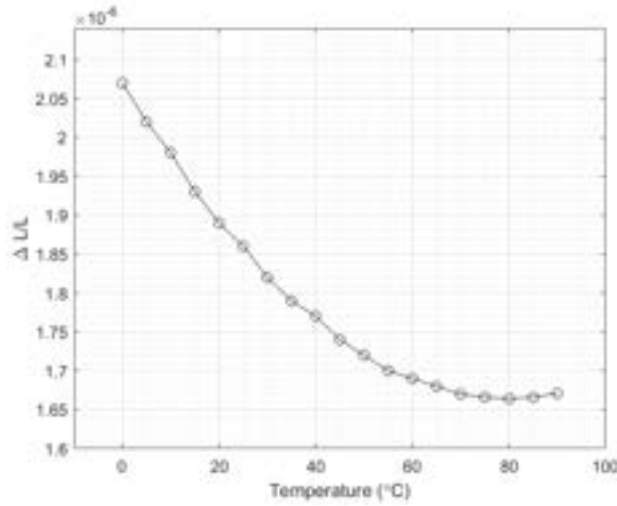
Figure 88: The thermal sensitivity (fractional length change, $\Delta L/L$ between the centre of the two diamond mirrors) for the diamond-ULE cavity with respect to temperature (°C). The points are connected to guide the eye, with the error bars not visible on this scale. Data from simulations computed on ANSYS.

7.4 Packing the Cavity in a Vacuum

There are a couple of other methods in which the sensitivity of the diamond-diamond cavity could be further minimised. The first is by removing any air or particles from the bore of the cavity, as any particles that are present in the bore of a cavity will cause a small proportion of the light to be scattered off the particles. The amount of light that would be scattered depends on the refractive index of the bore versus the wavelength of the light. For example blue light will experience more Rayleigh scattering in air, due to the ratio between the wavelength of blue light versus the size of air particles, resulting in a larger amount of loss in power in the light per round-trip in the cavity. There will also always be a certain amount of uncertainty that will be present if air and other particles are present in the bore. As any change in temperature and due to the random movements of particles the density of the bore and will not stay consistent throughout the bore, which will consequently mean that the refractive index will not stay constant in the bore. However, by moving the particles this would increase the finesse of the cavity as less power would be lost per "round-trip" in the cavity.

Commonly particles are extracted from the bore by adding a hole in the spacer of the cavity, connecting the bore to the outside of the cavity, resulting in when the cavity is placed under vacuum the bore would also be under the same vacuum pressure similar to [4]. Another method

which is more complicated is to assemble the cavity under vacuum. Due to the size of the diamond-diamond spacer, it would not be possible to add a hole into the bore, resulting in only the latter option being feasible.

One particular benefit on making the bore under a high vacuum pressure is that if the cavity was then placed under cryogenic temperatures, then there would be no concern about any water vapour condensing on the inner surface of the bore, which leads to the next method in which the sensitivity of the diamond-diamond cavity could also be reduced. By cooling the cavity down to cryogenic temperatures this would decrease the thermal expansion sensitivity, as at these temperatures diamond displays a coefficient of thermal expansion close to zero, as previously discussed in this chapter.

Another benefit of having the diamond cavity within a vacuum chamber is that the temperature stability of the cavity would be improved, as the vacuum would remove any conduction from the air that would act as a heat transfer mechanism.

7.5 The Next Steps

During stages of contacting relevant companies that specialise in making optical components from diamond, it was discovered that the material properties for diamond vary slightly between natural diamond and synthetic diamond. In addition, different sources tended to quote different values for some important properties of diamond, including the density, Young's modulus and the Poisson ratio. For example, [56] quotes diamonds Poisson ratio to be 0.2, while [52] quotes 0.1, and [61] states it as 0.0791 if the diamond has fracture planes along {111} (a more detailed discussion on diamond's Poisson ratio and its fracture planes can be found in Chapter 8). Therefore, some simulations where completed to see the effect of these different values for the material properties had on the acceleration sensitivity of the cavity and on the angle in which the zero crossing in the acceleration sensitivity occurs. The slight variations in the density and Young's modulus appeared to have minimal effect on the acceleration sensitivity. Whereas, the Poisson ratio had a significant effect. Initially for all simulations 0.2 was used for the Poisson ratio due to this being the auto value that ANSYS provides for diamond, but when 0.1 was used (which is the value quoted by the company Diamond Materials [59]) this reduces the zero crossing angle by approximately 25 degrees. This significant change prompted the need for extra research to be completed in order to find a more accurate value for the Poisson ratio, this research is discussed in detail in Chapter 8.1. As the Poisson ratio finally used is 0.075 (value selected is discussed in Chapter 8.1) for the CVD diamond, compared to the 0.2 that was used for this entire chapter, then the values found in this chapter are found to be off by an approximate systematic error, resulting in the overall

relationships found in each sub-chapter, (for when the geometry of the cavity is varied) are found to be almost identical to when 0.075 is used but the actual values found are off by a systematic error for each instance.

Therefore, the next steps that were taken was to find the new optimum angle for the bevel cuts, using 0.075 as the Poisson ratio for the CVD diamond. Also due to time constraints the decision was made to use easily available FS mirrors, compared to using diamond mirrors. As for the diamond mirrors the material would need to be cut and polished, and then sent to a different company to have mirror coatings with high reflectivity added to the diamond substrate. A full description of the next stages in designing and building the diamond can be found in Chapter 8 next.

8   Diamond-FS Cavity

As discussed in the previous chapter, due to time constraints, it was not possible to continue with the diamond-diamond cavity, as the added extra time to get the mirror coatings applied to the diamond mirrors would result in there not being enough time to fully assemble and test the cavity. Therefore, instead for proof of principle, fused silica mirrors were explored with the diamond spacer, to create a diamond-FS cavity.

For the diamond-FS cavity, there were a number of values which needed to be found or calculated, starting with the Poisson ratio of diamond, as it was found that many different sources quoted slightly different values for not only the Poisson ratio for diamond but also for the density and Young's modulus. However, unlike the density and Young's modulus, the Poisson ratio was found to have a large effect on the simulation results. Therefore, an accurate and reliable value for the Poisson ratio needed to be found, by taking into account a number of properties of diamond that could affect the Poisson ratio of the material including the fracture plane and how the diamond is formed. Next the optimum geometric values for the diamond spacer were calculated with taking into consideration that an added face was needed to be added to minimise any cracks that could occur in the diamond during the cutting and polishing stages. Lastly in this chapter is a discussion on the size of FS-mirrors that could be used for this type of cavity and which mirror coatings would benefit this thin cavity.

8.1   Poisson's Ratio of CVD diamond

Poisson's ratio, ν is a measure of the Poisson effect that each material experiences under a loading force. The Poisson effect occurs when a force is applied to a material causing the material to deform perpendicular to the direction of the force and the amount in which the material deforms is quantified by the material's Poisson's ratio. For most materials the Poisson ratio is approximately between -1.0 and 0.5 (to allow for the material to have a positive Young's modulus, shear modulus and bulk modulus, which is required for stable, isotropic and linear materials [57]). Softer materials tend to have a Poisson ratio that sits closer to 0.5, for example natural rubber has a Poisson ratio of 0.499 [58], as it exhibits a large expansion when it is compressed. For more solid, easily fractured materials, the Poisson ratio tends to be closer to zero.

As the Poisson's ratio is a ratio of transverse strain to the axial strain, it can be estimated using:

$$\nu = -\frac{\varepsilon_2}{\varepsilon_1} \tag{51}$$

assuming the material is only being compressed or stretched along one direction. With ε_2 as the transverse strain, which when positive would reflect axial compression and when negative axial

tension. Then ε_1 is the axial strain, which would be positive for axial tension and negative for axial compression. Of course, this equation is just a base estimate of the Poisson's ratio of materials and does not take in account the relative changes in the volume of an entire material. For some materials it can be quite difficult to calculate the Poisson's ratio, for example for materials with crystal structures as the Poisson's ratio depends on the fracture planes that are present in the structure [60] (with a full discussion on fracture planes found below in Chapter 8.1.1). This is the same for diamond. As a result for diamond, its Poisson ratio is quoted to be a variety of values, for example, [56] quotes diamonds Poisson ratio to be 0.2, while both synthetic diamond companies Element Six [52] and Diamond Materials [59] quote the poisson ratio to be 0.1, whereas in both [62] and [63] quote the Poisson ratio to be 0.0781 as an ultrasonically measured value.

When the Poisson ratio of the diamond spacer was varied within simulations ran in ANSYS, it was found that the optimum angle of the bevels (where the acceleration sensitivity of the cavity crosses zero) was largely affected by the value of the Poisson ratio. As seen in Figure 89, the optimum bevels angle approximately increases by two degrees as the Poisson ratio is increased by 0.1. Therefore an accurate and reliable value for diamond's Poisson ratio was needed to be selected.
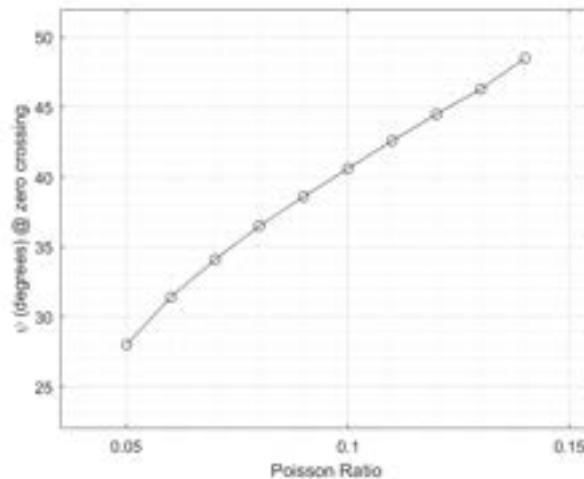
Figure 89: Zero crossing angle in the acceleration sensitivity (fractional length change $\Delta L/L$) under 1g of vertical acceleration in each orthogonal direction averaged for a diamond cavity versus the Poisson's ratio of the diamond, with a density of 3515 kgm^{-3} and Young's modulus of 1050 GPa. The points are connected to guide the eye, with the error bars not visible on this scale. Data from simulations computed on ANSYS.

As stated earlier the Poisson ratio of diamond depends on which fracture planes are present in the

crystals structure, and for CVD diamond (the type of diamond which will be used for the diamond spacer) normally fracture planes along {111} are present with occasionally {110} present [52]. Both [60] and [61], look and compare the Poisson ratio of diamond, versus the fracture planes present. They both state that when the fracture planes are along {111} and {110}, that the Poisson ratio is found to be 0.0791 and 0.0730 respectively. As it will be unknown which fracture planes will be present within the spacer and due to the difference in these values being only approximately 0.006, which would result in less than a couple of degrees difference in the optimum angle of the bevels cuts, a value between these numbers of 0.075 for the Poisson ratio was selected. As when the diamond is machined and polished into the bevels cuts, it will be difficult to accurately achieve the bevel cuts to the nearest degree and they will more be cut to the nearest couple of degrees the uncertainly on diamond's Poisson ratio of 0.006 will be negligible. Once 0.075 was selected for diamonds Poisson's ratio, the final material properties could be finalised as seen in Table 11. Both the density and Young's modulus were found to have very little if not zero effect on the angle of the bevels, where the fractional length change between the mirrors was found to cross zero, for when the values were varied between different quoted values from different resources. Therefore the values which the company Diamond Materials [59] quoted were selected for the final simulations.

Table 11: Final Diamond Material Properties Selected for diamond-FS cavity.

	Diamond
Density	3515kgm^{-3}
Young's Modulus	1050GPa
Poisson's Ratio	0.075

8.1.1 Fracture planes (Cleavage) in crystals

Crystals are crystalline materials and therefore, have crystallographic structures. The location of the atoms and ions in crystals structures have a huge impact on the stiffness and even the direction in which the crystal displays the highest stiffness, as along certain planes the crystallographic structure is stronger and considerably more weak along other planes. The weaker planes are where the crystalline materials have a higher susceptibility to split, known as the crystals fracture planes or cleavage [64].

The number of crystalline planes that are present in the structure of a material will determine how many fracture planes are also present, as fracture planes are found to be parallel to the crystalline planes. Graphite has only one crystalline plane, resulting in the material having one

fracture plane, which is known has having basal cleavage. When two fracture planes are found, the material is known to have prismatic cleavage and similarly when three planes are found (which meet at 90 degrees) the material is known as cubic cleavage. Salt (halite) is well known for exhibiting perfect cubic cleavage, as when it breaks it creates cubic shaped crystals. However if three fracture planes are present that do not meet at 90 degrees then the crystal is known to have rhombohedral cleavage.
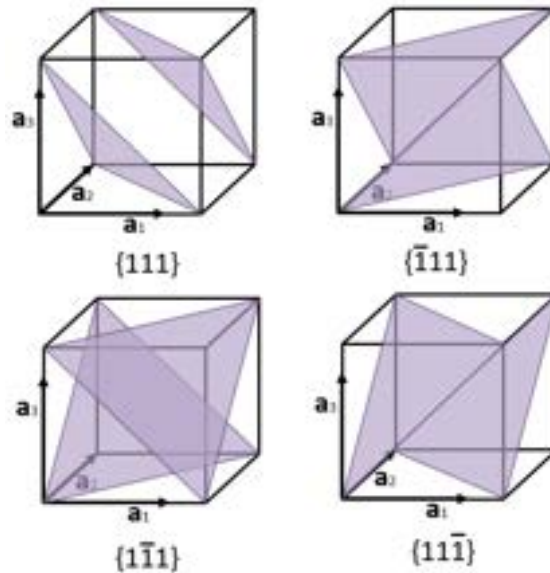
Figure 90: Miller indices along the {111} fracture planes presenting diamonds octahedral cleavage.

Due to diamond's unique structure it has octahedral cleavage, where four fracture planes are present. The cleavage occurs along the {111} planes when using Miller indices as shown in Figure 90. Along these planes diamond is prone to chipping and cutting, and more resistant in all other planes. For this reason when cleaving diamonds for jewellery a plan is normally put in place to ensure that the only cleaves made, occur along the fracture planes of the diamond. Of course more recently diamonds tend to be shaped using lasers so this is less important when cutting and sanding diamond, but if corners in the diamond are left close to a fracture plane, then this can leave the diamond very vulnerable to chipping.

As the fracture planes are formed where the carbon atoms in diamond are not as tightly packed, this will have an effect on the Poisson ratio of the crystal, and the value of the Poisson ratio will change depending on the direction in which the Poisson ratio is measured. Therefore it is important to consider the fracture planes that are present in diamond before selected an appropriate value of the Poisson ratio, especially, as the fracture planes in diamond can

occasionally occur along the {110} planes.

8.2 Minimising Small Chips between the Bevel Cuts

Due to the brittleness of diamond, having the material machined into any sharp corners, including the corner between the two bevels, could cause small fractures in the material, during the polishing process. Therefore, a thin side with thickness, κ was added to the design, as shown in Figure 91.
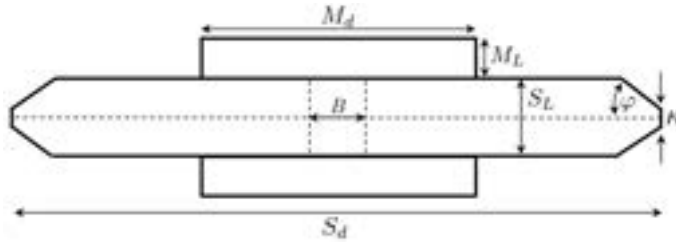
Figure 91: Diagram of the side view of circular double bevel design with added rim with thickness, κ with geometric dimensions.

This additional edge needs to be only approximately around 10 microns thick, to reasonably protect the edge spacer from fractures caused by machining the material. However, even with this added layer of protection to the design there is still a possibility of fractures occurring in the spacer, not only at the edge of the spacer but also at the corners of the bore.

With the edge, κ implemented in the diamond spacer design, it was found that this still allowed the cavity to display exceptionally low acceleration sensitivities, as displayed later in this Section. During the simulations instead of the corner between the two bevel cuts being used as the support, the entire face was used, with values of upto 30 microns explored for the length of the rim. After the initial simulations, a reasonably small value was selected for κ of twelve microns, as to ensure the bevel cut faces were as large as possible, for ease of mounting the cavity.

8.3 Size of FS-mirrors

FS mirrors most commonly can be ordered in a small range of different diameters, including half inch, one inch, two inch etc. (when working with imperial optical components). Due to the size of the diamond spacer's diameter only half and one inch mirrors would be applicable, which both normally come as quarter inch thick.

Both half and one inch FS-mirrors were simulated by changing the angle of the bevel cuts, ψ on the diamond spacer against the average fractional length change, $\Delta L/L$, by placing the cavity

134

under 1g and -1g in the x, y and z directions. The results are displayed in Figure 92. As seen both sized FS-mirrors display the same relationship and cross zero at a similar angle with similar gradients. The half inch mirror does have a slightly smaller gradient at the zero crossing but this is a minimal difference, and either sized mirror would be suitable to be used for the diamond-FS mirror. The only notable difference between the mirrors is that if the one inch mirrors are used, this may cause problems with mounting the cavity due to the mirrors having a diameter of 25.4mm which when compared to the spacer diameter of 30mm is less than 5mm difference. Therefore, the half inch mirrors would be more applicable for the diamond-FS cavity.

Figure 92: The acceleration sensitivity (fractional length change $\Delta L/L$) under 1g of vertical acceleration in each orthogonal direction averaged versus angle of bevel's, ψ for the Diamond-FS cavity for one inch and half inch FS mirrors as denoted in the top right-hand corner. The points are connected to guide the eye, with the error bars not visible on this scale. Data from simulations computed on ANSYS.

The results found when FS-mirrors are used with the diamond spacer, instead of the diamond mirrors, are distinctly similar. When comparing Figure 92 to the diamond-diamond cavity results found in Figure 82 in Chapter 7.2.2, both graphs have comparable relationships and gradients. Meaning that FS-mirrors or other mirror substrates that are cheap and more available could be incorporated with the diamond spacer design to produce a cavity with an exceptionally low acceleration sensitivity, even when mounted vertically or horizontally.

As the diamond-FS cavity has an especially short length, it will make the cavity more sensitive to Brownian motion present in the mirror coatings. Due to this, supermirrors would be an ideal option for this type of cavity as they have a lower overall Brownian motion compared to the

commonly used dielectric mirror coating (further information on mirror coatings can be found in Chapter 3.6). It is interesting to note that the coatings used in supermirrors are difficult to optically contact to diamond and are therefore not supplied for a diamond substrate but are available for FS-mirrors. As the diamond-FS cavity shows similar acceleration sensitivity values when compared to the diamond-diamond cavity results, this means that the diamond-FS cavity with these unique mirror coatings could be overall more stable than the diamond-diamond cavity.

8.4   Final Diamond Spacer Dimensions

From speaking to the company, Diamond Materials, based in Freiburg Germany (a high-purity CVD diamond discs manufacturing company), they had two options for the production of the diamond spacer. The first was that they could create the diamond crystal for the exact dimensions we had selected for simulations early on. The second was to use ready made diamond disks and have them cut and polished into the double bevel shape, with slightly different overall dimensions. As the company already had a disk with quite similar dimensions ready for the final cutting and polishing, to save time the second option was selected. Therefore, the final spacer dimensions are slightly different with the spacer length, S_L now being 1.80mm and the spacer diameter, S_d being minimally reduced to 29.00mm. With the complete dimensions with the tolerances displayed in Table 12 and with the final diamond spacer specification sheet shown in Figure 93. Both flat faces on the diamond spacer are set to have a flatness of better than $\lambda/5$, where the optical flatness is measured in fractions of $\lambda = 632.4$nm. Normally a flatness of better than $\lambda/10$ would be requested for the surface on an optical spacer but Diamond Materials could only guarantee a flatness of better than $\lambda/5$. However, at this flatness it still allows for the diamond spacer to be able to have the FS-mirrors optical contacted on to it.

Table 12: Final dimensions for diamond spacer, for diamond-FS cavity.

Parameter	Final Value	Tolerance
S_d	29.00mm	±1.00mm
S_L	1.80mm	±0.10mm
B	3.00mm	±0.20mm
κ	0.12mm	±0.05mm
ψ	36.00°	±2.00°

Tolerances were added to allow for any errors in the cutting and polishing of the diamond disk. The spacer was simulated at either end of each individual tolerance and it was found that apart

from the angle of the bevels, ψ, the small changes in the dimensions had minimal effect on the acceleration sensitivity of the cavity.
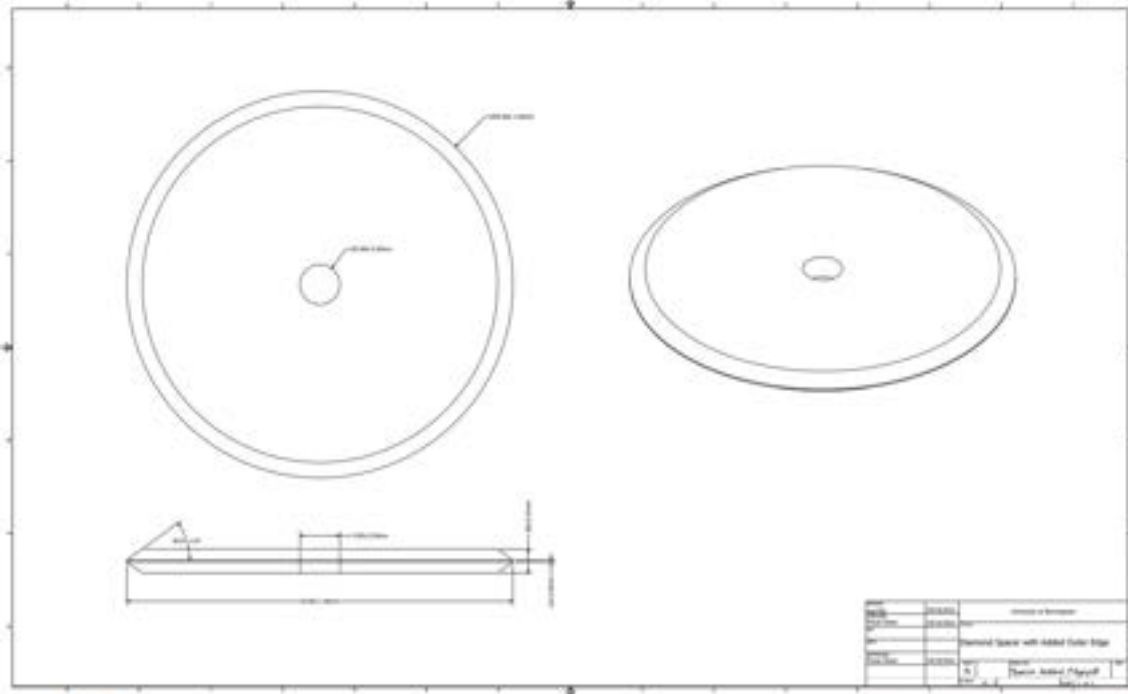
Figure 93: Final specification sheet for the diamond spacer, to be utilised within the diamond-FS cavity.

The angle of the bevels was given a reasonably large tolerance as it is quite difficult to accurately cut a diamond disk in such a way to make the bevel cuts. The acceleration sensitivity at either end of the angle tolerance was found to be $< 1.1 \times 10^{-12}$/g, if one inch mirrors are used and $< 1.5 \times 10^{-12}$/g with half inch mirrors (a full discussion on the FS-mirror sizes is found in Chapter 8.3 above).

Where the half inch FS-mirrors are used for the cavity and where it is assumed that the diamond spacer is cut to the exact final values, seen in Table 12, then the final fractional length change, $\Delta L/L$ between the two mirrors, where the cavity is placed in each orthogonal direction can be seen in Table 13. The displacement contours of when the diamond-FS cavity is vertically and horizontally mounting are shown in Figure 94.
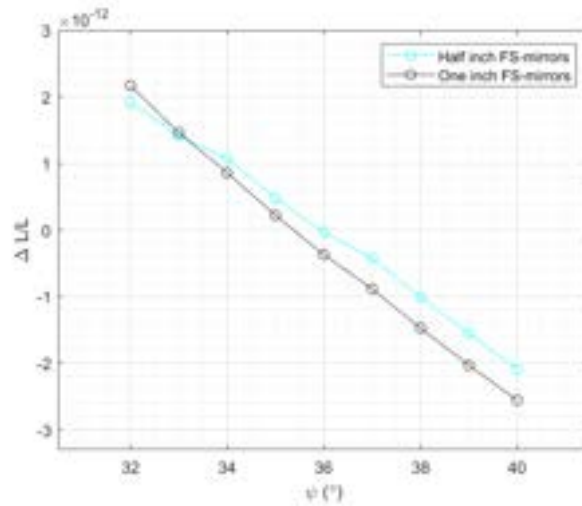
Table 13: Numerical values for the acceleration sensitivity (fractional length change $\Delta L/L$) when 1g of vertical acceleration is applied in each orthogonal axes for the diamond-FS cavity, with half inch mirrors.

X	Y	Z	$\Delta L/L$
1g	0	0	1.24×10^{-13}/g
-1g	0	0	-2.32×10^{-13}/g
0	1g	0	9.25×10^{-15}/g
0	-1g	0	9.25×10^{-15}/g
0	0	1g	-5.55×10^{-13}/g
0	0	-1g	4.53×10^{-13}/g

As seen when the cavity is mounted such that the optical axis is vertical, then the acceleration sensitivity is as low as 9.25×10^{-15}/g. As this value is nearly identical for when g is placed positive and negative in the y-direction, it suggests that the values found for $\Delta L/L$ are reasonably reliable as the cavity is completely symmetrical, so there should be no difference between the values. When the cavity is mounted horizontally, then the acceleration sensitivity is as low as 5.55×10^{-13}/g as seen in Table 13. The values for when the cavity is horizontally mounted do vary within $\approx 5 \times 10^{-13}$/g of each other which is quite large changes for values that should be identical, but as having infinite meshing cells is not possible errors will occur within the simulated data. For the simulations in this chapter ANSYS R18.2 was utilised but access was limited, so the finer meshing setting in ANSYS could not be used. A full description in the versions of ANSYS used is found in Appendix B.

<div align="center">(a)   (b)</div>
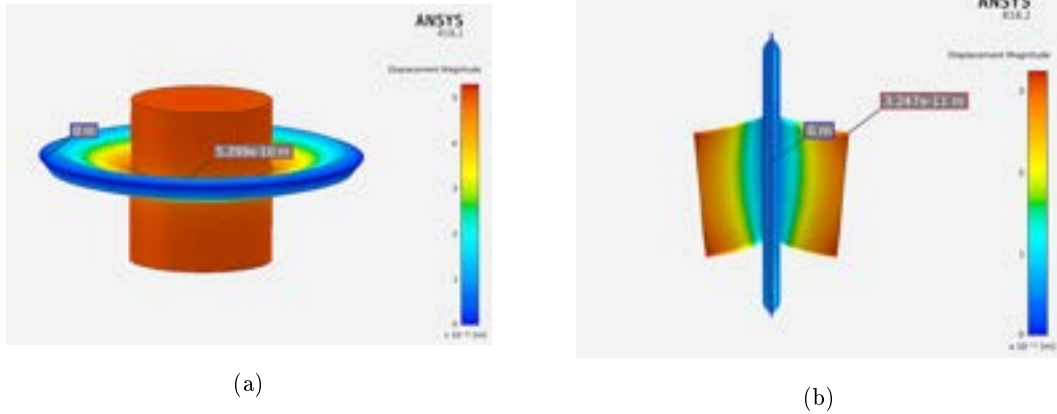
Figure 94: Displacement contour diagrams displaying the effect of vertical acceleration under 1g of acceleration on the diamond-FS cavity when (a) vertically and (b) horizontally mounted, with the scale on the right-side of each figure.

From the final dimensions of the diamond-FS cavity and with the length of cavity being approximately 1.8mm, the free spectral range is found to be expectationally large at $\approx 83.3 \times 10^9$Hz. Due to this large free spectral range and assuming the mirrors both have coatings with 99.9969% reflectance's (typical supermirrors from [49] have reflectance's of 99.9969% or higher for specific wavelengths of light) the cavity is expected to display a linewidth of $\approx 8.2 \times 10^6$Hz and finesse of 1.01×10^5. Due to these properties and in particular the large free spectral range of the diamond-FS cavity, the cavity will need to be used alongside a frequency comb, in order to be used within quantum technologies, as discussed in Section 8.5.

For the mirrors for the diamond-FS cavity, one planar and one concave mirror will be utilised to create a hemispherical shaped cavity. In order for the cavity to be within the stability condition as mentioned in Section 2.5,

$$0 \leq g_1 g_2 \leq 1. \tag{52}$$

For the planar mirror, g_1 is equal to one and where the radius of curvature of the second mirror is 100mm, $g_2 =0.98$, resulting in $g_1 g_2 = 0.98$. Therefore the cavity is within the condition but due to the short length of the cavity of 2mm it places the cavity towards the upper end of the stability condition. A hemispherical shape was selected for the cavity as by having one mirror planar it makes the cavity exceptionally robust to misalignment.

8.5 The Next Steps

Successfully in this chapter and in chapter 7 a diamond cavity with an acceleration sensitivity as low as $9.25{\times}10^{-15}$/g in one direction and $\approx 2,5{\times}10^{-13}$/g in the other two orthogonal directions, was simulated and presented. These impressively low acceleration sensitivities are lower than any other currently published optical cavity design. Therefore, to validate the diamond cavity design a prototype would need to be built and tested.

However, due to a number of delays the diamond spacer did not arrive in time for the cavity to be built or tested. If the spacer had arrived the prototype would be built by firstly optical contacting the two FS-mirrors to the diamond's surface, ensuring that each mirror is symmetrically over the bore and in the centre of each face on the diamond spacer. It is considered that the diamond cavity would benefit from being assembled under vacuum to ensure the bore of the cavity does not contain any particles that would cause more scattering in the bore of the cavity and in turn decreasing the finesse of the cavity. Although building the cavity under vacuum would make the assembling process more complex it would ensure the pressure sensitivity in the cavity is reduced as much as possible. Another benefit of building the cavity under vacuum would be that there would be more temperature control, as fewer temperature fluctuations would be present, allowing for the stability of the cavity to become more long term.

Once assembled the cavity was to be mounted horizontally using the support structure shown in Figure 95. Then by placing the structure on to the rotational table (discussed in Chapter 3.7.2), the cavity was to be locked to the laser light and the stability to be tested when the cavity was horizontally and vertically placed. The mounting structure was initially designed for the diamond-diamond cavity, which displayed an acceleration sensitivity lowest when the cavity was horizontally mounted. Therefore, once tested if the diamond-FS cavity displays a preferable acceleration sensitivity when vertically mounted then a new mounting structure would need to be designed.

Figure 95: Initial CAD design for the support structure for diamond-diamond cavity, where the cavity is dark grey, the viton o-rings are black and the aluminium support structure is light grey.

The thermal expansion of the diamond-FS cavity was explored from cryogenic temperatures all the way to well above room temperature. Coefficients of thermal expansion used for diamond and fused silica are $1.0 \times 10^{-6}/^{\circ}$C [59] and $5.5 \times 10^{-7}/^{\circ}$C [41], respectively. As shown in Figure 96 the thermal expansion has a linear relationship with a constant gradient of $1.95 \times 10^{-7}/^{\circ}$C, which is the calculated value of the coefficient of thermal expansion for the diamond-FS. While this value is reasonably low, a way to minimise it further could be to look into using Zerodur mirrors instead of fused silica, as Zerodur has a coefficient of thermal expansion of less than a fifth of fused silica [66].
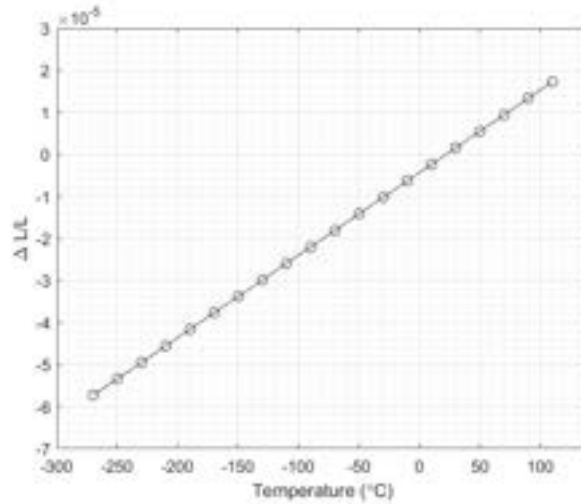
Figure 96: The thermal sensitivity (fractional length change, $\Delta L/L$ between the centre of the two diamond mirrors) for the diamond-FS cavity with respect to temperature (°C). The points are connected to guide the eye, with the error bars not visible on this scale. Data from simulations computed on ANSYS.

As the diamond cavities display acceleration sensitivities as low as $9.25{\times}10^{-15}$/g in one direction and $\approx 2, 5{\times}10^{-13}$/g in the orthogonal directions it would make the cavities suitable in applications where ultra low stability is required. For example in field deployable quantum technologies, like optical clocks and optically generated microwaves/RF, as the diamond cavities would be robust to external vibrations that are present on a moving vehicle, a ship or a plane. As the cavity has an ultra-low acceleration sensitivity it would also make the cavity robust to any vibrations that are less than $\approx 500Hz$.

There are a couple of ideas for the future work which would be interesting to research with relation to both diamond cavities. The first being to see if increasing the size of the diamond spacer would further decrease the acceleration sensitivity. However, by increasing the size of the diamond spacer this would start to increase the cost of the spacer drastically. The other idea would be to see if the acceleration sensitivity is equally as low in a diamond cavity, when Zerodur®mirrors are incorporated instead of diamond or fused silica mirrors. Zerodur is a lithium aluminium oxide glass-ceramic [65], which displays an extremely low thermal expansion which is occasionally used for the mirror material in optical cavities, where low thermal expansion is essential. Zerodur coefficient of thermal expansion is $0 \pm 0.1 \times 10^{-6}$/°C [66], which is approximately a fifth of fused silica's coefficient of thermal expansion.

9 Summary and Future Work

Throughout the work in this thesis is an in depth exploration of Fabry-Perot optical cavities and their importance to stabilising laser light for applications in quantum technologies and in particular for re-pump lasers for a magneto-optical trap, first stage cooling lasers for Sr optical clocks and for lasers that could be utilised in deployable quantum technologies, where robust ultra-stability is required.

Firstly is an introduction and detailed discussion on the theory of optical cavities and their key properties, as well as a look into the configuration of cavities and how this directly links to stability of each configuration, with a key discussion on the hemispherical configuration and how this configuration sits within the stability condition. This style of configuration is then later utilised within all cavities that are designed and built with relation to the work mentioned in this thesis. The hemispherical shape was selected as any small changes in the length of each cavity would not place the cavity out of the stable region, as well as this type of configuration having a good separation in frequency between each mode, making it an ideal cavity configuration to work with.

Building on this, is a study of how perturbations can affect the length of an optical cavity and how the length change directly links to the stability of an optical cavity. The acceleration and thermal expansion sensitivity are discussed in depth and how the magnitude of each of them can be calculated with finite element analysis in ANSYS. This method is then later used in Chapters 5, 6, 7 and 8 to ultimately reduce the acceleration sensitivity in each of the cavities and used to determine the thermal expansion in the diamond-FS cavity. Successfully using this method the acceleration sensitivity was simulated to be as low as 9.25×10^{-15}/g for the diamond-FS cavity, which if this value was reflected in experimental results would be the lowest acceleration sensitivity measured, when compared to any current published optical cavity design.

Chapter 4 describes the design and construction of a tunable 2.6μm optical cavity, which is to be implemented in [13] to stabilise a current free running re-pump laser for a magneto-optical trap. The cavity is successfully built with the use of twelve piezo-cubes, where three are wired to a vacuum wire, to allow the length of the cavity to be tunable from within the vacuum chamber. The cavity was secured within the vacuum system and the chamber was sealed using indium wire. Once the cavity was placed in the optical system it was found that the cavity was misaligned in the vacuum chamber, resulting in no light being able to pass through the system. Due to the misalignment the cavity needs to be removed from the chamber and as suggested at the end of the

143

chapter the parts of the inner vacuum chamber replaced with a new component, which allows for more access to the cavity. With this new component the cavity would be more easily and accurately aligned in the vacuum system.

In Chapter 5 is an introduction to applying additive manufacturing to create more portable and novel spacers for optical cavities, to be utilised for the first stage of cooling of Sr atoms, within portable optical clocks. With the use of invar, an iron-nickel alloy with an exceptionally low coefficient of thermal expansion at room temperature, a more portable optical cavity was designed and built. The cavity is referred to as the invar cavity and is simulated to display an acceleration sensitivity of 1.53×10^{-12}/g with a low gradient of 1.71×10^{-11}/mm at the zero crossing of the acceleration sensitivity. The cavity was assembled using a temporary adhesive and placed within a simple optical system to initially scan for the optical modes. After no build-up within the cavity was observed it was discovered that the parallelism of the cavity was 972 arcseconds (about 30 times higher than what is required), so the cavity was disassembled to allow for alterations to be made to the spacer. Once alternations are made the cavity is to be reassembled by attaching the mirrors with either a temporary or permanent solution, where the cavity is to be placed back into the optical system, where the stability is to be found and compared to the simulated results.

An idea to improve the acceleration sensitivity of the invar cavity was next implemented and explored. By incorporating an internal lattice to an invar spacer this would in turn reduce the weight of the spacer and in theory would decrease the acceleration sensitivity of the cavity. A vertical cavity design was utilised so that the support positions would not be directly under the lattice structure, so there would be no significant bending in the lattice. A vertical bicone lattice structure with a lattice thickness of 0.2mm was found that displayed a simulated acceleration sensitivity of 1.97×10^{-12}/g, which when compared to the simulated acceleration sensitivity of 3.26×10^{-12}/g for a solid vertical spacer of the same external dimensions is found to be approximately 40% lower. The lattice cavity had a 50.4% weight reduction when compared to the solid version, it is thought that the ratio of weight reduction compared to the ratio of acceleration sensitivities would, in an ideal lattice, be identical. But unfortunately as the lattice does reduce the stiffness of the cavity it would be difficult to find the ideal reduction. However, with appropriate lattice design software it is thought that a higher reduction than 40% in the acceleration sensitivity could be found.

It is interesting to find that the solid invar cavity displayed a lower acceleration sensitivity (1.53×10^{-12}/g) than the vertical lattice design (1.97×10^{-12}/g), suggesting that a horizontal

mushroom shaped spacer does ultimately have a lower acceleration sensitivity, when compared to a vertical bicone shaped shaper.

Similarly to the invar cavity, the lattice cavity was assembled using a temporary adhesive and placed into a simple optical system. There were some issues that arose while the lattice spacer was being printed and assembled, resulting in a few considerations that are mentioned in Chapter 6.6.1 to improve the design of the lattice spacer to reduce the amount of alterations that were needed to be made to the spacer after it was printed. While within the optical system, no optical modes were once again observed. It is thought that similar to the invar cavity that the parallelism of the spacer is larger than 30 arcseconds, which is stopping the light from being able to build-up within the bore. Therefore, the next steps would be to disassemble the cavity and make adjustments to the parallelism of the spacer.

Both types of invar cavities are initially designed to be utilised for the first stage of cooling of strontium (Sr) atoms, where the natural linewidth of the Sr transition is $\Gamma = 2\pi \times 32\text{MHz}$ [50] and a stability in the cavity of $\approx$100kHz is required. It is shown that due to invar's low coefficient of thermal expansion that the cavity would display a stability of 100kHz within temperature fluctuations of 144μK making the invar cavities suitable for this application. It is however, suggested that once fully built that the invar cavities would benefit from being within a temperatures controlled chamber, to protect them from temperature fluctuations that would be present in a laboratory.

The last two cavities explored in this thesis are a diamond-diamond cavity and a diamond-FS cavity. The diamond-diamond cavity is a pure diamond cavity with wide thin diamond mirrors and a thin circular double bevel shaped spacer, as discussed in Chapter 7. With the use of ANSYS the geometry of the cavity was optimised in such a way that the acceleration sensitivity was simulated to be as low as $\approx 1.5 \times 10^{-11}$/g when vertically mounted and $\approx 4 \times 10^{-14}$/g / $\approx 5.5 \times 10^{-13}$/g when horizontally mounted. During the simulation process, the Poisson ratio used was provided by the material library in ANSYS (as discussion in Appendix B) which was found to not be accurate. Therefore, researched was carried out to find a more suitable value, where 0.075 was finally selected and is the value used for all simulations on the diamond-FS cavity.

The diamond-FS cavity is the same shape diamond spacer as the diamond-diamond cavity, but with fused silica mirrors. From simulated results this cavity successfully demonstrates an acceleration sensitivity as low as 9.25×10^{-15}/g for when the cavity is vertically mounted and

$2/5{\times}10^{-13}$/g when horizontally mounted, which, if these simulated results are reflected in experimental results, would be the lowest acceleration sensitivity of any published cavity design.

To finally conclude, two new novel optical cavity designs have been presented, with the first being "invar cavities", where additive manufacturing was implemented to build two different invar cavities, which have applications in portable Sr optical clocks for the first stage cooling of Sr atoms. The second is "diamond cavities" where a thin circular double bevel diamond spacer is used alongside either diamond or fused silica mirrors. The simulated acceleration sensitivities of both diamond cavities are as low as $7/9{\times}10^{-15}$/g. These results are lower than other published optical cavity acceleration sensitivity and as the ultra-low acceleration sensitivity will also mean the cavity is robust to any vibrations that are less than $\approx 500Hz$, it gives these types of cavities the potential to be utilised in a range of applications, including to be used in field deployable quantum technologies, like optical clocks and optically generated microwaves/RF.

A CAD Components for 2.6μm Cavity

To ensure the piezo-chips are evenly attached around both the FS mirrors and ULE rings, small plastic components where designed and 3D printed. Figure 97 displays both CAD designs, with Figure 98 showing the 3D components being used on both the FS mirror and ULE ring.

<center>(a)</center>

<center>(b)</center>

Figure 97: CAD designs for 3D printed parts to align the piezo's for the 2.6μm cavity, (a) for the FS mirrors and (b) for the ULE rings.

For the wire attached piezos, a pencil was used to mark where each piezo-chip needed to be placed, using the 3D printed component

<center>(a)</center>

<center>(b)</center>
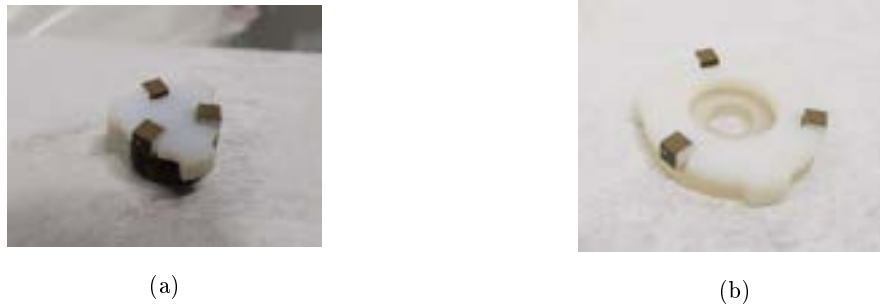
Figure 98: 3D printed parts to align the piezo's for the 2.6μm cavity, (a) for the FS mirror and (b) for the ULE ring.

For the main section in the 2.6μm cavity vacuum system there are three sections, the inner, middle and outer are all shown in Figures 99, 100 and 101 respectively. Small adjustments were later made to the inner and middle sections to make room for the wires.

Figure 99: CAD designs for vacuum system for the 2.6μm cavity (a) inner section (b) and inner section lid.

Figure 100: CAD designs for vacuum system for the 2.6μm cavity (a) middle section (b) and middle section lid.

(a)

(b)
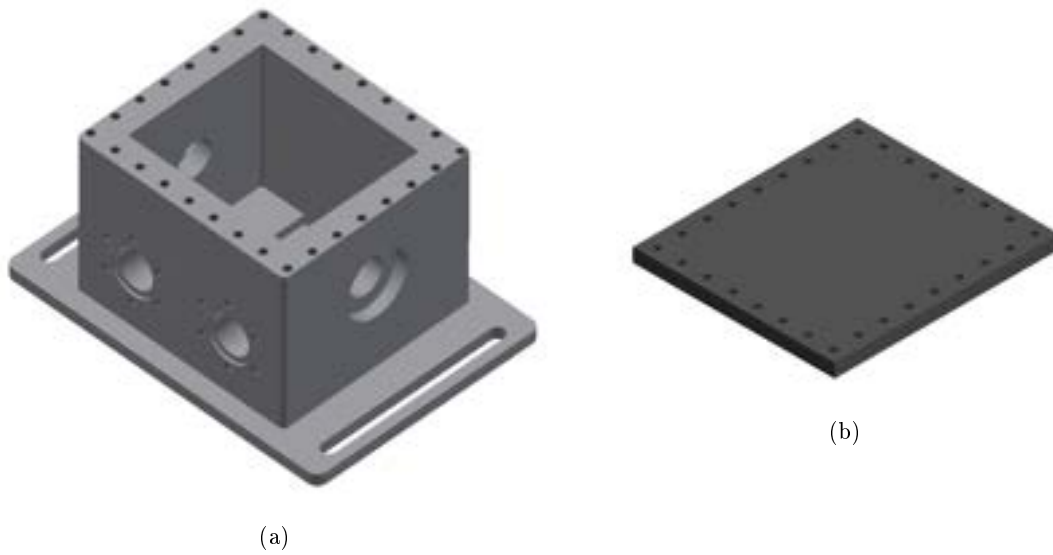
Figure 101: CAD designs for vacuum system for the 2.6μm cavity (a) outer section (b) and outer section lid.

B ANSYS Versions and Materials Library

Throughout the work mentioned in this thesis a range of ANSYS student versions were used including the student home versions ANSYS 2020 R1 and R2 academic. Both of these versions were found to have multiple meshing errors when higher meshing options were utilised, which resulted in lower meshing options being used and the results found using these versions being less reliable, as reflected in the final results found for the diamond-diamond cavities fractional length change in each orthogonal direction, as shown in Table 8. Compared to when the version which is available within the University of Birmingham R18.2 was utilised, for the finite element analysis completed in the other chapters.

Within ANSYS is a set library of materials. For the versions of ANSYS used for the work mentioned in this thesis the materials: invar, fused silica and ultra-low expansion glass (ULE) were not found in the library of materials. Therefore, these materials were manually entered in ANSYS with their properties found from a number of resources as referenced in the text.

The library did however have three types of diamond stocked, diamond, diamond PL CVD and diamond high pressure, with the values for the material properties being shown in Figures 102 and 103. For the simulations mentioned in Chapter 7 the material properties for diamond shown in Figure 102 was utilised. It is worth noting that all three diamond materials found in the ANSYS material library quote 0.2 for the Poisson ratio of diamond, which is found to not be an accurate value, as discussed in Chapter 8.1. Therefore, it is key for further simulations to manually add the material properties of diamond into ANSYS.

Figure 102: Values for the properties of diamond from the stock materials library in ANSYS.

$$(a) \qquad\qquad\qquad\qquad (b)$$

Figure 103: Values for the properties of (a) diamond PL CVD and (b) diamond high pressure from the stock materials library in ANSYS.

References

[1] J. P. Gordon, H. J. Zeiger, and C. H. Townes. (1955) 'The Maser—New Type of Microwave Amplifier, Frequency Standard, and Spectromete', *Phys. Rev.* 99, pp. 1264-1274.

[2] Jeff Hecht. (2008) *Lasers: An Entry-Level Guide*, 3rd Edition, IEEE Press: Wiley, Piscataway, New Jersey; Hoboken, New Jersey.

[3] A. E. Siegman. (1986) *Lasers*, University Science Books, Mill Valley, Calif.

[4] Chang Jian Kwong, Michael Georg Hansen, Jun Sugawara and Stephan Schiller. (2018)'Characterization of the long-term dimensional stability of a NEXCERA block using the optical resonator technique', *Measur.Sci.Tech.* 29, id. 075011.

[5] A. D. Ludlow, X. Huang, M. Notcutt, T. Zanon-Willette, S. M. Foreman, M. M. Boyd, S. Blatt, and J. Ye. (2007) 'Compact, thermal noise limited optical cavity for diode laser stabilization at 1×10^{-15}', *Opt. Lett.* 32, pp. 641-643.

[6] Lisheng Chen, John L. Hall, Jun Ye, Tao Yang, Erjun Zang, and Tianchu Li. (2006) 'Vibration-induced elastic deformation of Fabry-Perot cavities', *Phys. Rev. A* 74, id. 053801.

[7] Y. N. Zhao, J. Zhang, A. Stejskal, T. Liu, V. Elman, Z. H. Lu, and L. J. Wang. (2009) 'A vibration-insensitive optical cavity and absolute determination of its ultrahigh stability', *Opt. Express* 17, pp. 8970-8982.

[8] Won-Kyu Lee, Sang Eon Park, Chang Yong Park, Dai-Hyuk Yu, Myoung-Sun Heo, and Huidong Kim. (2019) 'Support-area Dependence of Vibration-insensitive Optical Cavities', *Curr. Opt. Photon.* 3, pp. 128-134.

[9] J. Keller, S. Ignatovich, S. A. Webster, T. E. Mehlstaubler. (2014) 'Simple vibration insensitive cavity for laser stabilization at the 10^{-16} level', *Applied Physics B*, 116, pp. 203-210.

[10] Stephen Webster and Patrick Gill. (2011)'Force-insensitive optical cavity', *Opt. Lett.* 36, pp. 3572-3574.

[11] David R. Leibrandt, Michael J. Thorpe, Mark Notcutt, Robert E. Drullinger, Till Rosenband, and James C. Bergquist. (2011) 'Spherical reference cavities for frequency stabilization of lasers in non-laboratory environments', *Opt. Express* 19, pp. 3471-3482.

[12] Eugen Wiens and Stephan Schiller. (2018) 'Simulation of force-insensitive optical cavities in cubic spacers', *Applied Physics B*, 124, pp. 1-17.

[13] Shengnan Zhang , Preetam Ramchurn, Marco Menchetti, Qasim Ubaid, Jonathan Jones, Kai Bongs et al. (2020) 'Novel repumping on $^3P_0 \rightarrow {}^3D_1$ for Sr magneto-optical trap and Lande g factor measurement of $^3D_1$ ' *J. Phys. B: At. Mol. Opt. Phys.* 53, id. 235301.

[14] M. Gellesch, J. Jones, R. Barron, A. Singh, Q. Sun, K. Bongs et al. (2020) 'Transportable optical atomic clocks for use in out-of-the-lab environments', *Advanced Optical Technologies*, 9, pp. 313-325.

[15] S. B. Koller, J. Grotti, St. Vogt, A. Al-Masoudi, S. Dörscher, S. Häfner, U. Sterr and Ch. Lisdat. (2017) 'Transportable Optical Lattice Clock with 7×10^{-17} Uncertainty', *Phys. Rev. Lett.* 118, id. 073601.

[16] S. O. Kasap. (2013) *Optoelectronics and Photonics, Principles and Practices*, Pearson Education. Chapter 1.

[17] M. Pollnau and M. Eichhorn. (2020, 'Spectral coherence, Part I: Passive-resonator linewidth, fundamental laser linewidth, and Schawlow-Townes approximation', *Progress in Quantum Electronics*, 72, 100255.

[18] L. G. Gouy. (1890) 'Sur une propriete nouvelle des ondes lumineuses', *C. R. Acad. Sci. Paris,* 110, 1251.

[19] H. Kogelnik and T. Li (1966) 'Laser Beams and Resonators', *Appl. Opt.* 1550-1567.

[20] Drever, R.W.P., Hall, J.L., Kowalski, F.V. et al. (1983) 'Laser phase and frequency stabilization using an optical resonator', *Appl. Phys. B.* 31, pp. 97-105.

[21] *Low-Voltage Piezoelectric Chips, 0.7 μm to 6.1 μm Travel* (no date). Available at: https://www.thorlabs.com/newgrouppage9.cfm?objectgroup_id=7563 (2021) (Accessed: 30 August 2021).

[22] Fireder Lindenfelser. (2011) *Laser stabilization for quantum information experiments with trapped ions*, Master Thesis, Institut for Quantum Electronics, ETH Zurich.

[23] Eric D. Black. (2001) 'An introduction to Pound–Drever–Hall laser frequency stabilization', *American Journal of Physics*, 69, 79.

[24] KATZIR S. (2006) *The Beginnings of Piezoelectricity, A Study in Mundane Physics*, Springer, Dordrecht, Chapter 1.

[25] Jacques Curie and Pierre Curie (1880) 'Développement par compression de l'électricité polaire dans les cristaux hémièdres à faces inclinées ', *Bulletin de la Société Minérologique de France*, 3(4) pp. 90-93.

[26] M. Kimura, A. Ando, Y. Sakabe. (2010) '2 - Lead zirconate titanate-based piezo-ceramics', *In Woodhead Publishing Series in Electronic and Optical Materials, Advanced Piezoelectric Materials*, pp. 89-110.

[27] Thomas Legero, Thomas Kessler, and Uwe Sterr. (2010) 'Tuning the thermal expansion properties of optical reference cavities with fused silica mirrors', *J. Opt. Soc. Am. B*, 27, pp. 914-919.

[28] Taylor, C.T. & Notcutt, M. & Wong, E.K. & Mann, A. & Blair, D.G.. (1997) 'Measurement of the thermal expansion coefficient of an all-sapphire optical cavity', *IEEE Transactions on Instrumentation and Measurement*, 46, pp. 183 - 185.

[29] M. Nagel and A. Peters. (2011) 'Towards an ultra-stable optical sapphire cavity system for testing Lorentz invariance', *arXiv: Optics*, arXiv:1112.3623v1.

[30] K. Hosaka, H. Inaba, D. Akamatsu, M. Yasuda, J. Sugawara, A. Onae, and F.-L. Hong. (2013) 'A Fabry-Perot etalon with an ultralow expansion ceramic spacer', *Japanese Journal of Applied Physics*, 52, 032402.

[31] *ULE® Corning Code 7972 Ultra Low Expansion Glass Advanced Optics and Materials - Information sheet* (2016). Available at: https://www.corning.com (Accessed: 14 May 2021).

[32] Davis, Joseph R. (2001) *Alloying: Understanding the Basics*, 1st Edition, ASM International, Materials Park. pages. 587–595.

[33] Willam D. Callister, Jr & David G. Rethwisch. (1997) *Materials Science and Engineering: An Introduction*, Fourth Edition, Wiley, New York. Chapter 19.

[34] Chunlei Qiu, Nicholas J.E. Adkins, Moataz M. Attallah. (2016) 'Selective laser melting of Invar 36: Microstructure and properties', *Acta Materialia*, 103, pp. 382-395.

[35] S. A. Webster, M. Oxborrow, and P. Gill. (2007) 'Vibration insensitive optical cavity ', *Phys. Rev. A*, 75, 011801.

[36] T. Nazarova, F. Riehle, and U. Sterr. (2006) 'Vibration-insensitive reference cavity for an ultra-narrow-linewidth laser', *Appl. Phys. B Lasers Opt.* 83,pp. 531–536.

[37] *Charles Edouard Guillaume – Facts* (no date). Available at:
https://www.nobelprize.org/prizes/physics/1920/guillaume/facts/ (Accessed: 3 Feb 2021).

[38] Mostafa Yakout, M.A. Elbestawi, Stephen C. Veldhuis. (2019) 'Density and mechanical properties in selective laser melting of Invar 36 and stainless steel 316L', *Journal of Materials Processing Technology*, 266, pp. 397-420.

[39] Grote Jark-Heinrich & Erik K. Antonsson. (2009) *Springer Handbook of Mechanical Engineering*, Springer: Berlin / Heidelberg. Chapter 8.

[40] Karunaratne, M.S.A., Kyaw, S., Jones, A. et al. (2016) 'Modelling the coefficient of thermal expansion in Ni-based superalloys and bond coatings' *J Mater Sci* 51, pp. 4213–4226.

[41] *Optical Substrates* (no date). Available at:
https://www.thorlabs.com/newgrouppage9.cfm?objectgroup_id=6973&tabname=UV%20Fused%20Silica (Accessed 5 March 2021).

[42] Gert-Jan Nijsse. (2011) *Linear motion system; a modular approach for improved straightness performance*, Doctoral Thesis, Delft University Press, Chapter 2.3.

[43] (2010) 'Maiman Builds First Working Laser. Physics History: May 16, 1960 ', *APS News*, 19(5). Available at: https://www.aps.org/publications/apsnews/201005/physicshistory.cfm (Accessed on 15 May 2021).

[44] Sruthi Viswam. (2019) *Advanced laser frequency stabilisation systems for mobile strontium optical lattice clocks*, Doctoral Thesis, The University of Birmingham.

[45] King, Steven Anthony. (2012) *Sub-Hertz Optical Frequency Metrology Using a Single Ion of 171Yb+*, Doctoral Thesis, Oxford University.

[46] S. A. Webster, M. Oxborrow, S. Pugla, J. Millo, and P. Gill. (2008) 'Thermal-noise-limited optical cavity', *Phys. Rev. A* 77, 033847.

[47] P. Koch, G. D. Cole, C. Deutsch, D. Follman, P. Heu, M. Kinley-Hanlon, R. Kirchhoff, S. Leavey, J. Lehmann, P. Oppermann, A. K. Rai, Z. Tornasi, J. Wöhler, D. S. Wu, T. Zederbauer, and H Lück. (2019) 'Thickness uniformity measurements and damage threshold tests of large-area GaAs/AlGaAs crystalline coatings for precision interferometry', *Opt. Express* 27, pp. 36731-36740.

[48] Ewen Callaway (2007) *Bad Vibrations: How to keep the effects of environmental bounce out of your data*. Available at:

https://www.minusk.com/content/in-the-news/TheSci_0907.html#indexisolator (Accessed: 2 Nov 2021).

[49] *Supermirrors* (no date). Available at: https://www.thorlabs.com/newgrouppage9.cfm?objectgroup_id=14069 (Accessed: 1 Jan 2022).

[50] Poli, N., Schioppo, M., Vogt, S. et al. (2014) 'A transportable strontium optical lattice clock', *Appl. Phys. B* 117, pp. 1107–1116.

[51] Mark Notcutt, Long-Sheng Ma, Jun Ye, and John L. Hall. (2005) 'Simple and compact 1-Hz laser system via an improved mounting configuration of a reference cavity', *Opt. Lett.* 30, pp. 1815-1817.

[52] *The Element Six CVD Diamond Handbook* (2020). Available at: https://www.e6.com/ (Accessed 16/01/2022).

[53] Alison Mainwood, Mark E Newton and Marshall Stoneham. (2009) 'Science's gem: diamond science 2009', *J. Phys.: Condens. Matter*, 21, 360301.

[54] Dodson, Joseph, Brandon, J, Dhillon, Harpreet, Friel, I, Geoghegan, S, Mollart, Timothy, Santini, P, Scarsbrook, Geoff, Twitchen, Daniel, Whitehead, A, Wilman, J, Wit, H. (2011) 'Single crystal and polycrystalline CVD diamond for demanding optical applications', *Proc. of SPIE*, 8016. 80160L-1.

[55] Alexandre Didier et al. (2016) 'Design of an ultra-compact reference ULE cavity', *J. Phys.: Conf. Ser.* 723, 012029.

[56] J. E. Field. (1979) *Diamonds: The Properties of Diamond* Academic Press, New York.

[57] Gercek, H. (2007) 'Poisson's ratio values for rocks', *International Journal of Rock Mechanics and Mining Sciences*, 44, pp. 1–13.

[58] P. H. Mott and C. M. Roland. (2009) 'Limits to Poisson's ratio in isotropic materials', *Phys. Rev. B*, 80, 132104.

[59] *Mechanical Properties of CVD Diamond* (no date). Available at: https://www.diamond-materials.com/cvd-diamant/meschanisch/ (Accessed 01 Feb 2022).

[60] J E Field. (2012) 'The mechanical and strength properties of diamond', *Rep. Prog. Phys.* 75, 126505.

[61] Claude A. Klein and Gregory F. Cardinale. (1992) 'Young's modulus and Poisson's ratio of CVD diamond', *Proceedings of the SPIE*, 1759, pp. 178-193.

[62] K. J. Dunn and F. P. Bundy. (1978) 'The stress-strain curves for cemented tungsten carbide and sintered diamond compact', *Journal of Applied Physics* 49, 5865.

[63] A. Lammer. (1988) 'Mechanical properties of polycrystalline diamonds'*Materials Science and Technology*, 4:11, pp. 949-955.

[64] Klein, Cornelis, Cornelius S. Hurlbut, and James Dwight Dana. (1999) *Manual of mineralogy: (after James D. Dana)*. New York: J. Wiley.

[65] *ZERODUR®* (no date). Available at: https://www.schott.com/en-gb/products/zerodur-p1000269 (Accessed 02 Feb 2022).

[66] *Zerodur® Broadband Dielectric Mirrors* (no date). Available at: https://www.thorlabs.com/newgrouppage9.cfm?objectgroup_id=9640 (Accessed 11 Jan 2022).